5-31-2018

Experiments and multi-field modeling of inelastic soft materials

Shuolun Wang
New Jersey Institute of Technology

ABSTRACT

EXPERIMENTS AND MULTI-FIELD MODELING OF INELASTIC SOFT MATERIALS

by
Shuolun Wang

Soft dielectrics are electrically-insulating elastomeric materials, which are capable of large deformation and electrical polarization, and are used as smart transducers for converting between mechanical and electrical energy. While much theoretical and computational modeling effort has gone into describing the ideal, time-independent behavior of these materials, viscoelasticity is a crucial component of the observed mechanical response and hence has a significant effect on electromechanical actuation. This thesis reports on a constitutive theory and numerical modeling capability for dielectric viscoelastomers, able to describe electromechanical coupling, large-deformations, large-stretch chain-locking, and a time-dependent mechanical response. This approach is calibrated to the widely-used soft dielectric VHB 4910, and the finite-element implementation of the model is used to study the role of viscoelasticity in instabilities in soft dielectrics, namely (1) the pull-in instability, (2) electrocreasing, (3) electrocavitation, and (4) wrinkling of a pretensioned three dimensional diaphragm actuator. Results show that viscoelastic effects delay the onset of instability under monotonic electrical loading and can even suppress instabilities under cyclic loading. Furthermore, quantitative agreement is obtained between experimentally measured and numerically simulated instability thresholds.

Filled rubber-like materials are important engineering materials, and they are widely used in aerospace, automotive, and other industries. However, their nonlinear, inelastic, and rate-dependent constitutive behavior is not fully understood and modeled with varying degrees of success. Much of the previous literature has focused on either capturing quasi-static stress-softening behavior or rate-dependent

viscous effects, but generally not both concurrently. This thesis develops a thermodynamically consistent constitutive model which accounts for both of those phenomena concurrently. A set of comprehensive mechanical tensile tests are conducted on the filled rubber Viton. The constitutive model is then calibrated to the experimental data, and numerically implemented into the finite element package Abaqus by writing a user material subroutine UMAT. The constitutive model is validated by comparing a numerical simulation prediction with an inhomogeneous deformation experiment. As an extension to the study of Viton, this thesis also develops a constitutive model to quantitatively capture thermal recovery of the Mullins effect. The model is then calibrated to experiments in the literature, and numerically implemented by writing a user material subroutine for the finite element program Abaqus/Standard. Lastly, simulation results suggest that the unanticipated behaviors due to recovery of Mullins effect are possible.

EXPERIMENTS AND MULTI-FIELD MODELING OF INELASTIC SOFT MATERIALS

by
Shuolun Wang

A Dissertation
Submitted to the Faculty of
New Jersey Institute of Technology
in Partial Fulfillment of the Requirements for the Degree of
Doctor of Philosophy in Mechanical Engineering

Department of Mechanical and Industrial Engineering

May 2018

APPROVAL PAGE

EXPERIMENTS AND MULTI-FIELD MODELING OF INELASTIC SOFT MATERIALS

Shuolun Wang

Shawn A. Chester, Dissertation Advisor — Date
Assistant Professor of Mechanical and Industrial Engineering, NJIT

Matthew P. Adams, Committee Member — Date
Assistant Professor of Civil and Environmental Engineering, NJIT

Siva P. V. Nadimpalli, Committee Member — Date
Assistant Professor of Mechanical and Industrial Engineering, NJIT

I. Joga Rao, Committee Member — Date
Professor and Chair of Mechanical and Industrial Engineering, NJIT

Anthony D. Rosato, Committee Member — Date
Professor of Mechanical and Industrial Engineering, NJIT

David G. Shirokoff, Committee Member — Date
Assistant Professor of Mathematical Sciences, NJIT

Pushpendra Singh, Committee Member — Date
Professor of Mechanical and Industrial Engineering, NJIT

BIOGRAPHICAL SKETCH

Author: Shuolun Wang

Degree: Doctor of Philosophy

Date: May 2018

Undergraduate and Graduate Education:

- Doctor of Philosophy in Mechanical Engineering
  New Jersey Institute of Technology, Newark, NJ, 2018
- Master of Science in Mechanical Engineering
  New Jersey Institute of Technology, Newark, NJ, 2014
- Bachelor of Science in Mechanical Engineering
  China Jiliang University, Hangzhou, Zhejiang, P.R. China, 2011

Major: Mechanical Engineering

Presentations and Publications:

S. Wang, M. Decker, D. L. Henann, and S. A. Chester. "Modeling of dielectric viscoelastomers with application to electromechanical instabilities." *Journal of Mechanics and Physics of Solids*, 95:213–229, 2016.

S. Wang and S. A. Chester. "Experimental characterization and continuum modeling of inelasticity in filled rubber-like materials." *International Journal of Solids and Structures*, 2017.

S. Wang and S. A. Chester. "Modeling thermal recovery of the Mullins effect." *Mechanics of Materials*, 2018. Submitted.

N. Bosnjak, S. Wang and S. A. Chester. "Modeling deformation-diffusion in polymeric gels." *Poromechanics VI*, 141–148, 2017.

Life is like riding a bicycle. To keep your balance you must keep moving.

Albert Einstein

ACKNOWLEDGMENT

Firstly, I would like to express my sincere gratitude to my advisor Professor Shawn Chester for his continuous support of my Ph.D. study, for his patience, motivation, and immense knowledge. His guidance helped me in all the time of research and writing of this thesis. I could not have imagined having a better advisor and mentor for my Ph.D. study.

Besides my advisor, I would like to thank the rest of my thesis committee: Professor Siva Nadimpall, Professor Pushpendra Singh, Professor I. Joga Rao, Professor Anthony Rosato, Professor Matthew Adams, and Professor David Shirokoff, for their insightful comments and encouragement, but also for the hard questions which motivated me to widen my research from various perspectives.

I thank my fellow labmate, Nikola for countless times of working together before the deadlines, and for all the fun we have had in the past handful years. I would particularly like to thank Fangda for the fruitful discussions, and his input on my research. Also, my thanks extend to the mechanics group in our department, especially Raj, Subhajit, and Akshay for being great colleagues and friends.

Last but not the least, I would like to thank my family: Lan Hu, Naining Wang, Xueyan Zhang for supporting me spiritually throughout writing this thesis and my life in general.

TABLE OF CONTENTS

TABLE OF CONTENTS
(Continued)

Chapter **Page**

TABLE OF CONTENTS
(Continued)

Chapter **Page**

LIST OF TABLES

LIST OF FIGURES

LIST OF FIGURES
(Continued)

Figure **Page**

LIST OF FIGURES
(Continued)

Figure **Page**

LIST OF FIGURES
(Continued)

Figure **Page**

LIST OF FIGURES
(Continued)

Figure **Page**

LIST OF FIGURES
(Continued)

Figure **Page**

CHAPTER 1

INTRODUCTION

1.1 Background

This thesis consists of three major parts; (i) modeling of dielectric viscoelastomers with application to electromechanical instabilities; (ii) experimental characterization and continuum modeling of inelasticity in filled-rubber like materials; and (iii) modeling thermal recovery of the Mullins effect. Each topic is discussed in more detail in the following subsections.

1.1.1 Soft Dielectrics

Soft dielectrics are compliant elastic materials, which exhibit electromechanical coupling. In particular, an unconstrained soft dielectric undergoes large mechanical deformation when subjected to an electric field [68, 100, 67], distinguishing them from stiff dielectrics, such as ceramics or glassy polymers. Soft dielectrics are capable of converting between mechanical and electrical energy, and hence, over the past two decades, significant effort has gone into using these materials as electromechanical transducers in a variety of applications [10, 64], such as artificial muscles [8], active lenses [81], loudspeakers [42], energy harvesting devices [46], and active architectural designs [16], among many others. However, the electromechanical instability, observed in soft dielectrics is a hot topic within the mechanic field, which depends on the application, could either be harmful or desirable. A better understanding of the realistic constitutive behavior of the soft dielectric as well as the proper electromechanical coupling play the crucial role in capturing the electromechanical instability. Previous works treat the soft dielectrics as "elastic" in nature and their results show varying degrees of success. The objective of this thesis is to capture the realistic mechanical behavior of the soft dielectrics *quantitatively* by using a

constitutive model that take the rate-dependent behavior as well as chain locking behavior[1] into account, and then incorporate it with the Maxwell stress. Further, the proposed model is implemented numerically by using finite element method, and based on the simulation different modes of electromechanical instabilities was investigated and compared against the experimental data.

Contribution of this thesis: We have developed a constitutive theory and numerical simulation capability for dielectric viscoelastomers. The constitutive model arises from combining our previous work on time-independent dielectric elastomers with the micromechanically motivated finite viscoelasticity model. The resulting model accounts for electromechanical coupling, large-stretch chain-locking behavior, and mechanical time-dependence. The theory has been applied to the DVE VHB 4910 – enabled by our own experimental measurements of the large-stretch equilibrium response of the material along with the data of [38] – and implemented numerically by writing customized finite elements in the commercial finite-element program [1]. The user-element subroutines as well as representative Abaqus input files are provided online as supplementary material. Using the numerical simulation capability, we have studied a number of different electromechanical instabilities: (1) the pull-in instability, (2) electrocreasing, (3) electrocavitation, and (4) wrinkling of a pre-stretched diaphragm actuator. We have shown that viscoelasticity provides stabilization that delays the onset of instability under monotonic loading and may fully suppress instabilities under sufficiently fast cyclic loading, which may be desirable for many applications. We have also demonstrated our simulation capability as a robust platform for the quantitative study of electromechanical instabilities, capable of achieving quantitative agreement with experimentally measured instability thresholds.

[1]This behavior is caused by the extensibility of the polymer chains.

1.1.2 Filled Rubber-like Materials

This thesis is also considered some rich inelastic behaviors found in filled rubber-like materials. The crosslinked polymer matrix of a rubber typically incorporates stiff filler particles of carbon black and silica in order to enhance its mechanical performance, and these materials are called filled rubber-like materials. Filled rubbers are widely used in industrial and consumer applications [14, 84, 11] ranging from tires, shock absorbers, and O-ring seals. The mechanical behavior of such materials often determines its limitations in applications. For example, the catastrophic loss of the Challenger space shuttle in 1986 was caused by the failure of an O-ring made of Viton [77], a filled rubber-like material. Accidents such as that show just how critical understanding the behavior of these materials is to larger engineering systems. The interaction between the polymer matrix and the rigid fillers gives the filled rubber-like materials very rich inelastic behavior, which includes: (i) stress softening behavior[2], (ii) rate-dependent behavior and (iii) asymmetric inelastic response[3]. Most of the literature deal with only one feature. In this thesis, a combined model is developed to account all three observed features *concurrently*. Additionally, the constitutive model is validated by comparing the numerical results with an inhomogeneous deformation experiment.

Contribution of this thesis: The combined viscoelastic and stress-softening inelastic behavior of the popular filled rubber-like material Viton was experimentally investigated, and modeled using a continuum approach. Uniaxial load/unload/reload tests, conducted at different stretch rates, as well as multi-step relaxation tests, show that Viton exhibits Mullins effect as well as rate-dependent effects. In order to separate the Mullins effect and minimize rate dependent effects, a preconditioning

[2]This is also known as the Mullins effect, in which the stress - strain curve depends on the maximum loading previously encountered.
[3]This behavior is also found in double network hydrogels, where the viscous over stress is not symmetric between loading and unloading path.

procedure was used. Further, quasi-static loading was used to eliminate rate-dependent effects from the measured response. We found that the viscous stiffness exhibited strain-stiffening behavior during loading, but that would essentially vanish during unloading.

For the constitutive model, we employ the concept of evolving hard to soft domains, and a micromechanically motivated finite viscoelasticity model. Those two are consolidated to account for the combined effects of stress-softening and viscous effects. Further, we introduced a scalar parameter in our model that controls the asymmetric inelastic behavior observed between loading and unloading, as well as the strain stiffening observed in the viscous response.

The model was calibrated to tensile tests by using a non-linear least squares method, and then implemented in the commercial finite element program [1] by writing a user-defined material subroutine (UMAT). Finally, the model was validated by comparing key features between an experiment and numerical simulation for an inhomogeneous deformation.

1.1.3 Thermal Recovery of the Mullins Effect

As an extension of the previous work of modeling inelasticity in filled rubber-like materials, this thesis also includes the study on thermal recovery of the Mullins effect. Numerous experiments show the recovery of the Mullins effect. One famous one is conducted by [33], in which eight different filled elastomers were undergone a first tensile loading, a second loading and a third loading after a stress-free annealing at a high elevated temperature. The results show different amount of recovery compared to the virgin response. The temperature dependency on both recovery rate and degree were reported in various literature [59, 76, 30, 99]. On the modeling side, most of the literature treats the Mullins effect as an irreversible process and ignore the recovery process completely. This thesis, however, a thermodynamically consistent

constitutive model is built to capture thermal recovery of Mullins effect. Using this numerical capability we show the possible failure of notched specimen during thermal recovery of the Mullins effect at different elevated temperatures.

Contribution of this thesis: We developed a thermodynamically consistent constitutive model that quantitatively captures the thermal recovery of the Mullins effect. Guided by experiments in the literature, the model follows the idea of a hard/soft phase transition to capture deformation induced stress-softening behavior while the thermal recovery is modeled through a temperature-dependent static recovery of the volume fraction of the soft domain. The model was calibrated to a suite of uniaxial experiments [33] using a non-linear least square method. Further, the performance of the model was demonstrated under uniaxial conditions. And, the practical relevance of this work was demonstrated through a three-dimensional simulation using a user-defined material subroutine (UMAT) in the commercial finite element software [1]. Lastly, in light of the progress made this work, much improvement yet remains. A suite of comprehensive experiments to measure the transient response of Mullins recovery at various elevated temperatures would greatly improve constitutive models.

1.2 Publications Related to this Thesis

The following is a list of journal publications with content related to this thesis. As matter of fact, much of the text which comprises this thesis is taken from the following publications.

1. S. Wang, M. Decker, D. L. Henann, and S. A. Chester. "Modeling of dielectric viscoelastomers with application to electromechanical instabilities." *Journal of Mechanics and Physics of Solids*, 95:213–229, 2016.

2. S. Wang and S. A. Chester. "Experimental characterization and continuum modeling of inelasticity in filled rubber-like materials." *International Journal of Solids and Structures*, 2017.

3. S. Wang and S. A. Chester. "Modeling thermal recovery of the Mullins effect." *Mechanics of Materials*, 2018. Submitted.

1.3 Structure of this Thesis

The remainder of this thesis is organized as follows. In chapter 2, thesis covers the modeling of dielectrics viscoelastomers with application to electromechanical instabilities. In chapter 3, thesis covers experimental characterization and continuum modeling of inelasticity in filled rubber-like materials. In chapter 4, thesis covers the modeling of thermal recovery of the Mullins effect. The thesis closes with conclusion and future directions in chapter 5.

CHAPTER 2

MODELING OF DIELECTRIC VISCOELASTOMERS WITH APPLICATION TO ELECTROMECHANICAL INSTABILITIES

2.1 Introduction

As soft dielectrics deform under the action of an applied electric field, it is not uncommon to encounter one of several modes of instability – a topic which has received significant attention in the recent literature [104]. Using the terminology of [104], instabilities in soft dielectrics may be categorized into three generic modes: (1) the pull-in instability [103, 70], (2) electrocreasing [94, 95, 93], and (3) electrocavitation [93], with the mode of instability dependent upon the geometric configuration and boundary conditions. Realizing that such instabilities may be harmful, methods of suppressing electromechanical instabilities and enhancing the performance of soft dielectrics have been investigated. Some of the proposed methods include applying a mechanical pre-stretch, using materials with "stiffening" properties, and constructing soft dielectric composites [104, 7]. However, instabilities are not universally harmful. Following the recent trend in mechanics of harnessing instabilities for novel functionalities [75], electromechanical instabilities in soft dielectric have been used to achieve enhanced deformations [41], as control valves in microfluidic devices [87], for tunable surfaces [93], and in anti-bio-fouling applications [82].

In order to better understand electromechanical instabilities and to harness them in design, predictive constitutive models and numerical simulation capabilities are required. The material behavior of soft dielectrics is quite rich, involving electromechanical coupling, large deformations and associated large-stretch chain locking behavior, as well as a time-dependent mechanical response. Consider, as an illustrative example, the behavior of VHB 4905/4910 – a widely studied material

in the literature [70, 86, 38, 27, 39] – which is demonstrated in Figure 2.1. First, Figure 2.1a shows the experimentally measured behavior of VHB 4910 in quasi-static, monotonic simple tension (experimental details in Section 2.3) to large stretch ($\lambda \approx 9$), presented in the form of nominal stress versus stretch. Clearly, the response of VHB is highly nonlinear and exhibits chain-locking-induced stiffening at large stretches. Second, [38] reported reversed simple tension experiments on VHB 4910 at different, constant stretch rates to different levels of maximum stretch, and their measured nominal stress versus stretch data are reproduced in Figures 2.1b-d. The data demonstrate the material time-dependence of VHB, manifested through a rate-dependent response and considerable hysteresis upon unloading. Henceforth, we will refer to soft dielectrics with mechanical time-dependence as dielectric viscoelastomers (DVEs) to distinguish them from soft dielectrics with a strictly elastic mechanical response.

The majority of the modeling work in the soft dielectric literature has focused on electromechanical coupling and non-dissipative material behavior, neglecting viscoelastic effects [20, 55, 85]. However, recent theoretical [102, 37, 78] and computational [65, 43, 9, 91, 89, 23] work has begun to address time-dependence in DVEs with the goal of describing the electromechanical response of real materials, such as VHB 4905/4910. The common approach is to utilize – within the finite viscoelasticity framework of [73] – a single non-equilibrium mechanism to account for mechanical time-dependence [37, 65, 91, 89, 23]. These studies are capable of drawing qualitative conclusions regarding the time-dependent, electromechanical response of actuators of different geometries, where the characteristic time of loading is varied compared to the material relaxation time. Other recent work [43] has begun to introduce more non-equilibrium mechanisms, so that experimental data may be quantitatively captured. Motivated by this trend of the literature, the first objective of this paper is to produce a theoretical model and finite-element-based numerical

simulation capability for DVEs that takes viscoelasticity and chain-locking into account and quantitatively apply it to VHB 4910. Our theoretical approach follows the recent modeling work of [48] on micromechanically motivated, finite-deformation viscoelasticity.

The second objective is to apply our simulation capability to the modeling of electromechanical instabilities in DVEs. A simulation capability is an essential tool in better understanding these instabilities and harnessing them in design. While the pull-in instability, which is homogeneous, may be considered analytically [103, 21], electrocreasing and electrocavitation are localized instabilities, which may not be analyzed based on linear perturbations and involve inhomogeneous deformations and electric fields. To numerically simulate these instabilities, time-dependence must be introduced, either through inertia or material time-dependence. Park and coworkers [65, 66] have used both a dynamic finite-element approach and a viscoelastic constitutive model to study electrocreasing and electrocavitation. However, obtaining quantitative agreement between experimentally measured and simulated instability thresholds has remained elusive. In this work, we study the effect of electrical loading rate on the onset and progression of electromechanical instabilities utilizing our simulation capability and use the limiting case of very slow loading rates to determine the equilibrium criteria for instabilities in different modes, showing that quantitative agreement is attained.

2.2 Continuum Framework

Kinematics: Consider a body $\mathcal{B}_{\mathrm{R}}$ identified with the region of space it occupies in a fixed reference configuration, and denote by $\mathbf{x}_{\mathrm{R}}$ an arbitrary material point of $\mathcal{B}_{\mathrm{R}}$. The referential body $\mathcal{B}_{\mathrm{R}}$ then undergoes a motion $\mathbf{x} = \boldsymbol{\chi}(\mathbf{x}_{\mathrm{R}}, t)$ to the deformed body

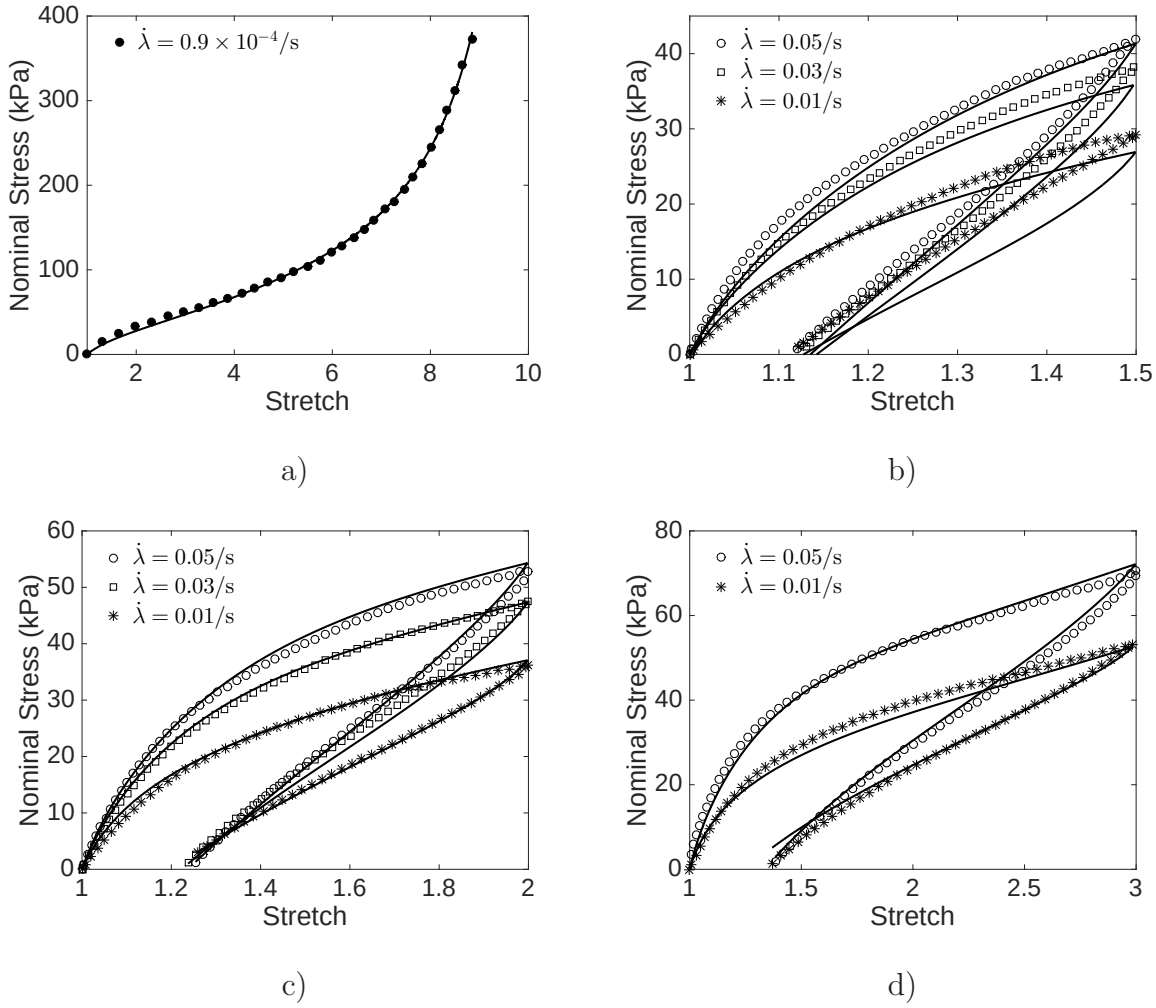

Figure 2.1 Comparison of experimental data for VHB 4910 (shown as points) to the calibrated model (shown as lines) in simple tension. a) Quasi-static monotonic tension to a maximum stretch of $\lambda \approx 9$ and the fit to the equilibrium response of (4.41). Reversed simple tension for several stretch rates to a maximum stretch of a) $\lambda = 1.5$, b) $\lambda = 2$, and c) $\lambda = 3$. The experimental data of a) is our own, while the experimental data of b), c), and d) is from [38].

$\mathcal{B}_t$ with deformation gradient given by[1] $\mathbf{F} = \nabla\boldsymbol{\chi}$, such that $J = \det \mathbf{F} > 0$. The right and left Cauchy-Green deformation tensors are given by $\mathbf{C} = \mathbf{F}^{\top}\mathbf{F}$ and $\mathbf{B} = \mathbf{F}\mathbf{F}^{\top}$, respectively.

[1]The symbols ∇, Div and Curl denote the gradient, divergence and curl with respect to the material point $\mathbf{x}_{\mathrm{R}}$ in the reference configuration; grad, div and curl denote these operators with respect to the point $\mathbf{x} = \boldsymbol{\chi}(\mathbf{x}_{\mathrm{R}}, t)$ in the deformed configuration.

Electric potential and electric field: The spatial description of the scalar electric potential is denoted by $\varphi(\mathbf{x}, t)$, and the spatial electric field is defined as

$$\mathbf{E} = -\operatorname{grad}\varphi, \tag{2.1}$$

so that the electrostatic form of Faraday's law is satisfied, i.e., $\operatorname{curl}\mathbf{E} = \mathbf{0}$. The referential electric field is related to the spatial electric field by $\mathbf{E}_{\mathrm{R}} = -\nabla\varphi = \mathbf{F}^{\top}\mathbf{E}$.

Equilibrium: Neglecting inertial effects, the balance of forces and moments in the deformed body $\mathcal{B}_t$ are expressed as

$$\operatorname{div}\mathbf{T} + \mathbf{b} = \mathbf{0} \quad \text{and} \quad \mathbf{T} = \mathbf{T}^{\top}, \tag{2.2}$$

respectively, where $\mathbf{T}$ is the Cauchy (total) stress and $\mathbf{b}$ is an external body force per unit deformed volume. We note that what we call the Cauchy stress here includes both the purely mechanical stress and the electrostatic (Maxwell) stress.

The boundary of the deformed body $\partial\mathcal{B}_t$ has outward unit normal $\mathbf{n}$. The external surface traction on an element of the deformed surface $\partial\mathcal{B}_t$ is given by

$$\mathbf{t}(\mathbf{n}) = [[\mathbf{T}]]\mathbf{n}. \tag{2.3}$$

Here $[[\cdot]]$ denotes the jump operator on the boundary $\partial\mathcal{B}_t$, defined as the difference between the the quantity inside and outside the domain – in this case $[[\mathbf{T}]] = \mathbf{T}^{\mathrm{in}} - \mathbf{T}^{\mathrm{out}}$ across $\partial\mathcal{B}_t$.

Gauss's law: We introduce the vector field $\mathbf{D}$, which denotes the electric displacement in the spatial configuration $\mathcal{B}_t$. Neglecting electrodynamic effects, Gauss's law may be expressed spatially as

$$\operatorname{div}\mathbf{D} = q, \tag{2.4}$$

where q is the free charge density per unit deformed volume. Further, the free charge density on an element of the deformed surface $\partial\mathcal{B}_t$ is given by

$$\omega(\mathbf{n}) = -[[\mathbf{D}]] \cdot \mathbf{n}, \tag{2.5}$$

where $[[\mathbf{D}]] = \mathbf{D}^{\text{in}} - \mathbf{D}^{\text{out}}$ across the boundary $\partial\mathcal{B}_t$. The referential electric displacement is related to the spatial electric displacement by $\mathbf{D}_{\text{R}} = J\mathbf{F}^{-1}\mathbf{D}$.

2.3 Constitutive Equations

Guided by the markedly time-dependent response of VHB 4910 discussed in Section 3.1 and shown in Figure 2.1, we assume that mechanical deformation is accommodated by a combination of one equilibrium mechanism and N non-equilibrium mechanisms denoted by $\alpha = 1, 2, \ldots, N$. The equilibrium mechanism describes the "long-time," hyperelastic response of the material, mathematically utilizing the total deformation gradient $\mathbf{F}$, whereas the N non-equilibrium mechanisms capture the dissipative, time-dependent response of the material using a set of N internal variables. Based on the work of [48], which was later successfully applied to VHB 4910 [38], we introduce a set of symmetric, stretch-like tensorial internal variables $\mathbf{A}^{(\alpha)}$ for the N non-equilibrium mechanisms. The thermodynamics of electromechanical coupling and the non-equilibrium mechanisms along with the attendant restrictions required to satisfy the second law are discussed in [35] and [48], respectively, and for brevity are not repeated here. Instead, we discuss a set of specialized constitutive equations for *isotropic* and *nearly-incompressible* materials. The major ingredients of the constitutive model are the free energy per unit reference volume $\psi_{\text{R}} = \hat{\psi}_{\text{R}}(\mathbf{C}, \mathbf{A}^{(\alpha)}, \mathbf{D}_{\text{R}})$ and a set of evolution equations for the internal variables $\mathbf{A}^{(\alpha)}$, each of which are discussed in detail below.

Free energy: We assume that the free energy is additively decomposed into (1) a contribution from the equilibrium mechanism $\hat{\psi}_{\text{R}}^{\text{eq}}$, which is only a function of $\mathbf{C}$, (2)

contributions from each of the non-equilibrium mechanisms $\hat{\psi}_{\mathrm{R}}^{\mathrm{neq}(\alpha)}$, each of which is a function of both $\mathbf{C}$ and the respective $\mathbf{A}^{(\alpha)}$, and (3) a contribution from electrical polarization $\hat{\psi}_{\mathrm{R}}^{\mathrm{elec}}$, which is a function of both $\mathbf{C}$ and $\mathbf{D}_{\mathrm{R}}$, i.e.,

$$\hat{\psi}_{\mathrm{R}}(\mathbf{C}, \mathbf{A}^{(\alpha)}, \mathbf{D}_{\mathrm{R}}) = \hat{\psi}_{\mathrm{R}}^{\mathrm{eq}}(\mathbf{C}) + \sum_{\alpha=1}^{N} \hat{\psi}_{\mathrm{R}}^{\mathrm{neq}(\alpha)}(\mathbf{C}, \mathbf{A}^{(\alpha)}) + \hat{\psi}_{\mathrm{R}}^{\mathrm{elec}}(\mathbf{C}, \mathbf{D}_{\mathrm{R}}). \tag{2.6}$$

We note that the additive decomposition of the mechanical free energy into equilibrium and non-equilibrium parts is a common approach in the literature [4, 74]. The Cauchy stress is then given through

$$\mathbf{T} = J^{-1} \frac{\partial \hat{\psi}_{\mathrm{R}}}{\partial \mathbf{F}} \mathbf{F}^{\top} = \mathbf{T}^{\mathrm{eq}} + \sum_{\alpha} \mathbf{T}^{\mathrm{neq}(\alpha)} + \mathbf{T}^{\mathrm{elec}}, \tag{2.7}$$

where

$$\mathbf{T}^{\mathrm{eq}} = J^{-1} \frac{\partial \hat{\psi}_{\mathrm{R}}^{\mathrm{eq}}}{\partial \mathbf{F}} \mathbf{F}^{\top}, \quad \mathbf{T}^{\mathrm{neq}(\alpha)} = J^{-1} \frac{\partial \hat{\psi}_{\mathrm{R}}^{\mathrm{neq}(\alpha)}}{\partial \mathbf{F}} \mathbf{F}^{\top}, \quad \text{and} \quad \mathbf{T}^{\mathrm{elec}} = J^{-1} \frac{\partial \hat{\psi}_{\mathrm{R}}^{\mathrm{elec}}}{\partial \mathbf{F}} \mathbf{F}^{\top} \tag{2.8}$$

are the equilibrium, non-equilibrium, and electrostatic contributions to the Cauchy stress, respectively. Each contribution is considered below.

1. *Equilibrium mechanical free energy*: First, since we are considering *nearly*-incompressible materials, we introduce the distortional part of the deformation gradient, defined as $\mathbf{F}_{\mathrm{dis}} = J^{-1/3}\mathbf{F}$ so that $\det \mathbf{F}_{\mathrm{dis}} = 1$. The distortional right and left Cauchy-Green deformation tensors are then $\mathbf{C}_{\mathrm{dis}} = \mathbf{F}_{\mathrm{dis}}^{\top}\mathbf{F}_{\mathrm{dis}} = J^{-2/3}\mathbf{C}$ and $\mathbf{B}_{\mathrm{dis}} = \mathbf{F}_{\mathrm{dis}}\mathbf{F}_{\mathrm{dis}}^{\top} = J^{-2/3}\mathbf{B}$. Next, motivated by the experiment shown in Figure 2.1a, which displays significant large-stretch stiffening, we adopt an inverse-Langevin-type material model [3, 2] for the equilibrium mechanical free energy to account for the effect of chain locking. With $\bar{\lambda} = \sqrt{\mathrm{tr}\,\mathbf{C}_{\mathrm{dis}}/3}$, we assume the form

$$\hat{\psi}_{\mathrm{R}}^{\mathrm{eq}} = G_{\mathrm{eq}}\lambda_{\mathrm{L}}^2 \left[\left(\frac{\bar{\lambda}}{\lambda_{\mathrm{L}}} \right) \beta + \ln \left(\frac{\beta}{\sinh \beta} \right) - \left(\frac{1}{\lambda_{\mathrm{L}}} \right) \beta_0 + \ln \left(\frac{\beta_0}{\sinh \beta_0} \right) \right] + \frac{1}{2} K (J-1)^2, \tag{2.9}$$

where G_{eq} and K are the equilibrium, ground-state shear and bulk moduli, respectively, and λ_{L} represents the locking stretch associated with limited chain extensibility of the long chain polymer molecules. Also, in (2.9) the functions β and β_0 are given by

$$\beta = \mathcal{L}^{-1}\left(\frac{\bar{\lambda}}{\lambda_{\text{L}}}\right) \quad \text{and} \quad \beta_0 = \mathcal{L}^{-1}\left(\frac{1}{\lambda_{\text{L}}}\right), \tag{2.10}$$

where $\mathcal{L}^{-1}$ is the inverse of the Langevin function, $\mathcal{L}(\bullet) = \coth(\bullet) - 1/(\bullet)$. The equilibrium contribution to the free energy is then

$$\mathbf{T}^{\text{eq}} = J^{-1}\frac{\partial \hat{\psi}_{\text{R}}^{\text{eq}}}{\partial \mathbf{F}}\mathbf{F}^{\top} = J^{-1}G_{\text{eq}}\left(\frac{\lambda_{\text{L}}}{\bar{\lambda}}\right)\mathcal{L}^{-1}\left(\frac{\bar{\lambda}}{\lambda_{\text{L}}}\right)(\mathbf{B}_{\text{dis}})_0 + K(J-1)\mathbf{1}. \tag{2.11}$$

2. *Non-equilibrium mechanical free energy*: To model the non-equilibrium viscoelastic contributions, following [48], we adopt the thermodynamically consistent and micromechanically motivated non-equilibrium free energy function

$$\hat{\psi}_{\text{R}}^{\text{neq}(\alpha)} = \frac{1}{2}G_{\text{neq}}^{(\alpha)}\left[\left(\mathbf{A}^{(\alpha)} : \mathbf{C}_{\text{dis}} - 3\right) - \ln\left(\det \mathbf{A}^{(\alpha)}\right)\right], \tag{2.12}$$

where $G_{\text{neq}}^{(\alpha)}$ are the non-equilibrium shear moduli. Straightforward calculations give the non-equilibrium contribution to the Cauchy stress for mechanism α as

$$\mathbf{T}^{\text{neq}(\alpha)} = J^{-1}\frac{\partial \hat{\psi}_{\text{R}}^{\text{neq}(\alpha)}}{\partial \mathbf{F}}\mathbf{F}^{\top} = J^{-1}G_{\text{neq}}^{(\alpha)}\left[\mathbf{F}_{\text{dis}}\mathbf{A}^{(\alpha)}\mathbf{F}_{\text{dis}}^{\top} - \frac{1}{3}(\mathbf{A}^{(\alpha)} : \mathbf{C}_{\text{dis}})\mathbf{1}\right]. \tag{2.13}$$

It bears noting that the stresses $\mathbf{T}^{\text{neq}(\alpha)}$ are deviatoric, and hence, the volumetric response is strictly elastic and given through the second term of (4.41).

3. *Electrical free energy*: Finally, for the electrical free energy, we adopt the form associated with the "ideal dielectric elastomer" [101]

$$\hat{\psi}_{\text{R}}^{\text{elec}} = \frac{1}{2\epsilon}J^{-1}\mathbf{D}_{\text{R}} \cdot \mathbf{C}\mathbf{D}_{\text{R}}, \tag{2.14}$$

where ϵ is the *constant* dielectric permittivity. While it is known that the permittivity is a function of the deformation [45, 98, 86], [90] showed the effect on electrostriction is negligible, and therefore we do not include this effect here. The electrostatic Cauchy stress and spatial electric field are then

$$\begin{cases} \mathbf{T}^{\text{elec}} = J^{-1}\dfrac{\partial \hat{\psi}_{\text{R}}^{\text{elec}}}{\partial \mathbf{F}}\mathbf{F}^{\top} = \dfrac{1}{\epsilon}\left[\mathbf{D}\otimes\mathbf{D} - \dfrac{1}{2}(\mathbf{D}\cdot\mathbf{D})\mathbf{1}\right], \\ \mathbf{E} = \mathbf{F}^{-\top}\dfrac{\partial \hat{\psi}_{\text{R}}^{\text{elec}}}{\partial \mathbf{D}_{\text{R}}} = \dfrac{1}{\epsilon}\mathbf{D}. \end{cases} \tag{2.15}$$

Inverting (2.15) so as to express the electrostatic Cauchy stress and spatial electric displacement in terms of the spatial electric field – a form more amenable to our finite-element implementation – we have

$$\begin{cases} \mathbf{T}^{\text{elec}} = \epsilon\left[\mathbf{E}\otimes\mathbf{E} - \dfrac{1}{2}(\mathbf{E}\cdot\mathbf{E})\mathbf{1}\right], \\ \mathbf{D} = \epsilon\mathbf{E}. \end{cases} \tag{2.16}$$

Combining (4.41), (3.19), and $(2.16)_1$, the Cauchy stress is

$$\begin{aligned} \mathbf{T} = {} & J^{-1}G_{\text{eq}}\left(\frac{\lambda_{\text{L}}}{\bar{\lambda}}\right)\mathcal{L}^{-1}\left(\frac{\bar{\lambda}}{\lambda_L}\right)(\mathbf{B}_{\text{dis}})_0 + K(J-1)\mathbf{1} \\ & + \sum_{\alpha} J^{-1}G_{\text{neq}}^{(\alpha)}\left[\mathbf{F}_{\text{dis}}\mathbf{A}^{(\alpha)}\mathbf{F}_{\text{dis}}^{\top} - \frac{1}{3}(\mathbf{A}^{(\alpha)}:\mathbf{C}_{\text{dis}})\mathbf{1}\right] + \epsilon\left[\mathbf{E}\otimes\mathbf{E} - \frac{1}{2}(\mathbf{E}\cdot\mathbf{E})\mathbf{1}\right]. \end{aligned} \tag{2.17}$$

Evolution equations for the internal variables: Finally, following [48], an evolution equation is provided for the internal variables in the form

$$\dot{\mathbf{A}}^{(\alpha)} = \frac{1}{\tau^{(\alpha)}}\left(\mathbf{C}_{\text{dis}}^{-1} - \mathbf{A}^{(\alpha)}\right), \quad \mathbf{A}(\mathbf{x}_{\text{R}}, t=0) = \mathbf{1}, \tag{2.18}$$

with $\tau^{(\alpha)}$ the relaxation time for each mechanism α.

Material parameters for VHB 4910: The calibration of material parameters is straightforward process, organized into three steps. First, the equilibrium

parameters G_{eq} and λ_{L} are determined from quasi-static experiments. Second, the non-equilibrium parameters $G_{\text{neq}}^{(\alpha)}$ and $\tau^{(\alpha)}$ are obtained by fitting to reversed experiments performed at different strain rates. Finally, we estimate the dielectric permittivity ϵ based on values appearing in the literature.

In order to determine the equilibrium parameters, we perform quasi-static, monotonic tension tests, using specimens cut from VHB 4910 tape into ASTM-D638-V dog bones with a gauge length of 0.9525 cm and a gauge width of 0.3185 cm, using a specimen cutting die. A permanent marker is used to draw black dots in the gauge section of each specimen for the purpose of Digital Image Correlation (DIC) strain measurement. Since our intent is to determine the equilibrium behavior, a constant stretch rate of $\dot{\lambda} = 0.9 \times 10^{-4}/\text{s}$ is prescribed. The experimental data presented in Figure 2.1a is the average of three tests that are nearly identical. Our new quasi-static tension test reaches a maximum uniaxial stretch of almost 9 – much greater than the maximum uniaxial stretch of 3 considered in [38] – and clearly shows locking behavior so that all material parameters in the equilibrium response may be obtained. We perform a nonlinear least squares fit of the equilibrium nominal stress, $J\mathbf{T}^{\text{eq}}\mathbf{F}^{-\top}$ with $\mathbf{T}^{\text{eq}}$ given through (4.41), specialized to simple tension, to the data of Figure 2.1a to obtain the equilibrium model parameters G_{eq} and λ_{L}, with the corresponding model fit shown in Figure 2.1a. To approximate nearly-incompressible conditions, we take the bulk modulus K to be three orders of magnitude greater than the ground state shear modulus G_{eq}.

Next, turning attention the the non-equilibrium response, we aim to calibrate the parameters $G_{\text{neq}}^{(\alpha)}$ and $\tau^{(\alpha)}$ appearing in (3.19) and (3.22) against the load/unload experiments of [38]. We perform a nonlinear least squares fit for all the remaining experimental data shown in Figure 2.1. Using the L^2 norm of the residual as our measure of quality, we have found that $\alpha = 3$ leads to well converged results as well as physically realistic parameter values for $G_{\text{neq}}^{(\alpha)}$ and $\tau^{(\alpha)}$. The fit of the purely

Table 2.1 Material Properties for the Mechanical Response of VHB 4910

Parameter	Value	Parameter	Value	Parameter	Value
G_{eq}	15.36 kPa	$G_{\text{neq}}^{(1)}$	26.06 kPa	$\tau^{(1)}$	0.6074 s
$K\,(=10^3 G_{\text{eq}})$	15.36 MPa	$G_{\text{neq}}^{(2)}$	26.53 kPa	$\tau^{(2)}$	6.56 s
λ_{L}	5.99	$G_{\text{neq}}^{(3)}$	10.83 kPa	$\tau^{(3)}$	61.25 s

mechanical model to the reversed tension experimental data of [38] is shown in Figures 2.1b-d, and the numerical values of the material parameters are summarized in Table 3.1.

Finally, considering the electrical response, we have only the dielectric permittivity ϵ appearing in (2.16). Typical values of ϵ for acrylic elastomers such as VHB are on the order of $\sim 10^{-12}\,\text{F/m}$. Instead of specifying the quantitative value, in our numerical simulations, we normalize the electrical problem so that ϵ is unity. This approach is appropriate when "ideal" dielectric behavior (2.14) is assumed.

2.4 Boundary-value Problem and Finite-element Implementation

Strong form of the boundary-value problem: In the absence of body forces and volumetric free charge density, the governing partial differential equations, expressed in the deformed body $\mathcal{B}_t$, consist of the balance of momentum,

$$\operatorname{div}\mathbf{T} = \mathbf{0} \quad \text{in} \quad \mathcal{B}_t, \tag{2.19}$$

with $\mathbf{T}$ given by (2.17), and Gauss's law,

$$\operatorname{div}\mathbf{D} = 0 \quad \text{in} \quad \mathcal{B}_t, \tag{2.20}$$

with $\mathbf{D}$ given by $(2.16)_2$. With the spatial description of displacement given through $\mathbf{u}(\mathbf{x},t)=\mathbf{x}-\boldsymbol{\chi}^{-1}(\mathbf{x},t)$, the mechanical boundary conditions on $\partial\mathcal{B}_t$ are given by

$$\mathbf{u}=\breve{\mathbf{u}} \quad \text{on} \quad \mathcal{S}_{\mathbf{u}}, \quad \text{and} \quad \mathbf{T}\mathbf{n}=\breve{\mathbf{t}} \quad \text{on} \quad \mathcal{S}_{\mathbf{t}}, \tag{2.21}$$

where $\breve{\mathbf{u}}$ and $\breve{\mathbf{t}}$ are the prescribed displacements and spatial surface tractions, respectively, and $\mathcal{S}_{\mathbf{u}}$ and $\mathcal{S}_{\mathbf{t}}$ are complementary subsurfaces of $\partial\mathcal{B}_t$. The electrical boundary conditions on $\partial\mathcal{B}_t$ are given by

$$\varphi=\breve{\varphi} \quad \text{on} \quad \mathcal{S}_{\varphi}, \quad \text{and} \quad -\mathbf{D}\cdot\mathbf{n}=\breve{\omega} \quad \text{on} \quad \mathcal{S}_{\omega}, \tag{2.22}$$

where $\breve{\varphi}$ and $\breve{\omega}$ are the prescribed electric potentials and spatial surface charge density, respectively, and $\mathcal{S}_{\varphi}$ and $\mathcal{S}_{\omega}$ are another set of complementary subsurfaces of $\partial\mathcal{B}_t$. The coupled set of equations (2.19) and (2.20), along with the boundary conditions (2.21) and (2.22), represent the strong form of the spatial boundary-value problem for the displacement field and the electric potential field.

Comment on the electrical boundary conditions: We note that in writing the boundary conditions $(2.21)_2$ and $(2.22)_2$, we have neglected the contribution of the surroundings, i.e., the jump conditions appearing in (2.3) and (2.5) are not considered in $(2.21)_2$ and $(2.22)_2$. This is not a simplification that may be made under all circumstances. In a general setting, the space surrounding the soft dielectric will have nonzero Cauchy stress and electric displacement. For the case of a vacuum, they are given by $\mathbf{T}=\epsilon_0\left[\mathbf{E}\otimes\mathbf{E}-\frac{1}{2}(\mathbf{E}\cdot\mathbf{E})\mathbf{1}\right]$ and $\mathbf{D}=\epsilon_0\mathbf{E}$, with ϵ_0 the permittivity of free space. The effect of nonzero stress and electric displacement in the surroundings may be important in some situations, but in others, they may be negligible. For example, in Appendix A of [35], we discussed the effect of the surroundings on thin DE layers – a common configuration – and showed that neglecting the surroundings and utilizing the simplified boundary conditions $(2.21)_2$ and $(2.22)_2$ was well justified.

We will revisit this point where appropriate when simulating different configurations in Section 3.6.

Weak form of the boundary-value problem: With $\mathbf{w}_1$ and w_2 denoting two weighting fields, the weak form of the boundary-value problem (2.19) through (2.22) is

$$\begin{aligned} \int_{\mathcal{B}_t} \left(\mathbf{T} : \frac{\partial \mathbf{w}_1}{\partial \mathbf{x}} \right) dv &= \int_{\mathcal{S}_{\mathbf{t}}} \left(\mathbf{w}_1 \cdot \breve{\mathbf{t}} \right) da, \\ \int_{\mathcal{B}_t} \left(\mathbf{D} \cdot \frac{\partial w_2}{\partial \mathbf{x}} \right) dv + \int_{\mathcal{S}_\omega} \left(w_2 \breve{\omega} \right) da &= 0. \end{aligned} \tag{2.23}$$

Finite-element implementation: The weak form of the governing equations (2.23) is a suitable basis for a finite-element formulation. Following our previous work [35], the deformed body is approximated using finite elements, $\mathcal{B}_t = \cup \mathcal{B}_t^{\mathrm{e}}$, and the nodal solution variables are taken to be the displacement and the electric potential, which are interpolated inside each element by

$$\mathbf{u} = \sum \mathbf{u}^A N^A \quad \text{and} \quad \varphi = \sum \varphi^A N^A, \tag{2.24}$$

with the index $A = 1, 2, \ldots$ denoting the nodes of the element, $\mathbf{u}^A$ and φ^A the nodal displacements and electric potentials, and N^A the shape functions. Employing a standard Galerkin approach, in which the weighting fields $\mathbf{w}_1$ and w_2 are interpolated by the same shape functions, leads to the following element-level residuals:

$$\begin{aligned} (\mathbf{R}_{\mathbf{u}})^A &= -\int_{\mathcal{B}_t^e} \left(\mathbf{T} \frac{\partial N^A}{\partial \mathbf{x}} \right) dv + \int_{\mathcal{S}_{\mathbf{t}}^e} \left(N^A \breve{\mathbf{t}} \right) da, \\ (R_\varphi)^A &= \int_{\mathcal{B}_t^e} \left(\mathbf{D} \cdot \frac{\partial N^A}{\partial \mathbf{x}} \right) dv + \int_{\mathcal{S}_\omega^e} \left(N^A \breve{\omega} \right) da. \end{aligned} \tag{2.25}$$

These element-level residuals are assembled into a set of global residuals, which when set equal to zero, represent a non-linear system of equations for the nodal degrees of freedom, which – when accompanied by appropriate tangents – may be solved iteratively using a Newton-Raphson procedure. Our finite-element procedures have

been implemented in [1], following our own recent work [12, 35, 13], using a user-element subroutine (UEL). We have developed four-noded isoparametric quadrilateral plane-strain and axisymmetric user-elements, as well as an eight-noded continuum brick user-element. These elements have been verified for electromechanical loading without time-dependence in our previous work [35]. In order to avoid issues related to volumetric-locking, we utilize the F-bar method of [15] for fully-integrated elements. For complete details regarding the implementation of Abaqus user-element subroutines for multi-physics problems, readers are referred to [13]. All Abaqus user-element subroutines used in the subsequent section have been made available online as supplementary material.

2.5 Numerical Simulations

In this section, we apply our numerical simulation capability calibrated for VHB 4910 in several configurations in which electromechanical instabilities are known to arise. Our intent is twofold: (1) to understand the effect of material time dependence on electromechanical instabilities and (2) to demonstrate a robust route for simulating electromechanical instabilities so that they may be harnessed in design. We consider the following settings: (1) the pull-in instability, (2) electrocreasing, (3) electrocavitation, and (4) wrinkling of a pretensioned three dimensional diaphragm actuator.

2.5.1 Pull-in Instability

We begin by considering the most basic electromechanical instability – the pull-in instability – in which deformation remains homogeneous. In this configuration, a thin soft dielectric layer is sandwiched between two compliant electrodes.[2] When an electric potential difference is applied across the layer, its thickness reduces, while the

[2]The electrodes are compliant in the sense that they do not contribute to the structural stiffness of the soft dielectric layer.

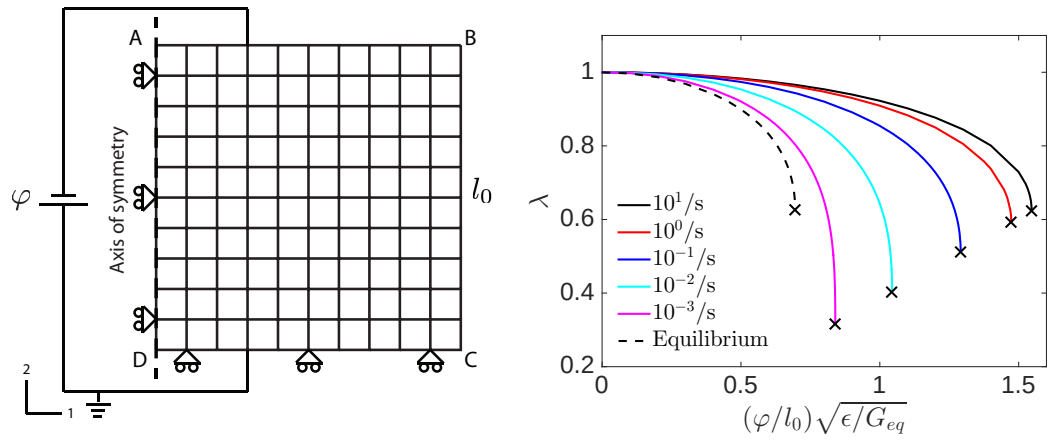

a) b)

Figure 2.2 a) Finite-element mesh and electromechanical boundary conditions used in the axisymmetric pull-in instability simulations. b) Simulated stretch in the 2-direction, λ, as a function of the normalized electric potential, $(\varphi/l_0)\sqrt{\epsilon/G_{\text{eq}}}$, for electric potential ramp rates of $(\dot{\varphi}/l_0)\sqrt{\epsilon/G_{\text{eq}}} = 10^{-3}, 10^{-2}, 10^{-1}, 10^{0}$, and 10^{1}/s (solid lines) along with the equilibrium response (dashed line). The onset of the pull-in instability is indicated by a $\times$ symbol and is delayed with increasing loading rate.

area of the film increases due to incompressibility. Due to thickness reduction, the spatial electric field grows faster than its referential counterpart, and the electrostatic Cauchy stress consequently grows quite rapidly. If this positive feedback outpaces the material's ability to mechanically resist deformation, unimpeded thinning commences, and the pull-in instability occurs.

In our simulations, we consider an axisymmetric geometry, consisting of a box with initial side lengths l_0, as shown in Figure 2.2a, and meshed with 100 axisymmetric user elements. We are interested in the homogeneous response of an isolated DVE, and hence, ignoring jump boundary conditions is appropriate. For the mechanical boundary conditions, faces AD and CD are assigned appropriate symmetry conditions while faces AB and and BC are traction-free. For the electrical boundary conditions, face CD is set to ground, $\breve{\varphi} = 0$, while face AB is assigned an electric potential history, $\breve{\varphi}(t)$. We consider monotonic ramp rates of $(\dot{\varphi}/l_0)\sqrt{\epsilon/G_{\text{eq}}} = 10^{-3}, 10^{-2}, 10^{-1}, 10^{0}$, and 10^{1}/s. Figure 2.2b shows the simulated stretch in the 2-direction, λ, as a function of

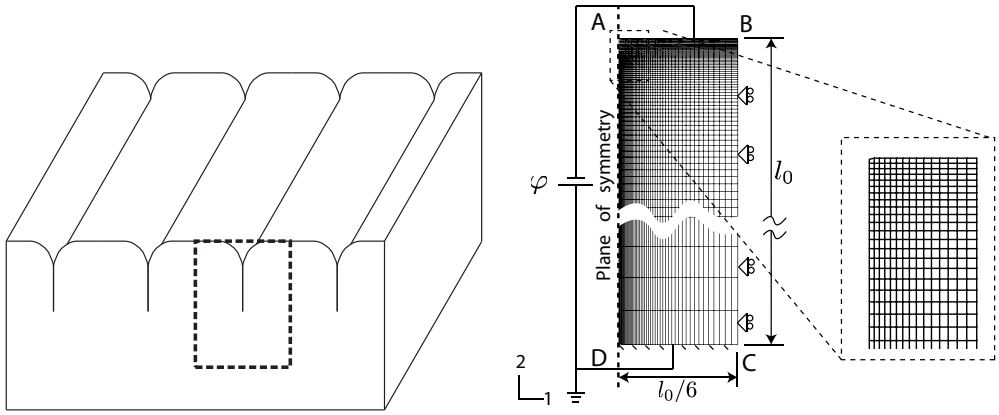

a) b)

Figure 2.3 a) Schematic of a soft dielectric layer with aligned creases. In our simulations we model a single plane-strain half cell as indicated by the dashed box. b) Finite-element mesh and electromechanical boundary conditions used in the two-dimensional, plane-strain electrocreasing simulations. The dashed line along the symmetry plane represents a fixed, frictionless, rigid surface that serves to model self-contact once the crease is formed.

the normalized electric potential, $(\varphi/l_0)\sqrt{\epsilon/G_{\text{eq}}}$, for each of these ramp rates as well as the equilibrium response.[3] From Figure 2.2b, it is clear that material time-dependence acts to delay the onset of the instability with increased loading rate. As the ramp rate is decreased, the electric field at the onset of instability approaches the equilibrium value of $(\varphi/l_0)_{\text{cr}}\sqrt{\epsilon/G_{\text{eq}}} = 0.69$, which is consistent with the theoretically determined value for a Neo-Hookean material [104].

2.5.2 Electrocreasing

Next, we consider the more complex electromechanical instability of electrocreasing, which involves highly inhomogeneous deformations and electric fields. When a soft dielectric layer is sandwiched between a rigid electrode on one side and a compliant electrode on the opposite side, lateral expansion – and hence thinning – is prevented by the rigid electrode, and the pull-in instability is suppressed. In this case, instability occurs through the formation of creases on the unconstrained side of the soft dielectric

[3]The equilibrium response was simulated by setting $G_{\text{neq}}^{(\alpha)} = 0$ for all α.

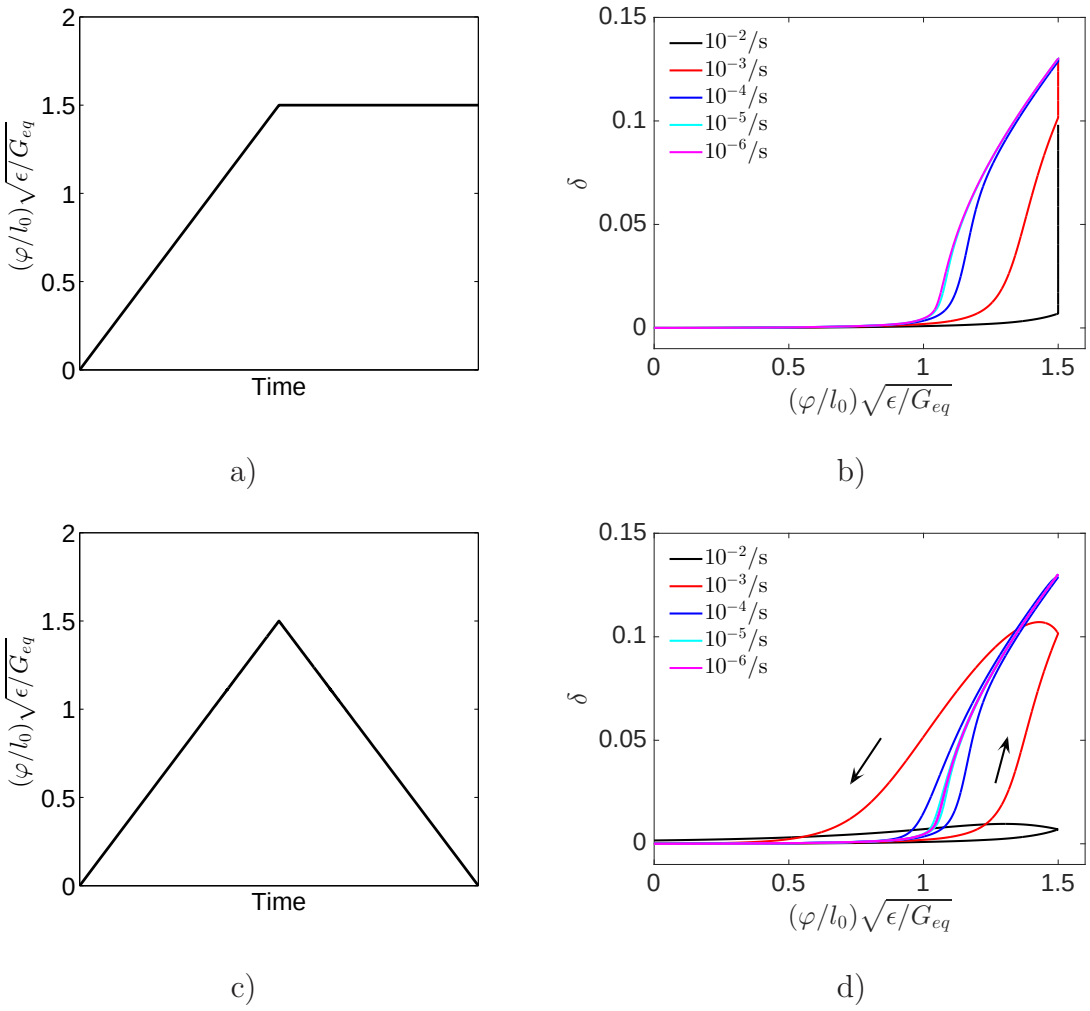

Figure 2.4 Results of electrocreasing simulations. a) Schematic of the applied normalized potential as a function of time for the monotonic/hold case. b) Simulated relative normalized displacement δ as a function of the applied normalized potential for the monotonic/hold case and ramp rates of $(\dot{\varphi}/l_0)\sqrt{\epsilon/G_{\text{eq}}} = 10^{-6}, 10^{-5}, 10^{-4}, 10^{-3}$, and 10^{-2}/s. c) Schematic of the applied normalized potential as a function of time for the load/unload case. d) Simulated relative normalized displacement δ as a function of the applied normalized potential for the load/unload case and the same set of ramp rates. Here the arrows indicate the direction of loading and unloading.

film at a critical value of the electric field – electrocreasing. Prior to electrocreasing, very little mechanical deformation occurs, and most of the free energy is electrostatic. The electrocreasing instability acts to relieve some of this electrostatic energy at the cost of localized mechanical strain energy in the region of the crease and reduces the total free energy of the layer. The creasing instability is distinct from a wrinkling

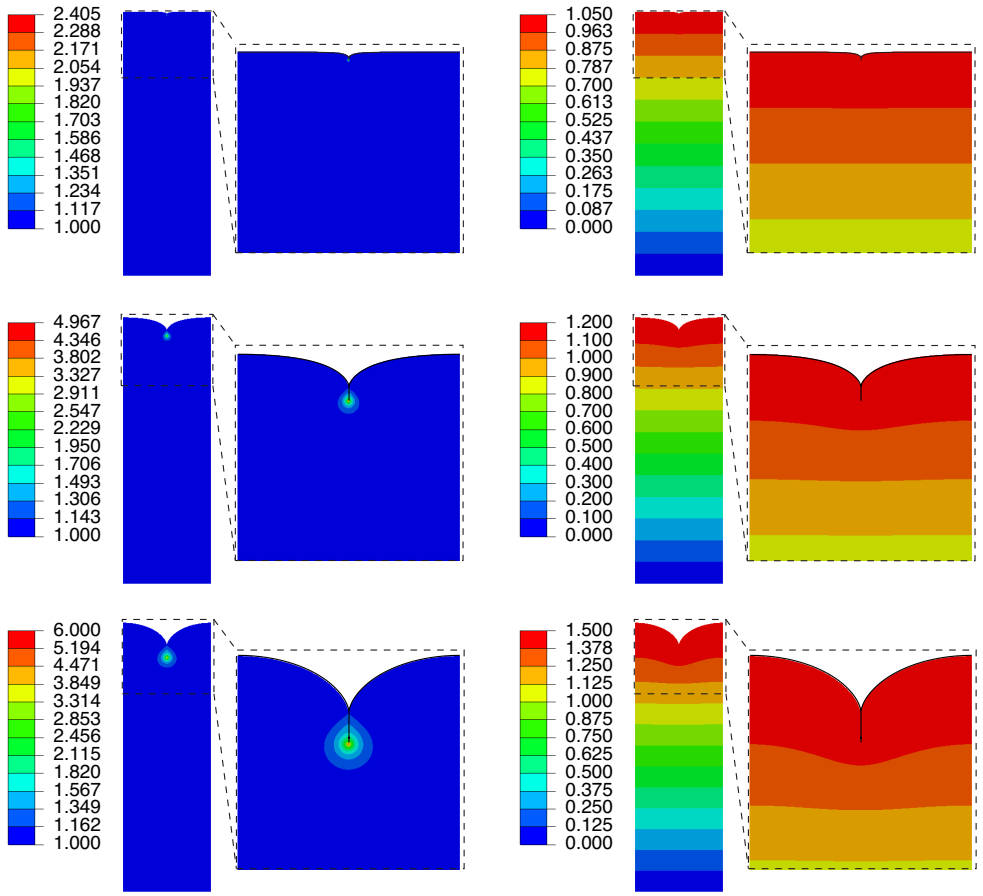

Figure 2.5 Simulation of a two-dimensional plane-strain crease at a single monotonic loading rate of $(\dot{\varphi}/l_0)\sqrt{\epsilon/G_{\text{eq}}} = 10^{-6}/\text{s}$. For clarity, the geometry has been mirrored about the symmetry plane, and the initial top surface of the soft dielectric layer is traced in black. Contour plots of a) the effective distortional stretch, $\bar{\lambda} = \sqrt{\text{tr}\,\mathbf{C}_{\text{dis}}/3}$, and b) the normalized electric potential field, $(\varphi/l_0)\sqrt{\epsilon/G_{\text{eq}}}$. The three rows correspond to applied normalized electric potentials of $(\varphi/l_0)\sqrt{\epsilon/G_{\text{eq}}} = 1.05, 1.20$, and 1.50.

instability in that it is inherently nonlinear and cannot be analyzed via linear perturbation. Hence, a nonlinear simulation capability provides a straightforward path for modeling this phenomenon.

Experimental observations of the electrocreasing instability have revealed that in the absence of prestretch, the surface pattern consists of randomly oriented creases

with aligned creases occurring when prestretch is applied in one direction [95, 94, 93]. Randomly oriented creases are inherently three-dimensional, and hence, modeling this case is computationally costly. For simplicity, we adopt a two-dimensional, plane-strain idealization – a common aspect of previous analyses [95, 66] – which assumes that the creases are regularly spaced and long relative to this spacing, as shown schematically in Figure 2.3a. The repeated nature of the assumed crease pattern enables modeling only a half cell, indicated by the dashed box in Figure 2.3a. The half cell geometry has initial thickness l_0 and half-width $l_0/6$ and is meshed with 3750 plane-strain user elements. We note that a small imperfection of $10^{-3}l_0$ is introduced at point A to serve as a geometric inhomogeneity to trigger the electrocreasing instability. By considering a single, plane-strain repeated unit, we have enforced that the soft dielectric layer is infinite in the lateral and out-of-plane directions, and by the scaling arguments for thin layers discussed in Appendix A of [35] jump boundary conditions may safely be neglected. Regarding mechanical boundary conditions, the surface CD is fixed, while the surfaces AD and BC are assigned the appropriate symmetry condition. The vertical dashed line represents a fixed, frictionless, rigid surface that serves to model the self-contact of surface AB once the crease forms. Regarding electrical boundary conditions, the bottom surface CD is set to ground, while the top surface AB is prescribed an electric potential history $\breve{\varphi}(t)$. To examine the effect of viscoelasticity on electrocreasing, we consider two forms of $\breve{\varphi}(t)$: (1) a monotonic ramp at fixed rate to the final normalized potential, which is subsequently held fixed, Figure 2.4a, and (2) a normalized potential ramp at fixed rate followed by unloading at that same rate, Figure 2.4c. For both forms, we consider a range of electric potential ramp rates $(\dot{\varphi}/l_0)\sqrt{\epsilon/G_{\text{eq}}} = 10^{-6}, 10^{-5}, 10^{-4}, 10^{-3}$, and 10^{-2}/s to the same final normalized potential of $(\varphi/l_0)_{\max}\sqrt{\epsilon/G_{\text{eq}}} = 1.5$.

Figure 2.5 shows contour plots for a simulation of the monotonic/hold case at an electric potential ramp rate of $(\dot{\varphi}/l_0)\sqrt{\epsilon/G_{\text{eq}}} = 10^{-6}$/s, where the geometry has been

mirrored about the symmetry plane for clarity. The left column shows contours of the effective distortional stretch, $\bar{\lambda} = \sqrt{\mathrm{tr}\,\mathbf{C}_{\mathrm{dis}}/3}$, and the right column shows contours of the normalized electric potential, $(\varphi/l_0)\sqrt{\epsilon/G_{\mathrm{eq}}}$. The three rows of Figure 2.5 correspond to applied normalized electric potentials of $(\varphi/l_0)\sqrt{\epsilon/G_{\mathrm{eq}}} = 1.05, 1.20,$ and 1.50, showing the evolution from a nearly flat surface to the onset of creasing to a deep crease with significant deformation. The size of the crease may be quantified through the normalized relative displacement of the top surface, $\delta = \left|u_2^{\mathrm{A}} - u_2^{\mathrm{B}}\right|/l_0$, i.e., the vertical displacement at point A (the tip of the crease) relative to the corner of the simulation domain at point B, normalized by the initial layer thickness l_0. We choose the measure δ since it clearly differentiates between homogeneous and crease-like deformation modes – i.e., the deformation is nearly homogeneous if $\delta \approx 0$, whereas as the crease forms and deepens, δ increases. Figure 2.4b shows the simulated normalized relative displacement δ as a function of the normalized electric potential for the monotonic/hold case and the full range of ramp rates, and Figure 2.4d summarizes δ versus the normalized electric potential for the load/unload case. From Figure 2.4b, we can see that the onset of the electrocreasing instability is delayed for faster ramps rates, but for sufficiently long subsequent hold times, the layer will form a crease regardless of the loading rate as the non-equilibrium mechanisms relax over time. However, for the load/unload case shown in Figure 2.4d, we observe that not all loading rates lead to a crease and that, once again, for transient, dynamic loading rates, viscoelasticity plays an important role – here possibly suppressing the creasing instability altogether.

Finally, we note that in Figures 2.4b and d the responses for the two slowest ramp rates (10^{-5} and 10^{-6}/s) are virtually identical, and for the load/unload case very little hysteresis is observed. Hence, as the electric potential ramp rate is decreased, we approach the equilibrium, time-independent, response. As measured experimentally [93] and corroborated by uncoupled electromechanical calculations

[95], in the equilibrium, plane-strain case, the onset of creasing occurs at a critical electric field of $(\varphi/l_0)_{\rm cr}\sqrt{\epsilon/G_{\rm eq}} \approx 1.03$, which agrees very closely with our finite element simulations at the slowest loading rate. Achieving this degree of quantitative agreement in fully-coupled finite-element simulations has remained elusive [65, 79] and points to the robustness of our simulation capability and its potential for predictive analysis of electromechanical instabilities.

2.5.3 Electrocavitation

A third distinct mode of electromechanical instability is electrocavitation, which – like electrocreasing – is a nonlinear instability involving inhomogeneous fields. However, unlike the electrocreasing instability, electrocavitation occurs in soft dielectrics that are highly constrained. Consider a defect, such as a fluid-filled bubble that may be introduced during processing (e.g., leftover base from the curing process), inside an otherwise homogeneous soft dielectric, which is under far-field mechanical constraint and subjected to an electric field. In the absence of the defect, the electric field will be constant, and since the soft dielectric is fully constrained, no deformation will occur. However, the presence of the defect introduces inhomogeneity in the fields and is accompanied by localized deformation around the defect. At some critical value of the applied far-field electric field, the deformation around the defect becomes unstable – the electrocavitation instability, which was first observed experimentally by [92]. In this section, we apply our simulation capability for DVEs to this mode of instability.

In our simulations, we consider a geometry consisting of a large DVE with a small, spherical, fluid-filled bubble in the center. Due to the symmetry of the problem, we employ an axisymmetric idealization in our simulations.[4] Figure 2.6a gives a three-dimensional view of the simulation domain rotated about the axis of symmetry, with the small bubble of initial radius R_0 highlighted, and Figure 2.6b shows the

[4]We note that this is in contrast to previous simulations of the electrocavitation instability, which employ a plane-strain assumption [65, 79].

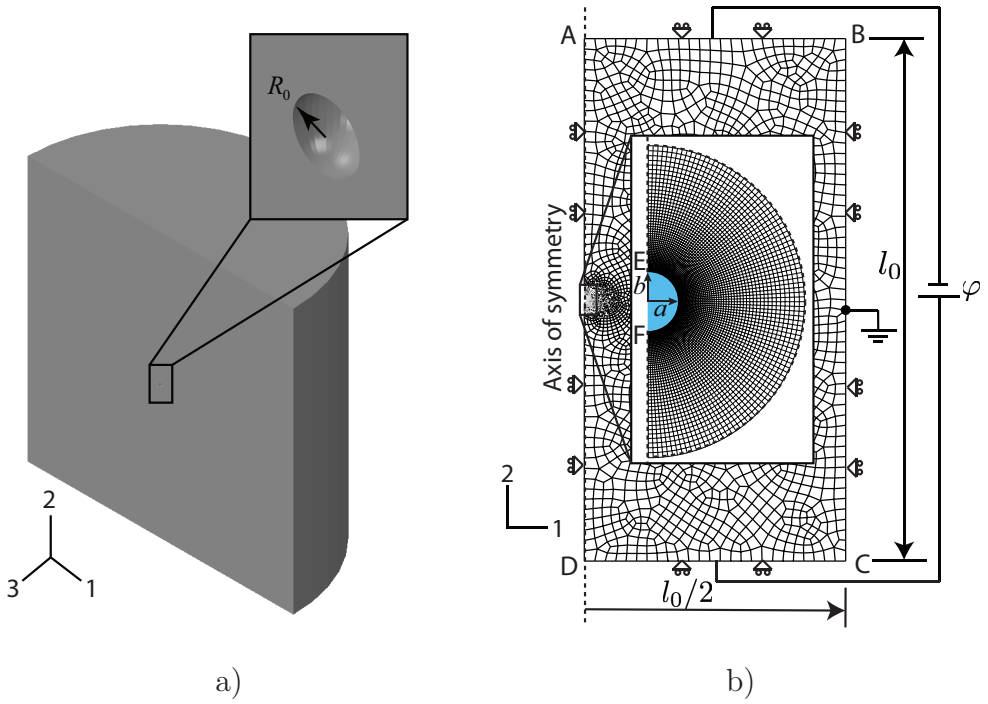

a) b)

Figure 2.6 Geometry, finite-element mesh, and electromechanical boundary conditions used in the axisymmetric electrocavitation simulations. a) Three-dimensional view of the simulation domain rotated about the axis of symmetry with an enlarged view of the fluid-filled bubble with initial radius R_0. b) Axisymmetric finite element mesh and boundary conditions. The bubble is highlighted in blue, and the nodes along the DVE/bubble interface are constrained to share the same electric potential.

axisymmetric finite element mesh, which consists of 7954 axisymmetric user-elements. For clarity, Figure 2.6b also shows the mesh in the immediate region of the fluid-filled bubble, shown in blue. The thickness and radius of the simulation domain are l_0 and $l_0/2$, respectively. The fluid-filled bubble is taken to be much smaller than the overall size of the full geometry, i.e., $R_0 \ll l_0$. Unlike in the electrocreasing simulations, no imperfection needs to be introduced, as the fluid-filled bubble serves as the inhomogeneity needed to trigger the instability.

Referring to Figure 2.6b, for the mechanical boundary conditions, in order to enforce the far-field constraint, faces AB, AE, FD, CD, and BC are assigned appropriate symmetry conditions while the DVE/bubble interface EF remains

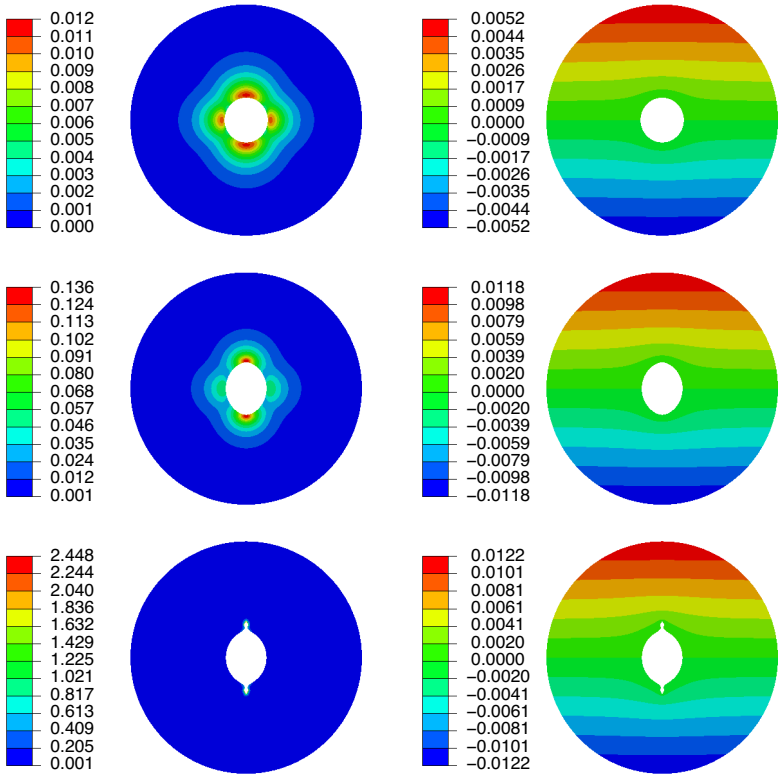

Figure 2.7 Simulation of axisymmetric electrocavitation at a single loading rate $(\dot{\varphi}/l_0)\sqrt{\epsilon/G_{\text{eq}}} = 10^{-5}$/s. For clarity, the body has been mirrored about the axis of symmetry, and the contour plots are limited to the immediate vicinity around the fluid-filled bubble. Contour plots of a) the maximum logarithmic strain, $\ln \lambda_1$ with λ_1 the maximum principal stretch, and b) the normalized electric potential field, $(\varphi/l_0)\sqrt{\epsilon/G_{\text{eq}}}$. The three rows correspond to applied normalized electric potentials of $(\varphi/l_0)\sqrt{\epsilon/G_{\text{eq}}} = 0.2, 0.45$, and 0.4646. We note that the strain contours corresponding to the maximum applied electric field (bottom left contour plot) indicate the extreme localization occurring after the onset of the electrocavitation instability.

traction-free. We take the bubble to be filled with an *incompressible* fluid, and in order to constrain the volume of the fluid-filled bubble to be constant throughout our simulations, we utilize the built-in fluid-filled-cavity constraint in [1].[5] In our simulations, we include the effect of surface energy at the DVE/bubble interface. In order to account for surface energy in our finite-element formulation, it is necessary

[5]We note that this constraint was neglected in previous simulations of electrocavitation [65, 79].

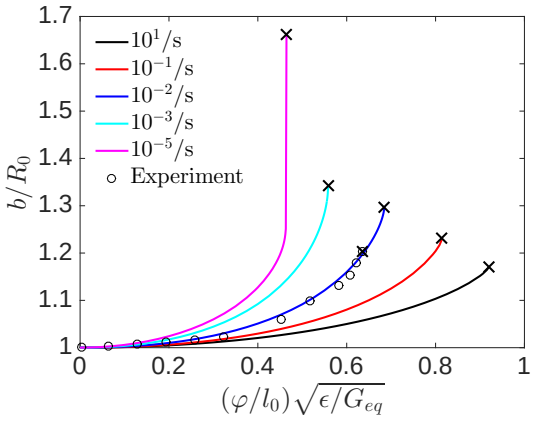

Figure 2.8 Simulated bubble deformation b/R_0 as a function of the applied normalized potential at constant ramp rates of $(\dot{\varphi}/l_0)\sqrt{\epsilon/G_{\text{eq}}} = 10^{-5}, 10^{-3}, 10^{-2}, 10^{-1}$, and 10^1/s for electrocavitation. The "×" symbols indicate the onset of instability for each case. Experimental data from [104] (for a different material system) is plotted with ∘ symbols.

to add an additional term to the displacement residual $(2.25)_1$:

$$(\mathbf{R}^{\gamma}_{\mathbf{u}})^A = -\int_{\mathcal{S}^{\text{e}}} \gamma \, \text{grad}_{\mathcal{S}} \, N^A \, da, \tag{2.26}$$

where γ is the surface energy density and $\text{grad}_{\mathcal{S}}$ is the surface gradient operator in the deformed configuration. For details regarding the derivation of this contribution to the residual and its calculation in the context of plane-strain and axisymmetric finite-elements, see [34]. In the experimental work of [92], the surface energy was in the range $\gamma/(G_{\text{eq}}R_0) = 0.1$ – 0.2, where the dimensionless quantity $\gamma/(G_{\text{eq}}R_0)$ is often referred to as the elasto-capillary number. Following their work, we take the surface energy to be given by $\gamma/(G_{\text{eq}}R_0) = 0.1$.[6] Regarding the electrical boundary conditions, we set the mid-side node on face BC to ground, while a time-dependent electric potential $\breve{\varphi}(t)/2$ is applied to face AB and $(-\breve{\varphi}(t)/2)$ to face CD so that the total far-field electric field is $(\varphi/l_0)\sqrt{\epsilon/G_{\text{eq}}}$ with the electric potential field symmetric about the bubble. The far-field electric field is then increased through a constant

[6]We have verified that we obtain very similar results when a smaller elasto-capillary number of 0.01 is used. See the recent work of [79] for an examination of the effect of large elasto-capillary numbers of up to approximately 10.

ramp rate $(\dot{\varphi}/l_0)\sqrt{\epsilon/G_{\text{eq}}}$. Furthermore, we assume the bubble to be filled with an *electrically conductive* fluid, and hence the electric potential is constrained to share the same value at all nodes on the DVE/bubble interface. Finally, we note that at the far-field boundaries it is appropriate to neglect jump conditions in our boundary conditions. Further, since the electric potential is constant in the fluid-filled bubble, the electric field in the bubble is zero and hence does not contribute to jump conditions at the DVE/bubble interface.

Figure 2.7 shows contour plots of the maximum logarithmic strain, $\ln \lambda_1$ with λ_1 the maximum principal stretch, (left column) and normalized electric potential, $(\varphi/l_0)\sqrt{\epsilon/G_{\text{eq}}}$, (right column) in the immediate vicinity of the fluid-filled bubble for a loading rate of $(\dot{\varphi}/l_0)\sqrt{\epsilon/G_{\text{eq}}} = 10^{-5}$/s and three different levels of far-field electric field $(\varphi/l_0)\sqrt{\epsilon/G_{\text{eq}}} = 0.2, 0.45$, and 0.4646. The presence of the fluid-filled bubble induces an inhomogeneous electric potential field that gives rise to inhomogeneous deformation in the surrounding DVE. As the electric potential increases, the bubble changes shape from a sphere to an ellipsoid with the bubble becoming more ellipsoidal as the electric field is increased (first and second rows of Figure 2.7). Above a critical electric field (third row of Figure 2.7), the geometry goes unstable, with sharp tips forming at the top and bottom of the bubble. This instability grows rapidly, and the simulations cease soon after the onset of instability. The deformation of the bubble prior to instability may be quantified through the ratio b/R_0, which is the deformed radius of the bubble along the direction of the applied electric field (as shown in Figure 2.6) normalized by the initial bubble radius. Figure 2.8 shows the ratio b/R_0 as a function of the normalized applied electric potential $(\varphi/l_0)\sqrt{\epsilon/G_{\text{eq}}}$ for a range of constant loading rates $(\dot{\varphi}/l_0)\sqrt{\epsilon/G_{\text{eq}}} = 10^{-5}, 10^{-3}, 10^{-2}, 10^{-1}$, and 10^{1}/s. The onset of electrocavitation is delayed with increasing loading rate, which is consistent with the results of previous sections.

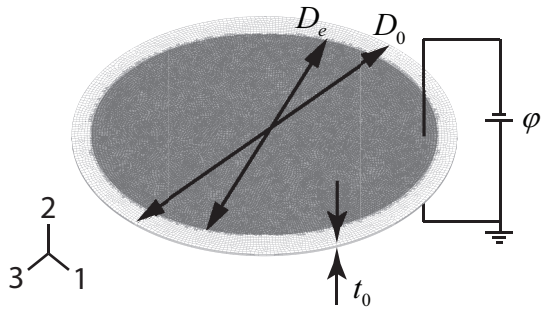

Figure 2.9 Finite-element mesh and electromechanical boundary conditions used in the three-dimensional pre-stretched diaphragm actuator simulations. Both sides of the soft dielectric disk have regions that serve as compliant electrodes, i.e., the active region, which are indicated by gray.

In Figure 2.8, we also plot the experimental data of [92], which was obtained using a different material system – Ecoflex rather than VHB 4910. Our simulation result for the case of $(\dot{\varphi}/l_0)\sqrt{\epsilon/G_{\text{eq}}} = 10^{-2}/\text{s}$ shows very nice agreement with the experimental data. The experiments of [92] utilized an electric potential ramp rate of 100 V/s, which when normalized by their reported layer thickness of 1.2 mm, shear modulus in the range 1.2 kPa to 4.6 kPa, and dielectric permittivity of $2.1\epsilon_0$, corresponds to a normalized ramp rate $(\dot{\phi}/l_0)\sqrt{(\epsilon/G_{\text{eq}})}$ in the range 0.53×10^{-2} /s to 1.04×10^{-2} /s. Hence, our numerical simulation and the experimental data correspond to similar loading rates and elasto-capillary numbers. While we stop short of claiming that this represents a direct comparison (since the mechanical time-dependence of Ecoflex and VHB 4910 are expected to be different), our simulation results are the first to the authors' knowledge to obtain this level of quantitative correspondence with experiments. Our results clearly demonstrate the importance of accounting for viscoelasticity in the interpretation of the instability threshold.

2.5.4 Wrinkling of a Pre-stretched Diaphragm Actuator

Finally, we move beyond the three idealized modes of electromechanical instability discussed in the prior sections and consider the electromechanically induced wrinkling

instability in a pre-stretched diaphragm actuator – a simple actuator configuration commonly used in application [70, 46]. A soft diaphragm actuator is prepared by (1) applying an equibiaxial pre-stretch to a thin soft dielectric layer, (2) fixing the edges of the pre-stretched layer to a frame to lock in the pre-stretch, (3) coating corresponding subregions on each side of the thin layer with conductive electrodes (we refer to this region of the thin layer as the active region) and (4) imposing an electric potential difference across the active region to actuate. Upon initial application of an electric potential difference, the active region will expand, which relieves some of the tensile stress in the thin layer. Once the applied electric potential difference is sufficiently high so as to induce compressive stress in some region of the thin layer, wrinkles will begin to form. We apply our numerical simulation capability to this configuration to illustrate the role of viscoelasticity in this mode of instability and to exercise our three-dimensional finite-element implementation.

In our numerical simulations, we consider a thin soft dielectric layer, which is circular in shape. Figure 2.9 shows the initial finite-element mesh and boundary conditions. The overall diameter of the undeformed soft dielectric layer is D_0 with a slightly smaller inner region of diameter, $D_e/D_0 = 0.914$, serving as the active region. The initial thickness of the layer is taken to be much smaller than its diameter, $t_0/D_0 = 0.0061$. The unstructured mesh consists of 90115 three-dimensional, eight-node brick user-elements with five elements through the thickness. To aid in triggering the onset of instability, all nodes on the top surface are prescribed a random geometric imperfection in the 2-direction on the order of $10^{-3}t_0$.

The simulation is performed in two steps. First, the thin layer is pre-stretched to a final equibiaxial stretch of 1.248. The pre-stretching is done very slowly to ensure that the non-equilibrium mechanisms remain approximately relaxed to minimize the effect of viscoelasticity in this step. Then, in the second step, while holding the outermost edge fixed, an electric potential difference is applied across the thickness of

the active region by setting the bottom electrode to ground and applying an electric potential $\breve{\varphi}(t)$ to the top surface at constant ramp rates of $(\dot{\varphi}/t_0)\sqrt{\epsilon/G_{\text{eq}}} = 3 \times 10^{-3}, 3 \times 10^{-2}$, and 3×10^{-1}/s.

Figure 2.10 shows the deformed shape and contours of the normalized vertical displacement, u_2/t_0, for the slowest loading rate of $(\dot{\varphi}/t_0)\sqrt{\epsilon/G_{\text{eq}}} = 3 \times 10^{-3}$/s. Figure 2.10a shows the deformed shape just after the onset of wrinkling at a normalized electric potential of $(\varphi/t_0)\sqrt{\epsilon/G_{\text{eq}}} = 0.32$, and Figure 2.10b shows the deformed shape well beyond the onset at a potential of $(\varphi/t_0)\sqrt{\epsilon/G_{\text{eq}}} = 0.36$, just prior to the onset of the pull-in instability locally at some point in the layer. It is clear that wrinkling of the initially flat sheet is accompanied by significant inhomogeneous, out-of-plane deformation. Further, Figure 2.11 shows u_2/t_0 at the center of the actuator as a function of applied electric field for all three loading rates considered. The onset of the wrinkling instability is clear from the point at which u_2/t_0 becomes non-zero, and the subsequent onset of the pull-in instability at some point in the thin layer is marked by a "×". As in our prior discussion of other modes of instability, the onset of wrinkling is delayed and occurs at a higher normalized electric potential as the loading rate is increased.

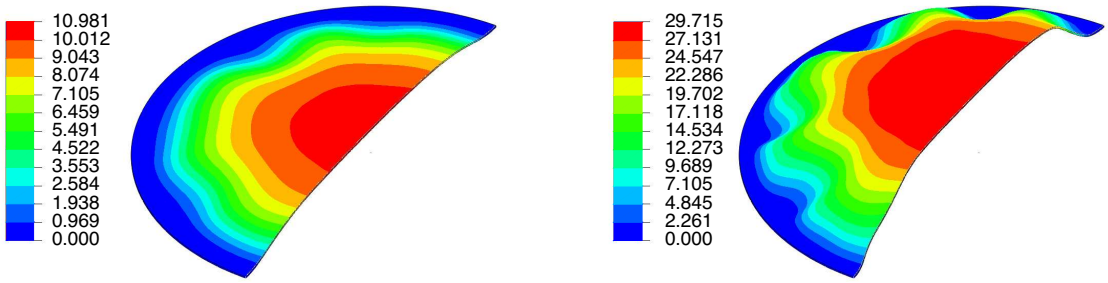

a) b)

Figure 2.10 Deformed shape and contours of the normalized vertical displacement u_2/t_0 for the pre-stretched diaphragm actuator simulation at a loading rate of $(\dot{\varphi}/t_0)\sqrt{\epsilon/G_{\text{eq}}} = 3 \times 10^{-3}$ /s and normalized electric potentials of a) $(\varphi/t_0)\sqrt{\epsilon/G_{\text{eq}}} = 0.32$, immediately after the onset of wrinkling, and b) $(\varphi/t_0)\sqrt{\epsilon/G_{\text{eq}}} = 0.36$, long after the onset of wrinkling but just prior to pull-in. For clarity, the mesh is not shown, and only half of the body is displayed.

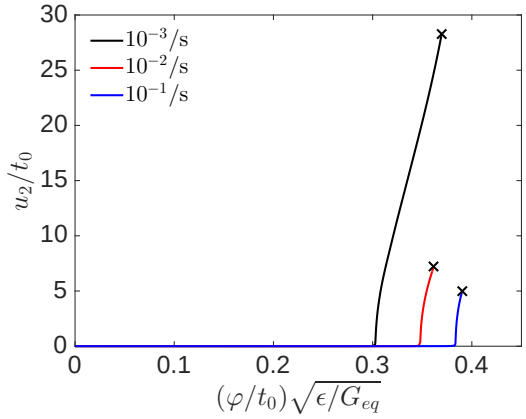

Figure 2.11 Simulated normalized vertical displacement, u_2/t_0, at the center of the diaphragm actuator as a function of the applied normalized potential for loading rates $(\dot{\varphi}/t_0)\sqrt{\epsilon/G_{\text{eq}}} = 3 \times 10^{-3}, 3 \times 10^{-2}$, and 3×10^{-1}/s. The "×" symbol denotes the onset of the pull-in instability locally at some point in the thin soft dielectric layer.

CHAPTER 3

EXPERIMENTAL CHARACTERIZATION AND CONTINUUM MODELING OF INELASTICITY IN FILLED RUBBER-LIKE MATERIALS

3.1 Introduction

Before beginning the discussion, it is necessary to make clear the difference between *virgin* and *preconditioned* material. In what follows, we consider *virgin* material that which is used directly in raw form, without any prior loading. On the other hand, *preconditioned* material has been cycled under load multiple times. As is well known [18, 19], preconditioning eliminates stress-softening, also known as Mullins effect, from the material response.

While the overall purpose is to consider filled rubbers in general, we will use Viton for our experiments. Viton is a popular material on the market for O-rings and other seals, and it exhibits a rich inelastic mechanical behavior. For example, Figure 3.1 shows the results of uniaxial load/unload/reload tests and multi-step stress relaxation tests on virgin Viton. Some of the key features observed in Figure 3.1a include stress-softening behavior (also known as the Mullins effect) and rate-dependent behavior, while in Figure 3.1b, one clearly observes inelasticity, as well as an asymmetry between loading and unloading.

The literature on the mechanical behavior of filled rubber-like materials has a long history, especially the phenomenon of stress softening. Stress softening occurs when virgin material is subjected to cyclic loading, the stress response becomes much softer during the reloading path and becomes stiffer again while experiencing a successive stretch. This phenomenon was first intensively studied in the seminal

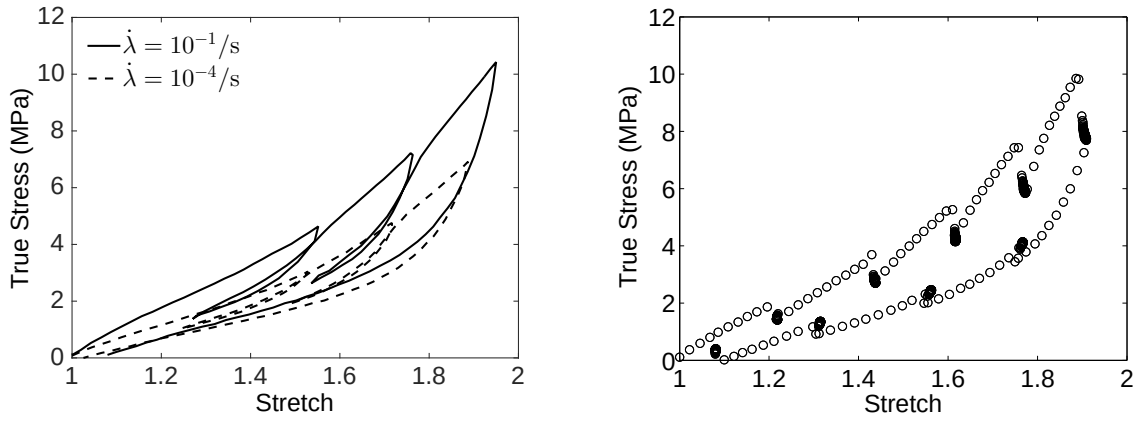

Figure 3.1 Uniaxial tensile tests on virgin Viton. a) Load/unload/reload test results at two different stretch rates, and b) multi-step stress relaxation test results.

work by [59] over a half century ago, and stress-softening is now widely known as the Mullins effect.

While there is still not a widely agreed upon physical explanation for the Mullins effect, numerous models exist in the literature. Some early phenomenological models [61, 62, 31, 32] treat the filled rubber-like material as an amorphous structure composed of hard and soft phases. The hard phase represents the filler and the soft phase represents the rubber matrix. Each material point is assumed to begin with a majority as the hard phase, and upon stretching, an irreversible phase change to soft occurs, only if the stretch is greater than any previously attained. More recently, models based on this approach have again found success [5, 6, 71]. Another phenomenological approach for modeling stress softening is through a continuum damage mechanics, or pseudo-elastic approach [83, 56, 63, 18, 19]. Here a damage parameter is introduced that evolves with deformation to model the breakup of hard filler particles and clusters. Lastly, micro-mechanics based models have also found success in modeling the Mullins effect [25, 44, 54]. These models are typically based on the statistical mechanics of chain rupture or filler cluster rupture.

Next, turning attention to the rate-dependent behavior of filled rubber-like materials, many experimental observations [49, 50, 4, 6, 58] show that filled rubber-like materials exhibit creep, stress relaxation, as well as hysteresis loops in cyclic loading. There are numerous phenomenological and micro-mechanicanics based models found in the literature. Some previous phenomenological works [36, 50, 40] use stress-like internal variables with constitutive evolution equations to model the observed behavior. Similarly, another approach splits the deformation gradient into elastic and inelastic contributions, which leads to constitutive equations for the inelastic deformation [52, 83, 73, 4]. As for micro-mechanics approaches, [57] proposed a micro-sphere model that accounts for viscous effects, [48] based on transient network theory introduced by [26] developed a fully physically based constitutive model.

In comparison, the literature is meager when considering the combined stress-softening and viscous behavior of rubber-like materials. Of those works that consider both, [83] was an early attempt for a fully nonlinear viscoelastic model incorporating a simple isotropic damage mechanism. In the years that followed a few other works may be found [58, 72] combining ideas from both Mullins effect and viscoelasticity, however, not all of them were for filled rubber-filled materials, and none of them dealt with the asymmetric inelastic response between loading and unloading. Most recently, [51] and [53] have developed a combined model for capturing the complex behavior of tough gels, which also exhibits a very rich inelastic response.

As mentioned earlier, most of the existing constitutive models found in the literature attempt to either predict the quasi-static stress-softening effect, *or* rate-dependent viscous effects. However, two effects are equally important. *The overall goal of this paper is to develop a validated constitutive model for filled rubber-like materials that accounts for stress-softening and viscous effects concurrently.*

Because of the limited data available in the literature, we conducted a series of experiments to measure the combined viscoelastic and stress-softening behavior of

Viton. With the purpose to decouple the combined behavior for ease of analysis and interpretation, three different types of uniaxial tension experiments were conducted. Specifically, the experiments are 1) quasi-static load/unload/reload tests on virgin specimens to provide information on the stress-softening behavior in the absence of viscous effects; 2) load/unload tests, as well as multi-step stress relaxation tests on preconditioned specimens to obtain the rate-depenedent behavior without any influence from stress-softening; and 3) both load/unload/reload tensile tests and multi-step stress relaxation tests on virgin specimens to obtain the total combined behavior.

For our constitutive model, we treat the stress-softening effect as hard/soft phase transition [71] and use a micro-mechanics based model [48] to capture viscous effects. The novelty in the model comes from the introduction of a scalar internal variable responsible for stretch dependence of the viscous response, as well as controlling the asymmetric response between loading and unloading. The numerical implementation of the model takes the form of a user material subroutine (UMAT) in [1]. The proposed model was calibrated to uniaxial experiments using a nonlinear least square method, and an inhomogeneous deformation experiment was used to validate the constitutive model.

3.2 Experiments

There is very limited data in the literature that probes the combined stress-softening and viscoelastic behavior of rubber-like materials. As mentioned in Section 3.1, all the experiments that follow will focus on the specific material Viton. Accordingly, in this section we summarize our set of comprehensive mechanical uniaxial tensile tests performed at room temperature. Our intention is to first decouple the measured response as much as possible for ease of analysis, and after that return to the fully combined behavior. Our experimental program involves the following components:

1. quasi-static load/unload/reload tests on virgin specimens;

2. quasi-static load/unload and multi-step stress relaxation tests on preconditioned specimens;

3. load/unload tests at various rates on specimens preconditioned to different stretch levels;

4. and, load/unload/reload tests at various rates and multistep relaxation tests on virgin specimens.

3.2.1 Specimens and Setup

Raw material was purchased in the form of 152.4 mm (6 in) square sheet with a thicknesses of $t_0 = 2.08\,\text{mm}$. From the raw material flat dog-bone specimens were cut using an ASTM D638-V specimen cutting die with a width of $w_0 = 3.18\,\text{mm}$ and length of $l_0 = 9.49\,\text{mm}$ in the gauge section. After cutting, the initial cross sectional area, A_0, in the gauge section was $6.553 \times 10^{-6}\,\text{m}^2$. A permanent marker was used to draw white dots in the gauge section of each specimen for the purpose of Digital Image Correlation (DIC) strain measurements as shown in Figure 3.2. All experiments were conducted at room temperature on a uniaxial tension testing machine.

As mentioned earlier, we consider a *virgin* specimen one which was cut from the raw stock and tested directly thereafter. On the other hand a *preconditioned* specimen is one which was cut from the raw stock, cycled in uniaxial tension no less than 5 times, and then left to relax overnight before further testing. As is well known [18, 19], preconditioning eliminates stress-softening from the material response and we exploit that here as well.

Figure 3.2 Typical Viton specimen cut from a larger sheet using an ASTM D638-V die.

3.2.2 Procedures and Analysis

Typically in rubber-like materials the stretch is used in place of typical strain measures. Under uniaxial conditions, the stretch is defined by

$$\lambda = \frac{l}{l_0} = 1 + \frac{u}{l_0}, \tag{3.1}$$

where l_0 the initial length of the gauge section, l is the current length of the gauge section, and u the displacement. Using DIC, we are able to directly measure λ since l is the distance between the white marks, and l_0 is simply the measurement prior to deformation. Since we wish to load at a constant *stretch-rate* to asses the scale of viscoelastic effects in the material, for a given set of prescribed experimental conditions $\{\dot{\lambda}, l_0\}$ the corresponding constant loading velocity is given by

$$\dot{u} = \dot{\lambda} l_0 \,. \tag{3.2}$$

We note that under uniaxial conditions the true strain ϵ, and engineering strain e, may be computed from the stretch by the simple relations $\epsilon = \ln(\lambda)$, and $e = \lambda - 1$, respectively.

As for the stress measures, when analyzing the experiments, we assume that the material is incompressible and therefore the true stress under uniaxial tension is given by

$$\sigma = \frac{F}{A_0}\lambda, \tag{3.3}$$

where F is the measured force, A_0 the undeformed cross sectional area of the specimen within its gauge length section and λ the measured stretch. We have used a 5 lb load cell (Transducer Techniques MDB-5) to measure the force in the specimen.

3.2.3 Quasi-static Load/Unload/Reload on Virgin Specimens

Previous research shows that the Mullins effect is rate-independent [58, 18, 71]. In this first set of experiments, for the purpose of probing the Mullins effect without any influence from viscous effects, we conducted quasi-static load/unload/reload tests at a stretch rate of $\dot{\lambda} = 10^{-4}$/s on *virgin* specimens. We note that the data presented here is one of three nearly identical tests.

A schematic of the prescribed stretch as a function of time is shown in Figure 3.3a. In order to prevent the specimen from going into compression during every unloading cycle, we intentionally made the stretch profile 'ladder' like.[1] The corresponding true stress - stretch curve is shown in Figure 3.3b. After an initial loading to a stretch of 1.5, it is clear that the specimen "softens" during the unloading. Then, upon reloading, the stress follows the unloading curve, until reaching a stretch of 1.5, after which it continues the initial loading curve to a stretch of 1.75. The process is repeated for the remaining load-unload cycles and this observation indicates stress-softening (Mullins effect) is present. This experiment will be used later, for calibrating material parameters in the constitutive model.

3.2.4 Tests on Preconditioned Specimens

Previous work in the literature [18, 19] used a preconditioning procedure on virgin specimens in order to eliminate the Mullins effect from the subsequent mechanical response. We performed a similar preconditioning procedure here, where a cyclic

[1]Since our uniaxial tensile testing machine is unable to use input from the load cell, we are unable to reverse the crosshead in real time based on event detection, and therefore must prescribe an appropriate stretch profile to ensure the specimen never goes into compression.

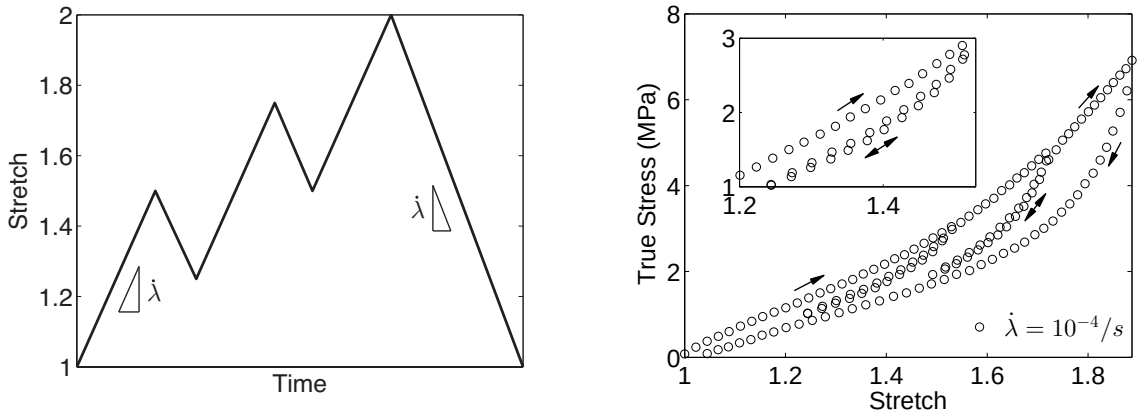

a) b)

Figure 3.3 a) Schematic of the prescribed stretch history, and b) corresponding true stress - stretch behavior for our quasi-static load/unload/reload tensile tests on virgin specimens. Arrows indicate the direction of loading/unloading.

loading to a maximum stretch of $\lambda = 2.5$ was prescribed for at least 5 cycles. After letting the preconditioned specimens relax overnight, those same specimens were then used to measure the viscous response without any influence from the Mullins effect.

Multi-step stress relaxation tests [4, 6, 38] were performed on the preconditioned specimens. In these multi-step tests, within each step, a rapid (2.54 mm/s) step in displacement was applied, then the position was held fixed for 2000 seconds to allow for stress relaxation. That procedure is then repeated multiple times for loading as well as unloading to perform the full multi-step relaxation test, the schematic is shown in Figure 3.4a. Additionally, quasi-static uniaxial tests were conducted on preconditioned specimens for comparison. We note that all experiments on preconditioned specimens were limited to a maximum stretch of $\lambda = 2.5$, which was the stretch used for preconditioning, and the results shown are chosen form one of three nearly identical tests.

The stress - stretch response is shown in Figure 3.4b for both multi-step relaxation and quasi-static load/unload tests. First, considering the quasi-static results, typical rubber-like material behavior is observed — very little dissipation and

evidence of limited extensibility. Next turning attention to the multi-step relaxation results, it is clear that viscous effects are present by the increase in stress when ramping, followed by relaxation during the hold period. Lastly, since the relaxed state coincides with the quasi-static results, we consider the quasi-static result to be the equilibrium behavior.

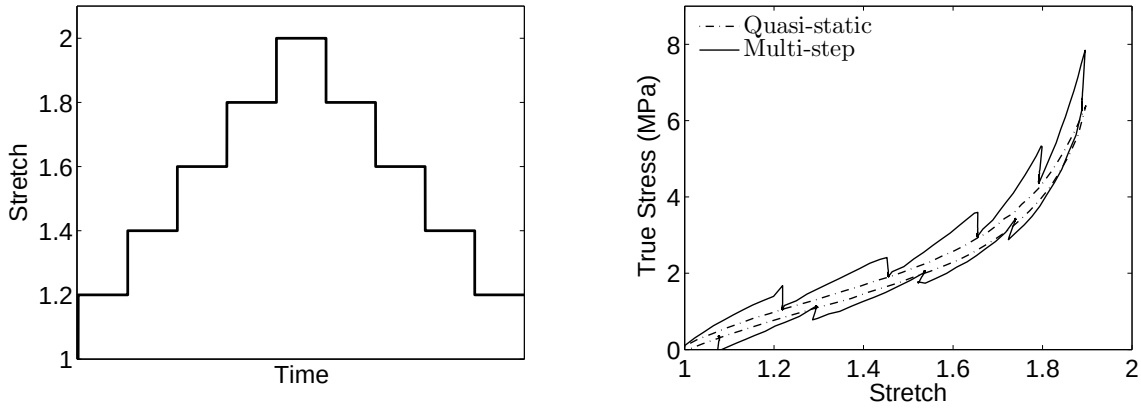

a) b)

Figure 3.4 Experimental results for preconditioned specimens. a) Schematic of stretch history for multi-step stress relaxation, b) measured stress-stretch response, a quasi-static load/unload and a multi-step stress relaxation test are superimposed.

Based on the data in Figure 3.4, there is a clear stretch dependent stiffening, as well as asymmetry in viscous response during loading and unloading, prompting further analysis. First, the stiffness was measured at the beginning of each loading, and unloading, step by taking the slope of the stress - stretch curve in the multi-step relaxation experiment. Then, the stiffness of the quasi-static tension test was also measured at that same stretch. Figures 3.5a and 3.5b show the stiffness measurements superimposed on the stress - stretch curves for loading and unloading, respectively. In Figures, 3.5a and 3.5b, red lines indicate the stiffness from the multi-step relaxation experiment, while blue lines are the stiffness measured form the quasi-static tension test.

Based on a comparison between the stiffnesses in Figures 3.5a and 3.5b, there are clear observations to be made. The most important observation is that the difference in stiffness between the two experiments is evident during loading, while nearly insignificant during unloading. Second, during loading, there is an increase in the amount of viscous strain stiffening with stretch. To quantify these observations, we assume the quasi-static test is representative of only the equilibrium response of the material, and the response of the material during the stretch increments of the multi-step relaxation to include only equilibrium and viscous contributions since these samples were preconditioned.

In Figures 3.5c and 3.5d, the measured stiffnesses were plotted against the measured stretch for loading and unloading, respectively. The viscous stiffness is computed as the difference between the total response and the quasi-static response for each fixed stretch. As mentioned, there is a trend that shows the viscous stiffness also strain stiffens, and that the equilibrium response alone cannot account for the observed strain stiffening behavior. Further, this behavior is not observed during unloading, where there is very little viscous strain stiffening relative to loading.[2] These observations will be used as guidance for constitutive model development.

Lastly, a suite of experiments were performed to assess the coupling between the Mullins effect and the non-equilibrium response. First, virgin specimens were preconditioned to three different levels of macroscopic stretch, $\lambda^{\max}$. After sitting overnight, load/unload tests were performed on those specimens at different stretch rates. From those experiments, the viscous stress was measured by taking the difference between the total stress (at a fixed rate) and the quasi-static stress. Figure 3.6 shows the measured viscous stress plotted against the macroscopic stretch at two different rates. What we observe from Figure 3.6 is that the viscous stress is

[2]Such behavior has been previously observed in other classes of materials. For example, [53], used the phrase asymmetric rate-sensitivity, to describe similar behavior in double network hydrogels.

essentially unaffected by $\lambda^{\max}$ used for preconditioning, and therefore we consider the non-equilibrium response unaffected by the Mullins effect.

3.2.5 Tests on Virgin Specimens

After considering the Mullins effect and viscous effects separately, we now bring attention back to the overall combined behavior. Similar to the discussion in Section 3.2.3, load/unload/reload tests on *virgin* specimens were conducted using two stretch rates of $\dot{\lambda} = 10^{-1}$/s and $\dot{\lambda} = 10^{-2}$/s, both of which are at a stretch rate where viscous effects are expected. Also, multi-step stress relaxation tests on virgin specimens were conducted in a similar manner to those in Section 3.2.4. The results of these experiments are shown in Figure 3.7.

Figure 3.7a shows the results for load/unload/reload tensile tests at multiple stretch rates, including quasi-static. The behavior clearly shows elements of Mullins effect, as well as rate-dependence. Figures 3.7b and 3.7c show the results for the multi-step relaxation experiment. From Figure 3.7b, as is expected, the stress clearly decays over time within each step. And Figure 3.7c shows that the steady stress values after relaxation from loading and unloading do not coincide, with much more hysteresis than the quasi-static preconditioned test. A clear indicator of the dissipation caused by the Mullins effect. These experiments, which measure the combined response, will be employed later for model calibration.

3.3 Continuum Framework

In this section we cover the kinematics and governing equation from a continuum mechanics perspective to describe the nonlinear mechanical behavior of filled rubber-like materials.

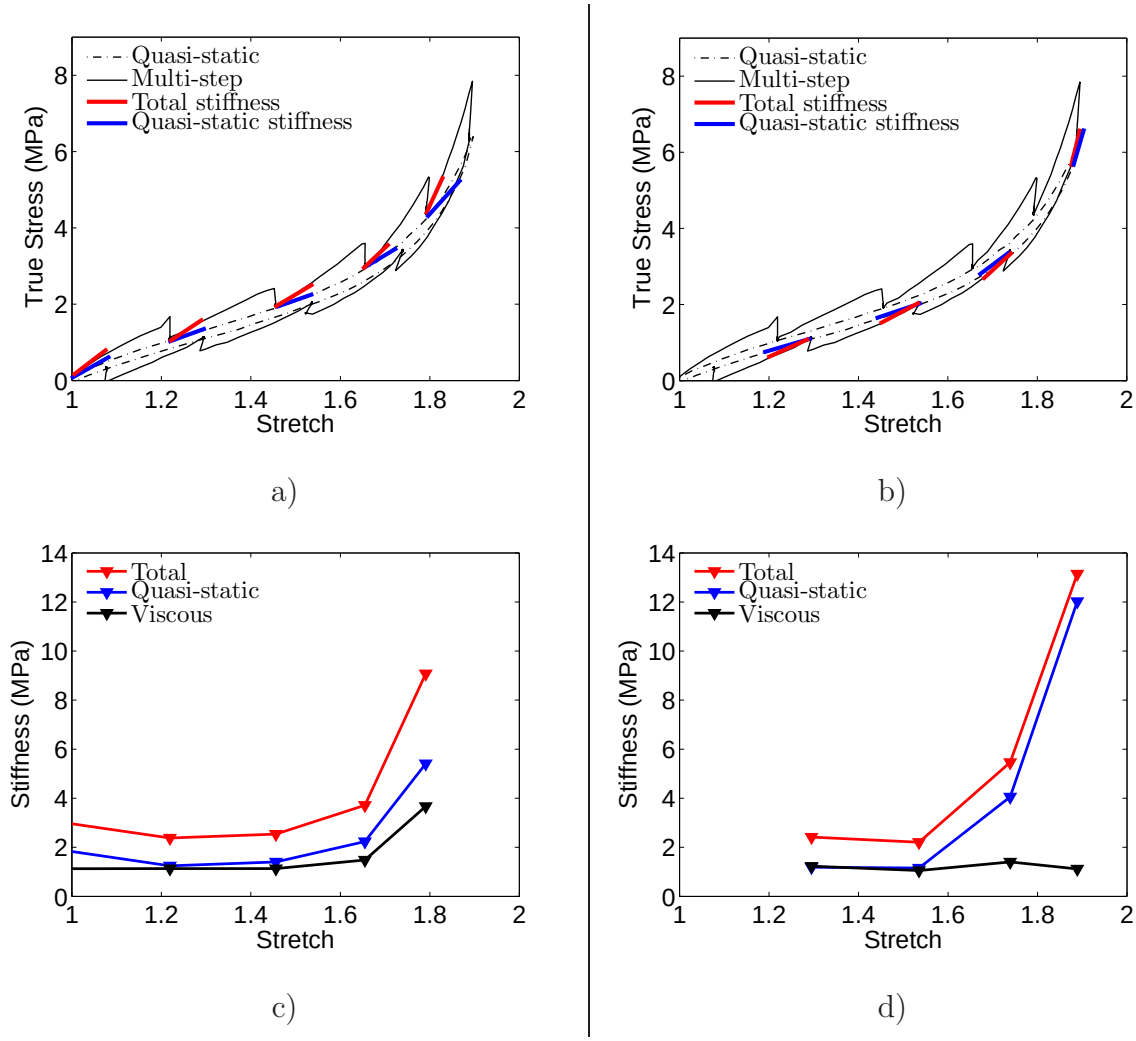

Figure 3.5 Quasi-static load/unload and multi-step stress relaxation tests performed on preconditioned specimens. The stiffness, a) measured at the beginning of each loading increment, and b) unloading increment, superimposed on the stress - stretch curves. Stiffness in c) loading, and d) unloading, plotted against stretch, the viscous stiffness is calculated by taking the difference between total and quasi-static stiffness.

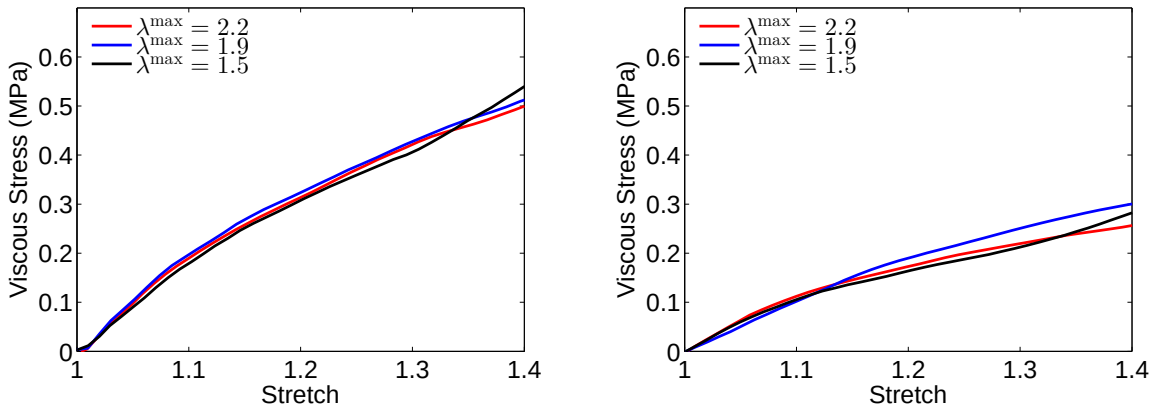

a) b)

Figure 3.6 The viscous stress, measured as the quasi-static subtracted from the total, plotted against macroscopic stretch for multiple levels of $\lambda^{\max}$ used for preconditioning at a rate of a) $\dot{\lambda} = 10^{-1}/\text{s}$, and b) $\dot{\lambda} = 10^{-2}/\text{s}$.

3.3.1 Kinematics

Consider a body $\mathcal{B}_{\text{R}}$ identified with the region of space it occupies in a fixed reference configuration, and denote by $\mathbf{x}_{\text{R}}$ an arbitrary material point of $\mathcal{B}_{\text{R}}$. The referential body $\mathcal{B}_{\text{R}}$ then undergoes a motion $\mathbf{x} = \boldsymbol{\chi}(\mathbf{x}_{\text{R}}, t)$ to the deformed body $\mathcal{B}_t$ with deformation gradient given by[3]

$$\mathbf{F} = \nabla\boldsymbol{\chi}, \quad \text{such that} \quad J = \det \mathbf{F} > 0. \tag{3.4}$$

The right and left Cauchy-Green deformation tensors are given by $\mathbf{C} = \mathbf{F}^{\top}\mathbf{F}$ and $\mathbf{B} = \mathbf{F}\mathbf{F}^{\top}$, respectively. The deformation gradient admits the polar decomposition, $\mathbf{F} = \mathbf{R}\mathbf{U}$, where $\mathbf{R}$ is a rotation and $\mathbf{U}$ the stretch, with $\mathbf{U} = \sqrt{\mathbf{C}}$. We assume that the material is *nearly*-incompressible, and introduce the distortional part of the deformation gradient, defined as

$$\mathbf{F}_{\text{dis}} = J^{-1/3}\mathbf{F} \quad \text{so that} \quad \det \mathbf{F}_{\text{dis}} = 1. \tag{3.5}$$

[3]The symbols ∇ and Div denote the gradient and divergence with respect to the material point $\mathbf{x}_{\text{R}}$ in the reference configuration; while grad and div denote these operators with respect to the point $\mathbf{x} = \boldsymbol{\chi}(\mathbf{x}_{\text{R}}, t)$ in the deformed configuration.

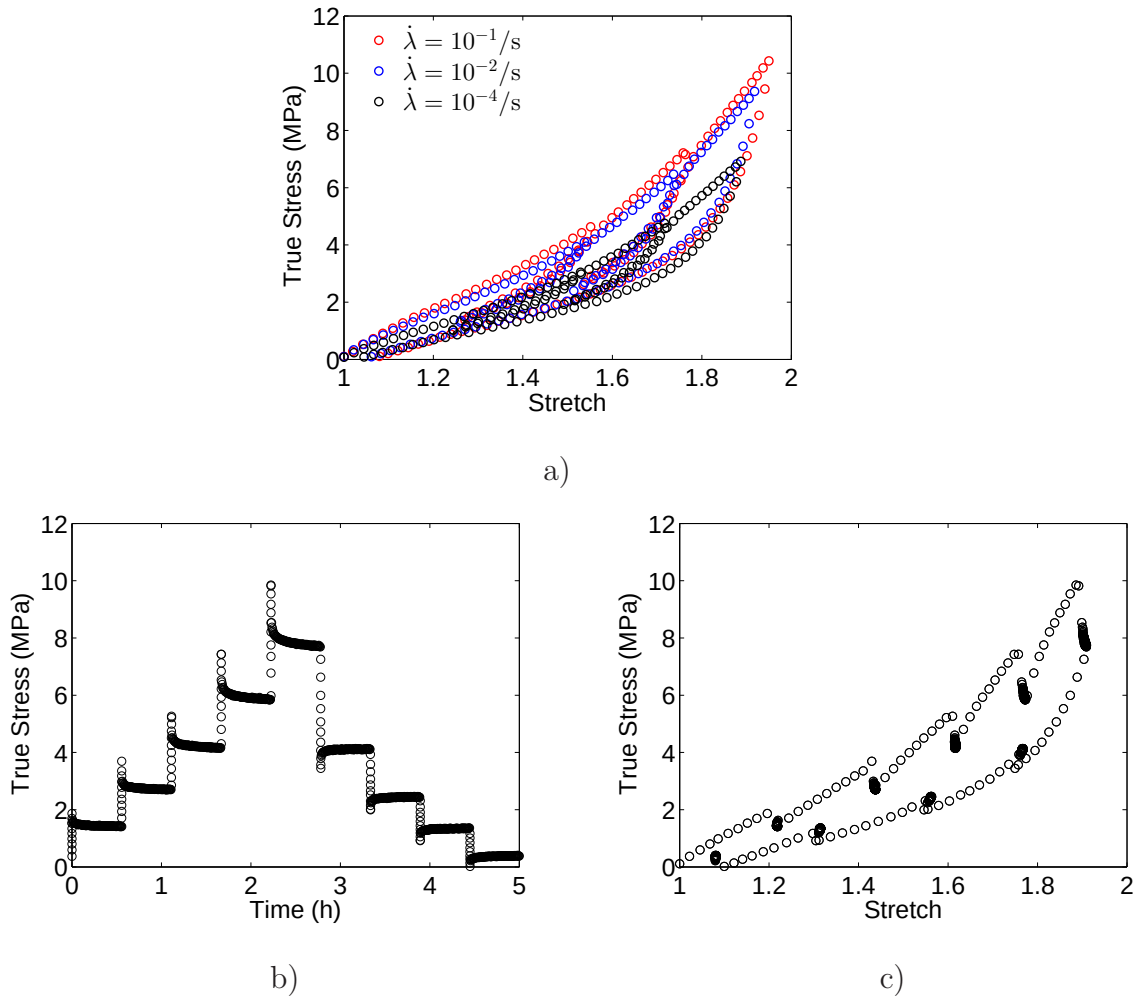

Figure 3.7 Uniaxial tensile test results on virgin specimens. a) Load/unload/reload tests at multiple stretch rates. b) True stress as a function of time, and c) the corresponding true stress - stretch curve, in a multi-step stress relaxation test.

The distortional right and left Cauchy-Green deformation tensors are then $\mathbf{C}_{\text{dis}} = \mathbf{F}_{\text{dis}}^{\top}\mathbf{F}_{\text{dis}} = J^{-2/3}\mathbf{C}$ and $\mathbf{B}_{\text{dis}} = \mathbf{F}_{\text{dis}}\mathbf{F}_{\text{dis}}^{\top} = J^{-2/3}\mathbf{B}$. In what follows, the effective stretch is given by

$$\bar{\lambda} = \sqrt{\operatorname{tr}\mathbf{C}_{\text{dis}}/3}\,. \tag{3.6}$$

3.3.2 Stress Softening Variables

We treat filled rubber-like materials as a composite system of "hard" filler and a "soft" rubber matrix, where the filler volume fraction is denoted by ν_{f}, and the volume fraction of soft domain is $\nu_{\text{s}} = 1 - \nu_{\text{f}}$. One possible explanation for the Mullins effect is that deformation breaks up hard regions, so that the effective soft domain fraction increases. Such an evolution equation is constitutive and will be prescribed in the following sections.

Further, following [61], when this class of material undergoes an arbitrary deformation, the hard filler accommodates much less of the overall deformation than the soft rubber matrix. Therefore, an amplified stretch

$$\Lambda = \sqrt{X(\bar{\lambda}^2 - 1) + 1} \tag{3.7}$$

is used for the rubber matrix, where X is a amplification factor and it usually depends on the volume fraction ν_{s}, and the shape of the filler.

3.3.3 Equilibrium

We consider that the body $\mathcal{B}_t$ is at equilibrium, neglecting any inertial effects and body forces, the balance of momentum in the deformed body $\mathcal{B}_t$ is expressed as

$$\operatorname{div}\mathbf{T} = \mathbf{0} \quad \text{and} \quad \mathbf{T} = \mathbf{T}^{\top}, \tag{3.8}$$

where $\mathbf{T}$ is the Cauchy stress. Further, (4.6) serves as the governing equation for the displacement field. The boundary of the deformed body $\partial\mathcal{B}_t$ has outward unit

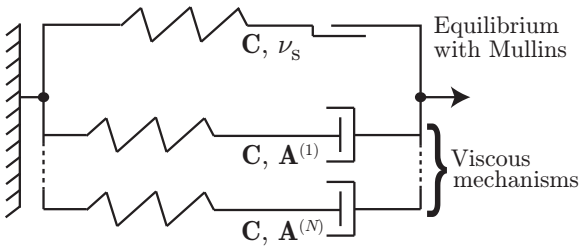

Figure 3.8 Rheological schematic of the constitutive model. The rate-independent mechanism is represented by an equilibrium spring connected to a "slider" to describe the Mullins effect, while the rate-dependent mechanism employs multiple spring and dashpot systems connected in parallel to describe the viscous behavior.

normal $\mathbf{n}$, and the external surface traction on an element of the deformed surface $\partial\mathcal{B}_t$ is given by

$$\mathbf{t} = \mathbf{T}\mathbf{n}. \tag{3.9}$$

3.4 Constitutive Equations

Taking the guidance from the experiments in Section 3.2, we assume that mechanical response of filled rubber-like materials is the combination of i) a rate-independent portion which includes an equilibrium mechanism with Mullins effect and ii) a rate-dependent portion that includes multiple viscous mechanisms denoted by $\alpha = 1, 2, ..., N$ to capture the viscous response using tensorial internal variables $\mathbf{A}^{(\alpha)}$. A rheological schematic of the model is shown in Figure 3.8.

3.4.1 Free Energy

We assume that the free energy per unit reference volume $\hat{\psi}_{\mathrm{R}}$ is additively decomposed into (1) a contribution from the rate-independent mechanism $\hat{\psi}_{\mathrm{R}}^{\mathrm{RI}}$, which is a function of right Green Cauchy stretch tensor $\mathbf{C}$ and volume fraction of soft domain ν_{s}, and (2) $\alpha = 1, \ldots, N$ contributions from each of the rate-dependent mechanisms $\hat{\psi}_{\mathrm{R}}^{\mathrm{RD}(\alpha)}$, each of which is a function of both $\mathbf{C}$ and stretch like tensorial internal variables $\mathbf{A}^{(\alpha)}$.

Therefore the total free energy is given by the form

$$\hat{\psi}_{\mathrm{R}}(\mathbf{C}, \nu_{\mathrm{s}}, \mathbf{A}^{(\alpha)}) = \hat{\psi}_{\mathrm{R}}^{\mathrm{RI}}(\mathbf{C}, \nu_{\mathrm{s}}) + \sum_{\alpha=1}^{N} \hat{\psi}_{\mathrm{R}}^{\mathrm{RD}(\alpha)}(\mathbf{C}, \mathbf{A}^{(\alpha)}). \tag{3.10}$$

It is worth noting that $\mathbf{C}$, ν_{s} and the stretch like internal variables $\mathbf{A}^{(\alpha)}$, are all invariant under a frame transformation since a change in frame does not affect referential vector or tensor fields, therefore, the constitutive equation (3.10) is frame invariant. While we do not show all the details regarding thermodynamics here, they are provided in Appendix A. Based on thermodynamic restrictions, the Cauchy stress is then given through

$$\mathbf{T} = 2J^{-1}\mathbf{F}\frac{\partial \hat{\psi}_{\mathrm{R}}}{\partial \mathbf{C}}\mathbf{F}^{\top} = \mathbf{T}^{\mathrm{RI}} + \sum_{\alpha} \mathbf{T}^{\mathrm{RD}(\alpha)}, \tag{3.11}$$

where

$$\mathbf{T}^{\mathrm{RI}} = 2J^{-1}\mathbf{F}\frac{\partial \hat{\psi}_{\mathrm{R}}^{\mathrm{RI}}}{\partial \mathbf{C}}\mathbf{F}^{\top}, \quad \text{and} \quad \mathbf{T}^{\mathrm{RD}(\alpha)} = 2J^{-1}\mathbf{F}\frac{\partial \hat{\psi}_{\mathrm{R}}^{\mathrm{RD}(\alpha)}}{\partial \mathbf{C}}\mathbf{F}^{\top}, \tag{3.12}$$

are the rate-independent and rate-dependent contributions to the Cauchy stress, respectively.

Rate-independent Contribution to the Free Energy Following [71], we assume that a typical filled rubber-like material may be treated as composite material with rigid filler particles in a soft matrix. Following their work, the rate-independent free energy has the form

$$\hat{\psi}_{\mathrm{R}}^{\mathrm{RI}} = \nu_{\mathrm{s}} G_{\mathrm{eq}} \lambda_{\mathrm{L}}^2 \left[\left(\frac{\Lambda}{\lambda_{\mathrm{L}}} \right) \beta + \ln \left(\frac{\beta}{\sinh \beta} \right) - \left(\frac{1}{\lambda_{\mathrm{L}}} \right) \beta_0 - \ln \left(\frac{\beta_0}{\sinh \beta_0} \right) \right] + \frac{1}{2} K (J-1)^2, \tag{3.13}$$

where the ν_{s} is the volume fraction of the soft domain, G_{eq} and K are the equilibrium, ground-state shear and bulk moduli, respectively. The parameter λ_{L} represents the locking stretch associated with limited chain extensibility of the long chain polymer molecules. And Λ, is the amplified stretch previously given in (4.4), with the

amplification factor [29]

$$X = 1 + 3.5(1 - \nu_{\mathrm{s}}) + 18(1 - \nu_{\mathrm{s}})^2. \tag{3.14}$$

Also, in (4.37) the functions β and β_0 are given by

$$\beta = \mathcal{L}^{-1}\left(\frac{\Lambda}{\lambda_{\mathrm{L}}}\right) \quad \text{and} \quad \beta_0 = \mathcal{L}^{-1}\left(\frac{1}{\lambda_{\mathrm{L}}}\right), \tag{3.15}$$

where $\mathcal{L}^{-1}$ is the inverse of the Langevin function, $\mathcal{L}(\bullet) = \coth(\bullet) - 1/(\bullet)$. Finally, using (4.37) in (3.12), the rate-independent contribution to the Cauchy stress is

$$\mathbf{T}^{\mathrm{RI}} = 2J^{-1}\mathbf{F}\frac{\partial \hat{\psi}_{\mathrm{R}}^{\mathrm{RI}}}{\partial \mathbf{C}}\mathbf{F}^{\top} = J^{-1}\nu_{\mathrm{s}} X G_{\mathrm{eq}}\left(\frac{\lambda_{\mathrm{L}}}{\Lambda}\right)\mathcal{L}^{-1}\left(\frac{\Lambda}{\lambda_{\mathrm{L}}}\right)(\mathbf{B}_{\mathrm{dis}})_0 + K(J-1)\mathbf{1}. \tag{3.16}$$

Rate-dependent Contribution to the Free Energy In order to model the rate-dependent contribution, we employ the work of [48], which has recently been successful as a validated model for unfilled visco-elastomers [48, 38, 97]. Following that work, the free energy for each mechanism α takes the form

$$\hat{\psi}_{\mathrm{R}}^{\mathrm{RD}(\alpha)} = \frac{1}{2}G_{\mathrm{neq}}^{(\alpha)}\left[\left(\mathbf{A}^{(\alpha)} : \mathbf{C}_{\mathrm{dis}} - 3\right) - \ln\left(\det \mathbf{A}^{(\alpha)}\right)\right], \tag{3.17}$$

where $G_{\mathrm{neq}}^{(\alpha)}$ are the non-equilibrium shear moduli. Note that (3.17), does not contain any volumetric contribution since that is already accounted for in (4.37).

As mentioned earlier in Section 3.2, we conducted a set of experiments with the intention of obtaining the viscous contribution to the overall response independently from the Mullins effect through preconditioning. As discussed in Section 3.2.4, and shown in Figure 3.5, the viscous stiffness exhibits strain stiffening as well as asymmetry between loading and unloading. Therefore, in a departure from the literature on filled rubbers, we have implemented the following new functional form for the non-equilibrium moduli to account for these two phenomena

$$G_{\mathrm{neq}}^{(\alpha)} = \varphi G_0^{(\alpha)}. \tag{3.18}$$

In (3.18), $G_0^{(\alpha)}$ is a ground state non-equilibrium shear modulus for each α. We have also introduced φ as a scalar parameter that stiffens with total deformation and also controls the asymmetric inelastic response between loading and unloading, the evolution will be discussed in Section 3.4.2. Straightforward calculations give the rate-dependent contribution to the Cauchy stress for each mechanism α as

$$\mathbf{T}^{\mathrm{RD}(\alpha)} = 2J^{-1}\mathbf{F}\frac{\partial \hat{\psi}_{\mathrm{R}}^{\mathrm{RD}(\alpha)}}{\partial \mathbf{C}}\mathbf{F}^{\top} = J^{-1}G_{\mathrm{neq}}^{(\alpha)}\left[\mathbf{F}_{\mathrm{dis}}\mathbf{A}^{(\alpha)}\mathbf{F}_{\mathrm{dis}}^{\top} - \frac{1}{3}(\mathbf{A}^{(\alpha)} : \mathbf{C}_{\mathrm{dis}})\mathbf{1}\right]. \tag{3.19}$$

3.4.2 Evolution Equations

Evolution of the Soft Domain Volume Fraction ν_{s} For the purpose of capturing the stretch-induced softening behavior, the idea of an evolution from hard to soft domains within the material was presented in [71]. Their approach states that the evolution of ν_{s} is triggered only when the local stretch exceeds the previous maximum stretch, i.e. $\Lambda \geq \Lambda^{\max}$. Here, $\Lambda^{\max}$ is an internal variable that takes on the maximum value of Λ in the prior history of each material point. With that in mind and following [58],[4] the evolution equation of ν_{s} is taken as

$$\dot{\nu_{\mathrm{s}}} = A(\nu_{\mathrm{ss}} - \nu_{\mathrm{s}})\frac{\lambda_L - 1}{(\lambda_L - \Lambda^{\max})^2}\dot{\Lambda}^{\max}, \quad \nu_{\mathrm{s}}(\mathbf{x}_{\mathrm{R}}, t = 0) = \nu_{\mathrm{s0}} \tag{3.20}$$

with

$$\dot{\Lambda}^{\max} = \begin{cases} 0, & \Lambda < \Lambda^{\max}, \\ \\ \dot{\Lambda}, & \Lambda = \Lambda^{\max}. \end{cases} \tag{3.21}$$

The form given in (4.42) is such that ν_{s} approaches the steady state value of ν_{ss} whenever $\dot{\Lambda} \neq 0$. As mentioned by [71], ν_{s} approaches its saturation value ν_{ss} more rapidly than $\Lambda^{\max}$ approaches λ_L, therefore, $\dot{\nu_{\mathrm{s}}}$ will always become dormant prior to chain locking and the associated numerical issues.

[4] This type of evolution equation was presented in [58] in a continuum damage mechanics context.

Evolution of the Viscous Internal Variables Following [48], the evolution of the internal variables $\mathbf{A}^{(\alpha)}$ is taken in the simple form

$$\dot{\mathbf{A}}^{(\alpha)} = \frac{1}{\tau^{(\alpha)}} \left(\mathbf{C}_{\text{dis}}^{-1} - \mathbf{A}^{(\alpha)} \right), \quad \mathbf{A}(\mathbf{x}_{\text{R}}, t = 0) = \mathbf{1}, \tag{3.22}$$

where $\tau^{(\alpha)}$ is the relaxation time for each mechanism α. This specific constitutive form is a linear evolution equation and shows that each internal variable $\mathbf{A}^{(\alpha)}$ approaches the current $\mathbf{C}_{\text{dis}}^{-1}$ with a relaxation time of $\tau^{(\alpha)}$. Therefore as time goes on, each $\mathbf{A}^{(\alpha)}$ reaches $\mathbf{C}_{\text{dis}}^{-1}$, at which point from (3.19) that α contribution to the non-equilibrium stress vanishes.

Evolution of Asymmetric Inelasticity Parameter φ In order to capture the measured viscous stretch stiffening and the asymmetric inelastic response between unloading and unloading, a dimensionless scalar parameter φ was previously introduced in (3.18). Adapting the recent work of [53], φ evolves with the amplified stretch rate $\dot{\Lambda}$, and the evolution is given by

$$\dot{\varphi} = B \left| \varphi_* - \varphi \right|^n \dot{\Lambda}, \tag{3.23}$$

where $B \geq 0$ is a material parameter that controls the rate, and

$$\varphi_* = \begin{cases} \left(1 - \dfrac{\Lambda}{D} \right)^{-1} & \text{when loading} \quad (\text{i.e., } \dot{\Lambda} > 0) \\ 0 & \text{when unloading} \quad (\text{i.e., } \dot{\Lambda} < 0) \end{cases} \tag{3.24}$$

controls the value. The parameter $D > 1$ controls the stretch dependent stiffening, and the parameter n controls the shape of the evolution curve. To further examine (3.23), we consider the loading and unloading cases separately:

- When loading, and $\dot{\Lambda} > 0$, in (3.23), φ approaches saturation value φ_*. Inspired by [24], φ_* takes a functional form which stiffens with the deformation.

- When unloading, and $\dot{\Lambda} < 0$, in (3.23), φ approaches the saturation value of 0.

Therefore, through (3.18), φ makes the effective viscous shear moduli stiffen with the deformation during loading, while making them vanish during unloading. This is directly inline with the measurements discussed in Section 3.2.4 and shown in Figure 3.5.

3.5 Model Calibration

A one-dimensional uniaxial stress version of the constitutive model was implemented in MATLAB so that we can exploit the nonlinear least squares algorithms readily available for calibration. In the procedure that follows, first the parameters related to the rate-independent response are calibrated using quasi-static uniaxial tension test data. That is followed by calibration of the viscous parameters on uniaxial tension test data, keeping the previously determined parameters fixed.

First, considering the contribution consisting of the rate-independent response, we choose a quasi-static load/unload/reload test at stretch rate of $\dot{\lambda} = 10^{-4}$/s to eliminate viscous effects. The experimentally measured stress - stretch curve from the experiment is shown in Figure 3.9a as black open circles. Using the stretch measured by the DIC as input to the constitutive model, a nonlinear least squares fit was performed on the error of $\mathbf{T}^{\mathrm{RI}}$ in (4.41), in uniaxial tension. The solid line in Figure 3.9a is the calibrated model with the material parameters G_{eq}, λ_{L}, A, ν_{s0} and ν_{ss} provided in Table 3.1. To approximate nearly-incompressible behavior, the bulk modulus K is set to be three orders of magnitude larger than G_{eq}.

Next, we bring our attention to calibration of the α rate-dependent mechanisms. In order to determine the rate-dependent parameters $G_0^{(\alpha)}$, $\tau^{(\alpha)}$, D, B and n, the previously calibrated rate-independent parameters are kept fixed. Using the stretch history measured from the experiments as input to the constitutive model, the calibration is then performed through a least squares comparison of the total

Table 3.1 Calibrated Material Parameters for Viton

Rate-independent		Rate-dependent	
Parameter	Value	Parameter	Value
G_{eq}	384.5 kPa	$G_0^{(1)}$	413.4 kPa
$K\,(=10^3 G_{\text{eq}})$	384.4 MPa	$G_0^{(2)}$	189.6 kPa
λ_{L}	1.54	$\tau^{(1)}$	2.28 s
A	0.85	$\tau^{(2)}$	602.75 s
ν_{s0}	0.57	D	2.86
ν_{ss}	0.89	B	26.15
		n	1.9

stress $\mathbf{T}$ from (3.11) (with $\mathbf{T}^{\text{RI}}$ already calibrated) against load/unload/reload tensile test experiments at multiple stretch rates as well as a multi-step stress relaxation experiment concurrently.

To determine the number of active rate-dependent mechanisms α, the non-equilibrium calibration procedure is performed for increasing α and the final results compared. We chose the minimum number of α that provides reasonable convergence in the error. In this specific case, we have found that $\alpha = 2$ gives good comparisons while keeping the number of material parameters low. The calibrated model is shown in Figures 3.9a-d, where open circles are experimentally measured data, and lines are the calibrated model. Values of all material parameters calibrated for Viton are found in Table 3.1.

3.6 Validation Experiment and Simulation

For the purpose of validating the constitutive model, we performed an inhomogeneous tension experiment and compare some key measurable quantities with a numerical simulation using the previously calibrated material parameters shown in Table 3.1.

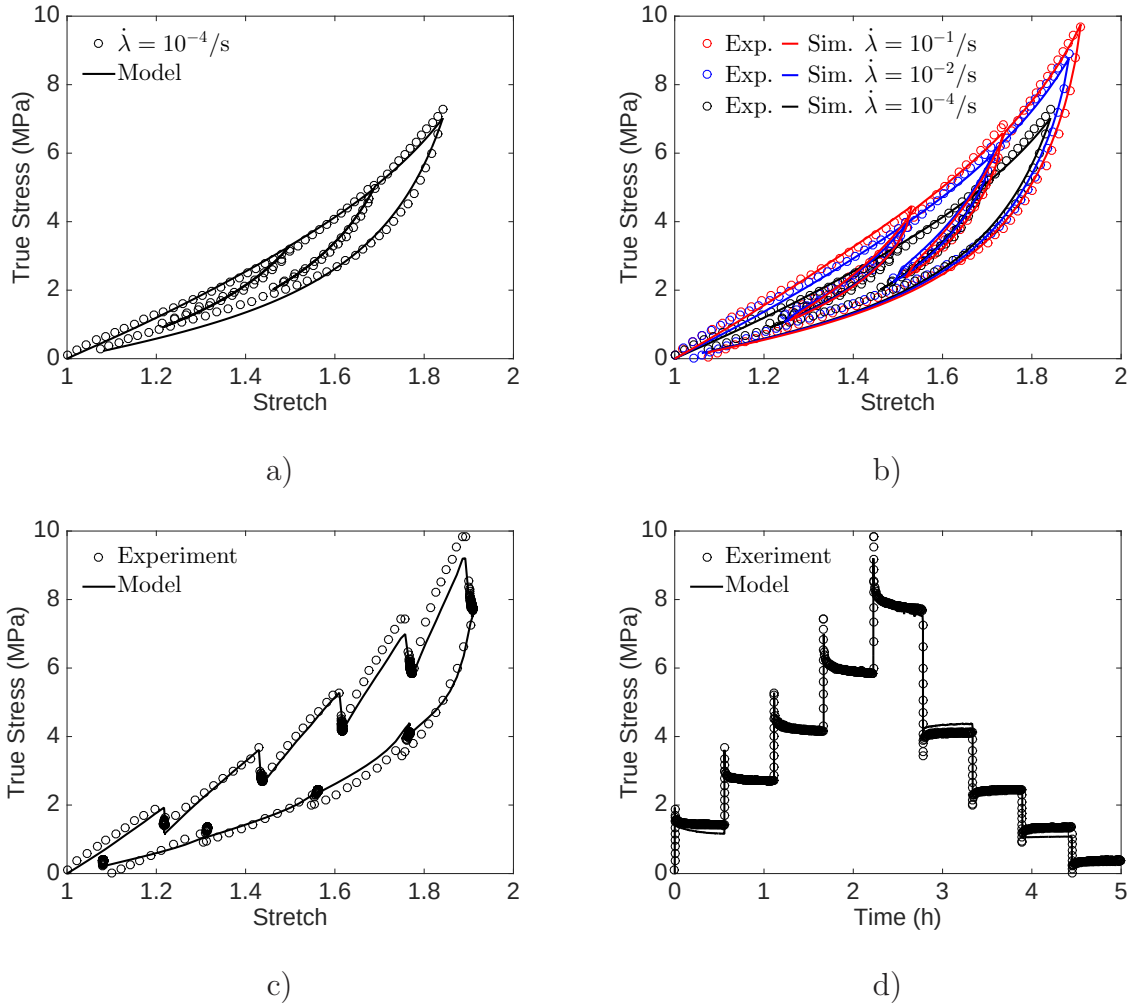

Figure 3.9 Model calibration results using virgin specimens, experiments are shown as open circles and the calibrated model as solid lines. a) Quasi-static load/unload/reload test, b) load/unload/reload uniaxial tension tests at different stretch rates, and multi-step relaxation c) stress - stretch and d) stress - time.

For the experiment, the specimen is prepared by using an ASTM D638-I cutting die to obtain a virgin specimen from a sheet of raw Viton material. Three circular holes, each with a radius of 3.16 mm, were punched out from the gauge section to create a purposefully un-symmetric geometry. The detail of geometry is shown in Figure 3.10a, and we note that the gripping area is not shown. Prior to the experiment, one entire face of the specimen was spray-painted with a random speckle pattern of white paint so that full field DIC measurements may be obtained to compute the measured strain field. We again used the tensile testing machine for the validation, the displacement was measured using DIC and the force with the 1 kN load cell.

Additionally, the constitutive model was implemented in [1] by writing a user material subroutine UMAT. The mesh of the geometry shown in Figure 3.10b was discretized with 1650 C3D8H elements and 2516 nodes. The boundary conditions are shown in Figure 3.10b, face EFGH is pinned and the displacement u measured from the experiment is prescribed on face ABCD in the 2 direction and constrained in the other directions. The force is obtained by summing up the reaction force from each node in the 2 direction on face EFGH. All remaining faces are considered traction free.

The results are shown in Figure 3.11, the measured displacement as a function of time is shown in Figure 3.11a, and the comparison of force - displacement curves as well as time - force curves between the experiment and numerical simulation are shown in Figures 3.11b and 3.11c — the simulation and experiment show good agreement. Furthermore, Figure 3.12 shows a quantitative comparison between the measured and simulated Hencky strain field E_{22} at various times in the deformation, where the Hencky strain is given by $\mathbf{E} = \ln \mathbf{U}$. Again, the comparison shows a good quantitative agreement. Lastly, while we cannot validate the evolution of ν_s, Figure 3.13 shows that for this deformation, an inhomogeneous field of ν_s is present. From the observation

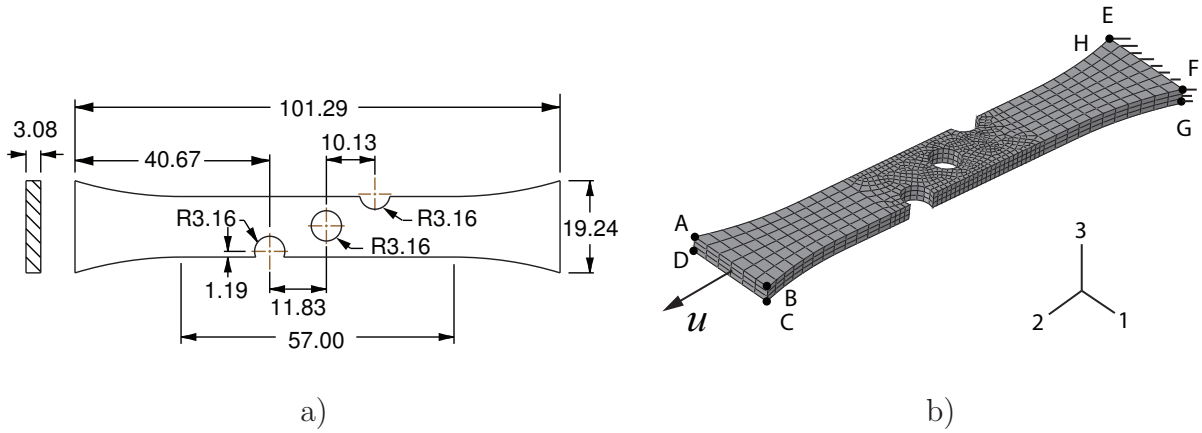

a) b)

Figure 3.10 Viton specimen used for the validation experiment. a) Measured dimensions in mm, and b) undeformed initial finite element mesh with boundary conditions, the displacement u measured from the experiment is prescribed on face ABCD.

made from above, our proposed model quantitatively captures the response of Viton very well.

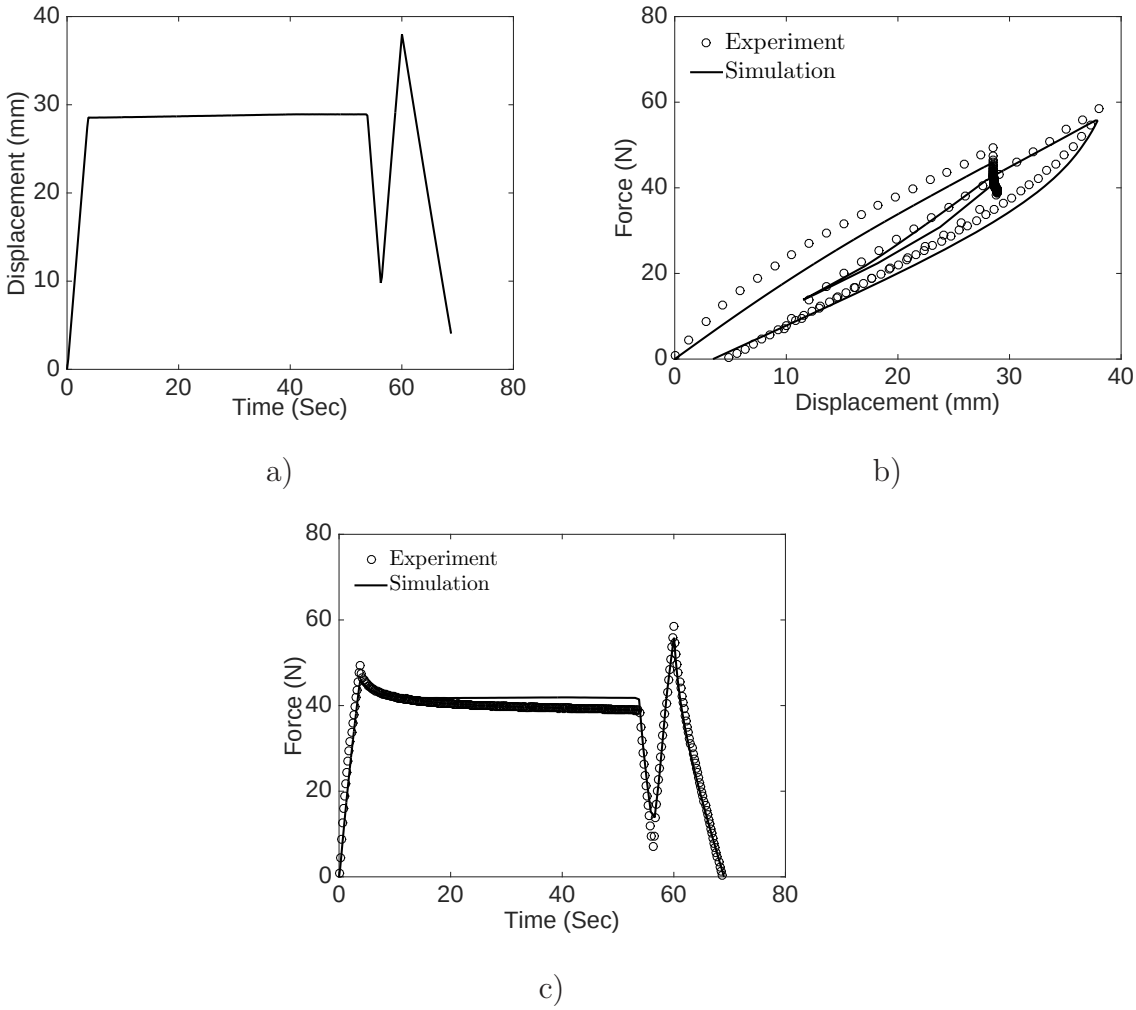

Figure 3.11 Validation experiment and simulation results, a) the measured displacement as a function of time (only showing when the specimen is under tensile load), b) the comparison of the force - displacement curve and c) the comparison of force - time curve between experiment and simulation.

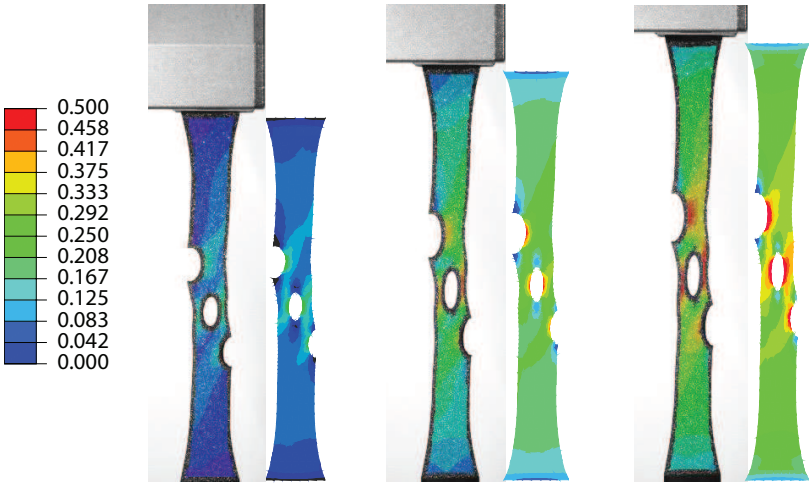

Figure 3.12 Comparison of E_{22}, where $\mathbf{E} = \ln \mathbf{U}$, between the experimentally measured and simulated validation. The left half of each subfigure shows the measured E_{22} from DIC, while the right half of each subfigure shows the numerically computed E_{22}. The results are shown at displacements of a) 15.14 mm, b) 28.90 mm, and c) 37.98 mm.

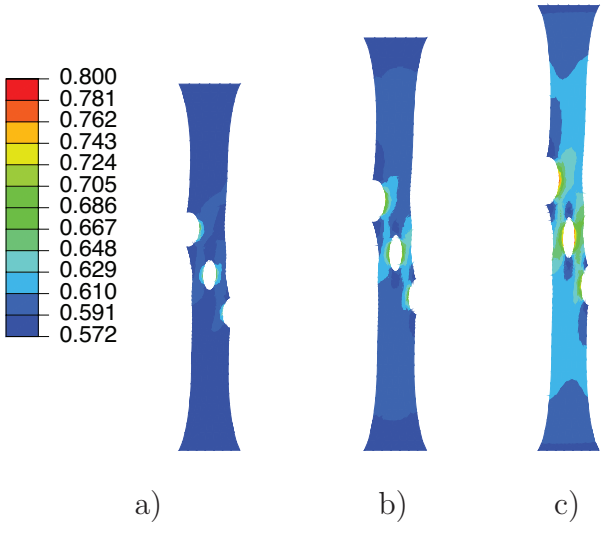

Figure 3.13 Numerically computed ν_s field shown at a displacement of a) 15.14 mm, b) 28.90 mm and c) 37.98 mm.

CHAPTER 4

MODELING THERMAL RECOVERY OF THE MULLINS EFFECT

4.1 Introduction

Research on the broad topic of elastomeric materials has been ongoing for over a half-century with constant improvements and developments. Various applications may be found in cutting-edge technologies as well as industrial consumer products ranging from smart soft robots, artificial heart valves, tires, shock absorbers, to O-ring seals [14, 84, 11, 69, 80, 88, 97]. A thorough understanding of the mechanical behavior of elastomeric materials is essential when it comes to design for applications. For the purpose of strengthening the material and improving its durability, different fillers are added as reinforcement [76]. However, the interactions between the fillers and polymer network gives these materials a very interesting inelastic behavior, which includes the Mullins effect as well as rate-dependency.

Among these inelastic behaviors, one that is intellectually stimulating is the Mullins effect. The Mullins effect, which is easily observed by stretching a virgin filled rubber material in cyclic loading, exhibits a behavior where the stress response becomes noticeably softer during the unloading and reloading, and only becomes stiffer again after experiencing a stretch greater than any in its prior history. Further, the Mullins effect is observed under many different deformation modes [4, 53]. The underlying physics responsible for the Mullins effect is still not fully agreed upon, and accordingly numerous models exist in the literature. Early phenomenological models [61, 62, 31, 32] assume an amorphous micro-structure consisting of hard and soft phases for the filler and rubber matrix, respectively. Upon stretching, the virgin material with an initial volume fraction of hard phase undergoes an irreversible deformation induced phase change to the soft phase. Further phase change only occurs

when the stretch is greater than any previously attained. Recent models [5, 6, 71, 96] based on this classic idea have found success capturing the Mullins effect in numerous filled elastomers. Additionally, taking a different modeling approach, models based on the concept of continuum damage mechanics are in wide use [83, 56, 63, 18, 19]. In those approaches, a scalar damage parameter is introduced which evolves with deformation. Also, micro-mechanics models based on the statistical mechanics of chain rupture or filler cluster rupture also found success in modeling the Mullins effect [25, 44, 54].

There is ample experimental evidence that shows the Mullins effect may be recovered, at least partially, at room temperature. Seminal research on such recovery was reported by [59]. He discovered that roughly 20% of the strength was recovered for a filled elastomer at room temperature after four days. Later, [76] showed that a carbon black filled rubber partially recovered after four weeks of relaxation at room temperature. [30] shows that the stress softening effect induced by the first loading could be partially recovered within six months for silica-filled PDMS at room temperature. And [99] shows that complete recovery of Mullins effect at room temperature was found in a nanoparticle-filled polymer composite after 17 hours.

Further, at elevated temperatures, the completeness and rate of recovery are higher, and in some cases fully recovered. For example, [59] reports that a carbon black filled rubber recovered to 80% of its virgin state after annealing for two days at 100°C under vacuum. In corroboration, [47], also shows that carbon black filled natural rubber almost fully recovered to its virgin state after annealing at 95°C under vacuum for two days. [33] did similar tests on eight different variants of filled rubber materials at an annealing temperature of 100°C under vacuum, with the results mostly indicating recovery of the materials toward their virgin state. More recently, [17] reports that carbon black filled SBR partially, and fully recovered, the Mullins effect when subjected to annealing for 13 and 17 hours at 80°C, respectively.

However, even with such a large number of experiments in the literature, the majority of the existing *modeling* literature assumes that the Mullins effect is an irreversible process. When it comes to models that capture thermal recovery, very little is found except for the work of [22]. Which is based on the idea of permanent and temporary networks to capture both Mullins effect as well as its recovery caused by thermal annealing and solvent exposure. Their model was calibrated to the experiments of [33] using only five parameters. The calibrations, however, were done on each process (first loading, second loading, third loading after annealing) separately, and not on the complete process as a whole.

In this paper, our objective is to develop a thermodynamically consistent thermo-mechanically coupled constitutive model that *quantitatively* captures the thermal recovery of the Mullins effect. We model the Mullins effect by exploiting the idea of the hard/soft phase transition. The thermal recovery is modeled through a new temperature dependent *reversible* evolution equation for the hard/soft phase volume fraction. We use experimental data from the literature [59, 33] for guidance in the specific constitutive forms, and use the results of [33] for model calibration. We have also implemented our thermo-mechanically coupled constitutive model by writing a user material subroutine for the finite element program [1].

The remainder of this chapter is organized as follows, Section 4.2 describes the behavior through experiments found in the literature. Section 4.3 overviews the thermo-mechanically coupled continuum level framework used, with Sections 4.4 and 4.5 discussing constitutive equations. Section 4.6 summarizes the two coupled governing equations. In Section 4.7 the model is calibrated to a suite of experiments at various temperatures performed by [33], and the general behavior shown in Section 4.8. And lastly we finish with concluding remarks in chapter 5.

4.2 Experimental Observations

As mentioned earlier, many early studies on the behavior of elastomeric materials [59, 60, 33] found evidence that both natural rubber, and filled rubber, after a pre-stretch regained some portion of their strength after leaving the specimen to anneal at various temperatures for several days. [33] conducted a series of tensile tests on specimens using three vulcanizing systems — named, Type A, B, and C — at a stretch rate of $2\,\mathrm{min}^{-1}$. In their experiments, each virgin specimen undergoes two load/unload cycles (referred to as a "first" and "second" stretching) at room temperature, followed by stress free annealing in an oven heated to 100°C for 24 hours under vacuum. Then, a third stretching was performed at room temperature to assess the thermal recovery. Figure 4.1 shows the loading portion of stretch - stress curves for eight variants (using different amounts of crosslinker) of material types A, B, and C. The first stretching on the virgin specimen is denoted by filled red circles, the second stretching is denoted with filled black squares, and the third stretching after recovery is denoted with filled blue triangles. Different amounts of recovery are clearly found in Figure 4.1. In comparison, Type A materials in Figure 4.1a recovered slightly, and a high degree of recovery is found in Type B materials which are shown in Figure 4.1b, finally in Figure 4.1c, Type C materials are nearly fully recovered. In a different set of experiments, [59] captured the recovery process as a function of time, and at three different elevated annealing temperatures, 20°C, 60°C, and 100°C, with the results shown in Figure 4.2. It is obvious from Figure 4.2, that both the recovery rate, and the amount of recovery depend on the temperature. However, since many details on the material were not included in the original paper, we are unable to use the data in Figure 4.2 for model calibration. Nonetheless, this observation is useful for guidance of specific constitutive forms.

4.3 Continuum Framework

In this section we cover the kinematics and balance laws from a continuum perspective to describe the thermo-mechanically coupled behavior of filled rubber-like materials focusing on the Mullins effect and its thermal recovery as described in Section 4.2.

4.3.1 Kinematics

Consider a body $\mathcal{B}_{\mathrm{R}}$ identified with the region of space it occupies in a fixed reference configuration, and denote by $\mathbf{x}_{\mathrm{R}}$ an arbitrary material point of $\mathcal{B}_{\mathrm{R}}$. The referential body $\mathcal{B}_{\mathrm{R}}$ then undergoes a motion $\mathbf{x} = \boldsymbol{\chi}(\mathbf{x}_{\mathrm{R}}, t)$ to the deformed body $\mathcal{B}_t$ with deformation gradient given by[1]

$$\mathbf{F} = \nabla\boldsymbol{\chi}, \quad \text{such that} \quad J = \det\mathbf{F} > 0. \tag{4.1}$$

The right and left Cauchy-Green deformation tensors are given by $\mathbf{C} = \mathbf{F}^{\top}\mathbf{F}$ and $\mathbf{B} = \mathbf{F}\mathbf{F}^{\top}$, respectively. The deformation gradient admits the polar decomposition, $\mathbf{F} = \mathbf{R}\mathbf{U}$, where $\mathbf{R}$ is a rotation and $\mathbf{U}$ the stretch, with $\mathbf{U} = \sqrt{\mathbf{C}}$. We assume that the material is *nearly*-incompressible, and introduce the distortional part of the deformation gradient, defined as

$$\mathbf{F}_{\mathrm{dis}} = J^{-1/3}\mathbf{F} \quad \text{so that} \quad \det\mathbf{F}_{\mathrm{dis}} = 1. \tag{4.2}$$

The distortional right and left Cauchy-Green deformation tensors are then $\mathbf{C}_{\mathrm{dis}} = \mathbf{F}_{\mathrm{dis}}^{\top}\mathbf{F}_{\mathrm{dis}} = J^{-2/3}\mathbf{C}$ and $\mathbf{B}_{\mathrm{dis}} = \mathbf{F}_{\mathrm{dis}}\mathbf{F}_{\mathrm{dis}}^{\top} = J^{-2/3}\mathbf{B}$. As is standard, the effective stretch is given by

$$\bar{\lambda} = \sqrt{\operatorname{tr}\mathbf{C}_{\mathrm{dis}}/3}\,. \tag{4.3}$$

[1]The symbols ∇ and Div denote the gradient and divergence with respect to the material point $\mathbf{x}_{\mathrm{R}}$ in the reference configuration; while grad and div denote these operators with respect to the point $\mathbf{x} = \boldsymbol{\chi}(\mathbf{x}_{\mathrm{R}}, t)$ in the deformed configuration.

4.3.2 Stress Softening Variables

We treat filled rubber-like materials as a composite system of a "hard" filler and a "soft" rubber matrix, where the filler volume fraction is denoted by ν_{f}, and the volume fraction of soft domain is $\nu_{\mathrm{s}} = 1 - \nu_{\mathrm{f}}$. One possible explanation for the Mullins effect is that deformation breaks up hard regions, so that the effective soft domain fraction increases. Such an evolution equation is constitutive and will be prescribed in the following sections.

Further, following [61], when this class of material undergoes an arbitrary deformation, the hard filler accommodates much less of the overall deformation than the soft rubber matrix. Therefore, an amplified stretch

$$\Lambda = \sqrt{X(\bar{\lambda}^2 - 1) + 1} \tag{4.4}$$

is used for the rubber matrix, where X is a amplification factor and it usually depends on the volume fraction ν_{s}, and the shape of the filler. In this work, we assume an amplification factor in the form [29]

$$X = 1 + 3.5(1 - \nu_{\mathrm{s}}) + 18(1 - \nu_{\mathrm{s}})^2 \,. \tag{4.5}$$

4.3.3 Balance Laws

Balance of Forces and Moments Neglecting inertia, the balance of forces and moments in the deformed body $\mathcal{B}_t$ are expressed as

$$\operatorname{div} \mathbf{T} + \mathbf{b} = \mathbf{0} \quad \text{and} \quad \mathbf{T} = \mathbf{T}^{\top}, \tag{4.6}$$

where $\mathbf{T}$ is the Cauchy stress and $\mathbf{b}$ the body force. Further, (4.6) serves as the governing equation for the displacement field. The boundary of the deformed body $\partial\mathcal{B}_t$ has outward unit normal $\mathbf{n}$, and the external surface traction on an element of the deformed surface is given by

$$\mathbf{t} = \mathbf{T}\mathbf{n}. \tag{4.7}$$

Balance of Energy and Entropy Imbalance Let ε and η denote the specific internal energy and specific entropy measured per unit mass in the spatial body, ρ the spatial mass density, $\mathbf{q}$ denotes the heat flux measured per unit area in the spatial configuration and q is the heat source/sink measured per unit volume in the spatial body. The balance of energy in the spatial body $\mathcal{B}_t$ is the requirement that for an arbitrary part $\mathcal{P}_t$ of the body

$$\overset{\cdot}{\int_{\mathcal{P}_t} \rho\varepsilon dv} = -\int_{\partial\mathcal{P}_t} \mathbf{q}\cdot\mathbf{n}da + \int_{\mathcal{P}_t} qdv + \int_{\partial\mathcal{P}_t} \mathbf{T}\mathbf{n}\cdot\mathbf{v}da + \int_{\mathcal{P}_t} \mathbf{b}\cdot\mathbf{v}dv. \tag{4.8}$$

Since the part $\mathcal{P}_t$ is arbitrary, the local form of (4.8) is obtained by using the divergence theorem,

$$\rho\dot{\varepsilon} = -\operatorname{div}\mathbf{q} + q + \mathbf{T}:\mathbf{L} \tag{4.9}$$

with velocity gradient $\mathbf{L} = \dot{\mathbf{F}}\mathbf{F}^{-1}$. The stress power, $\mathbf{T}:\mathbf{L}$, admits the decomposition

$$\begin{aligned} \mathbf{T}:\mathbf{L} &= \mathbf{T}:\left(\dot{\mathbf{F}}\mathbf{F}^{-1}\right) \\ &= \frac{1}{2}J^{-1}\mathbf{S}:\mathbf{C} \end{aligned} \tag{4.10}$$

where we introduced the stress measure

$$\mathbf{S} = J\mathbf{F}^{-1}\mathbf{T}\mathbf{F}^{-\top} \tag{4.11}$$

as second Piola stress. Thus, the balance of energy may be written in the form

$$\rho\dot{\varepsilon} = -\operatorname{div}\mathbf{q} + q + \frac{1}{2}J^{-1}\mathbf{S}:\mathbf{C}. \tag{4.12}$$

Next, for an arbitrary part $\mathcal{P}_t$ of the deformed body, the second law takes the form of an entropy imbalance

$$\overset{\cdot}{\int_{\mathcal{P}_t} \rho\eta dv} \geq -\int_{\partial\mathcal{P}_t} \frac{\mathbf{q}\cdot\mathbf{n}}{\vartheta}da + \int_{\mathcal{P}_t} \frac{q}{\vartheta}dv, \tag{4.13}$$

where ϑ denotes the absolute temperature. Since the part $\mathcal{P}_t$ is arbitrary, we obtain the local form of (4.13) as

$$\rho\dot{\eta} \geq -\frac{1}{\vartheta}\operatorname{div}\mathbf{q} + \frac{1}{\vartheta^2}\mathbf{q}\cdot\operatorname{grad}\vartheta + \frac{q}{\vartheta}. \tag{4.14}$$

Let

$$\psi \stackrel{\text{def}}{=} \varepsilon - \vartheta\eta \tag{4.15}$$

denote the Helmholtz free energy measured per unit deformed mass. Then (4.12) and (4.14), with (4.15), yield the local dissipation inequality

$$\rho\dot{\psi} + \rho\eta\dot{\vartheta} + \frac{1}{\vartheta}\mathbf{q}\cdot\operatorname{grad}\vartheta - \frac{1}{2}J^{-1}\mathbf{S}:\dot{\mathbf{C}} \leq 0\,. \tag{4.16}$$

The referential quantities ψ_{R}, ε_{R}, and η_{R} are related to their true counterparts through following relations

$$\psi_{\mathrm{R}} = \rho J\psi, \quad \text{and} \quad \varepsilon_{\mathrm{R}} = \rho J\varepsilon, \quad \text{and} \quad \eta_{\mathrm{R}} = \rho J\eta\,, \tag{4.17}$$

which allow us to rewrite (4.16) as

$$\dot{\psi}_{\mathrm{R}} + \eta_{\mathrm{R}}\dot{\vartheta} + \frac{J}{\vartheta}\mathbf{q}\cdot\operatorname{grad}\vartheta - \frac{1}{2}\mathbf{S}:\dot{\mathbf{C}} \leq 0\,. \tag{4.18}$$

4.4 Constitutive Theory

4.4.1 Basic Constitutive Equations

Taking the guidance from experiments in the literature as shown in Section 4.2, we assume that the thermo-mechanically coupled mechanical response of filled rubber-like materials is mainly hyperelastic, along with softening due to the Mullins effect, any other inelastic effects are neglected since they are not the focus of this work. Based on the local dissipation inequality (4.18), we assume the following set of constitutive

equations

$$\begin{aligned} \psi_{\mathrm{R}} &= \hat{\psi}_{\mathrm{R}}(\mathbf{C}, \nu_{\mathrm{s}}, \vartheta) \\ \eta_{\mathrm{R}} &= \hat{\eta}_{\mathrm{R}}(\mathbf{C}, \nu_{s}, \vartheta) \\ \mathbf{S} &= \hat{\mathbf{S}}(\mathbf{C}, \nu_{s}, \vartheta) \end{aligned} \tag{4.19}$$

along with an evolution equation for the volume fraction of soft domain

$$\dot{\nu}_{\mathrm{s}} = \dot{\nu}_{\mathrm{s}}(\mathbf{C}, \nu_{\mathrm{s}}, \vartheta). \tag{4.20}$$

The heat flux is taken to follow Fourier's law

$$\mathbf{q} = -\kappa(\vartheta)\mathrm{grad}\,\vartheta, \tag{4.21}$$

where κ is the (scalar) temperature dependent thermal conductivity.

Thermodynamic Restrictions Taking the time derivative of the free-energy in (4.19), we have

$$\dot{\hat{\psi}}_{\mathrm{R}}(\mathbf{C}, \nu_{\mathrm{s}}, \vartheta) = \frac{\partial \hat{\psi}_{\mathrm{R}}}{\partial \mathbf{C}} : \dot{\mathbf{C}} + \frac{\partial \hat{\psi}_{\mathrm{R}}}{\partial \nu_{\mathrm{s}}}\dot{\nu}_{\mathrm{s}} + \frac{\partial \hat{\psi}_{\mathrm{R}}}{\partial \vartheta}\dot{\vartheta}, \tag{4.22}$$

then use of (4.21), (4.22) in (4.18) yields

$$\left(\frac{\hat{\psi}_{\mathrm{R}}}{\partial \mathbf{C}} - \frac{1}{2}\mathbf{S}\right) : \dot{\mathbf{C}} + \frac{\partial \hat{\psi}_{\mathrm{R}}}{\partial \nu_{\mathrm{s}}}\dot{\nu}_{\mathrm{s}} + \left(\frac{\partial \hat{\psi}_{\mathrm{R}}}{\partial \vartheta} + \eta_{\mathrm{R}}\right)\dot{\vartheta} - \frac{J}{\vartheta}(\kappa \mathrm{grad}\,\vartheta) \cdot \mathrm{grad}\,\vartheta \leq 0. \tag{4.23}$$

Further, sufficient conditions for the constitutive equations to satisfy (4.18) provide the state relations,

$$\left.\begin{aligned} \mathbf{S} &= 2\frac{\partial \hat{\psi}_{\mathrm{R}}(\mathbf{C}, \nu_{\mathrm{s}}, \vartheta)}{\partial \mathbf{C}} \\ \eta_{\mathrm{R}} &= -\frac{\partial \hat{\psi}_{\mathrm{R}}(\mathbf{C}, \nu_{\mathrm{s}}, \vartheta)}{\partial \vartheta} \end{aligned}\right\} \tag{4.24}$$

and the reduced dissipation inequality becomes

$$-\frac{\partial \psi_{\mathrm{R}}}{\partial \nu_{\mathrm{s}}}\dot{\nu}_{\mathrm{s}} + \frac{J}{\vartheta}(\kappa \mathrm{grad}\,\vartheta) \cdot \mathrm{grad}\,\vartheta \geq 0. \tag{4.25}$$

Next, we define the thermodynamic driving force conjugate to the time rate of the volume fraction of the soft domain as

$$F \stackrel{\text{def}}{=} -\frac{\partial \psi_{\text{R}}}{\partial \nu_{\text{s}}}\,, \tag{4.26}$$

and we will assume that the response is strictly dissipative so that

$$(\kappa \text{grad}\,\vartheta) \cdot \text{grad}\,\vartheta > 0 \quad \text{when} \quad \text{grad}\,\vartheta \neq \mathbf{0}, \tag{4.27}$$

and

$$F\dot{\nu}_{\text{s}} > 0 \quad \text{when} \quad \dot{\nu}_{\text{s}} \neq 0. \tag{4.28}$$

Further Consequences of Thermodynamics Using (4.24) and (4.26) in (4.22) gives the first Gibbs relation

$$\dot{\psi}_{\text{R}} = \frac{1}{2}\mathbf{S} : \dot{\mathbf{C}} - F\dot{\nu}_{\text{s}} - \eta_{\text{R}}\dot{\vartheta}. \tag{4.29}$$

The second Gibbs relation with $\psi_{\text{R}} = \varepsilon_{\text{R}} - \vartheta\eta_{\text{R}}$ is given by

$$\dot{\varepsilon}_{\text{R}} = \frac{1}{2}\mathbf{S} : \dot{\mathbf{C}} - F\dot{\nu}_{\text{s}} + \vartheta\dot{\eta}_{\text{R}} \tag{4.30}$$

Next, we define the specific heat measured in energy per unit mass mass per temperature

$$C \stackrel{\text{def}}{=} \frac{\partial \varepsilon}{\partial \vartheta} = \frac{1}{\rho J}\frac{\partial \varepsilon_{\text{R}}}{\vartheta} \tag{4.31}$$

for a fixed deformation. Using the (4.24) with (4.15) we have

$$C = \frac{1}{\rho J}\left(\frac{\psi_{\text{R}}}{\vartheta} + \eta_{\text{R}} + \vartheta\frac{\partial \eta_{\text{R}}}{\vartheta}\right) = -\frac{\vartheta}{\rho J}\frac{\partial^2 \psi_{\text{R}}}{\partial \vartheta^2} \tag{4.32}$$

Next using (4.24), we obtain

$$\dot{\eta}_{\text{R}} = -\frac{1}{2}\frac{\partial \mathbf{S}}{\partial \vartheta} : \dot{\mathbf{C}} - \frac{\partial^2 \psi_{\text{R}}}{\partial \vartheta^2}\dot{\vartheta} + \frac{\partial F}{\partial \vartheta}\dot{\nu}_{\text{s}} \tag{4.33}$$

which provides

$$\vartheta\dot{\eta}_{\mathrm{R}} = -\frac{1}{2}\vartheta\frac{\partial \mathbf{S}}{\partial \vartheta} : \dot{\mathbf{C}} + \rho J C\dot{\vartheta} + \vartheta\frac{\partial F}{\partial \vartheta}\dot{\nu}_{\mathrm{s}}. \tag{4.34}$$

The use of (4.34) and (4.30) in (4.12) yields the heat equation in the deformed body

$$\rho C\dot{\vartheta} = \operatorname{div}(\kappa \operatorname{grad}\vartheta) + q + J^{-1}F\dot{\nu}_{\mathrm{s}} + \frac{1}{2}J^{-1}\vartheta\frac{\partial \mathbf{S}}{\partial \vartheta} : \dot{\mathbf{C}} - J^{-1}\vartheta\frac{\partial F}{\partial \vartheta}\dot{\nu}_{\mathrm{s}}\,. \tag{4.35}$$

4.5 Specialization of the Constitutive Equations

4.5.1 Free Energy

For *nearly*-incompressible materials, the total free energy can be decomposed into distortional and volumetric contributions [28], the separable form is given as

$$\tilde{\psi}_{\mathrm{R}} = \tilde{\psi}_{\mathrm{R}}^{\mathrm{dis}}(\mathbf{C}_{\mathrm{dis}}, \nu_{\mathrm{s}}, \vartheta) + \tilde{\psi}_{\mathrm{R}}^{\mathrm{vol}}(J, \vartheta). \tag{4.36}$$

Following [71], the material system may be modeled as composite material with rigid filler particles in a soft matrix. Following their work, the distortional contribution of the free energy in (4.36) has the form

$$\tilde{\psi}_{\mathrm{R}}^{\mathrm{dis}} = \nu_{\mathrm{s}} G_0 \lambda_{\mathrm{L}}^2 \left[\left(\frac{\Lambda}{\lambda_{\mathrm{L}}}\right)\beta + \ln\left(\frac{\beta}{\sinh\beta}\right) - \left(\frac{1}{\lambda_{\mathrm{L}}}\right)\beta_0 + \ln\left(\frac{\beta_0}{\sinh\beta_0}\right)\right], \tag{4.37}$$

where the ν_{s} is the volume fraction of the soft domain, G_0 is the temperature dependent ground-state shear modulus. The ground state shear modulus is temperature dependent and given by the standard relation

$$G_0 = N_{\mathrm{R}} R\vartheta \tag{4.38}$$

where N_{R} denotes the number of polymer chains per unit reference volume, and R is the universal gas constant. In (4.37), the parameter λ_{L} represents the locking stretch associated with limited chain extensibility of the long chain polymer molecules. And Λ, is the amplified chain stretch previously given in (4.4). Also, in (4.37) the functions

β and β_0 are given by

$$\beta = \mathcal{L}^{-1}\left(\frac{\Lambda}{\lambda_{\mathrm{L}}}\right) \quad \text{and} \quad \beta_0 = \mathcal{L}^{-1}\left(\frac{1}{\lambda_{\mathrm{L}}}\right), \tag{4.39}$$

where $\mathcal{L}^{-1}$ is the inverse of the Langevin function, $\mathcal{L}(\bullet) = \coth(\bullet) - 1/(\bullet)$. The volumetric contribution of the free energy is taken as

$$\tilde{\psi}_{\mathrm{R}}^{\mathrm{vol}} = \frac{1}{2}K(J-1)^2 \tag{4.40}$$

with K the bulk modulus. We note that in (4.40), we have ignored any contribution due to thermal expansion for the purpose of highlighting thermal recovery of the Mullins effect in the constitutive equations.

Finally, using (4.36), (4.37), and (4.40) in (4.24), the Cauchy stress is given by

$$\mathbf{T} = J^{-1}\mathbf{F}\left(2\frac{\partial\tilde{\psi}_{\mathrm{R}}}{\partial\mathbf{C}}\right)\mathbf{F}^{\top} = J^{-1}\nu_{\mathrm{s}}XG_0\left(\frac{\lambda_{\mathrm{L}}}{\Lambda}\right)\mathcal{L}^{-1}\left(\frac{\Lambda}{\lambda_{\mathrm{L}}}\right)(\mathbf{B}_{\mathrm{dis}})_0 + K(J-1)\mathbf{1}. \tag{4.41}$$

4.5.2 Evolution Equations

In order to model the Mullins effect and its thermal recovery, the evolution equation for the volume fraction of soft domain is taken in a form that includes the typical deformation induced softening, but also includes temperature dependent static recovery. Such an evolution may be written in the form

$$\dot{\nu_{\mathrm{s}}} = d + r \qquad \text{with} \qquad \nu_{\mathrm{s}}(\mathbf{x}_{\mathrm{R}}, t=0) = \nu_{\mathrm{s}0}, \tag{4.42}$$

where the d is the rate of deformation induced softening and r is the temperature dependent rate of static recovery.

Stretch Induced Softening For the purpose of capturing the stretch-induced softening behavior, the idea of an evolution from hard to soft domains within the material was presented in [71]. Their approach states that the evolution of ν_{s} is triggered only when the local stretch exceeds the previous maximum stretch, i.e.

$\Lambda = \Lambda^{\max}$. Where $\Lambda^{\max}$ is an internal variable that takes on the maximum value of Λ in the prior history of each material point. With that in mind, following [58],[2] the stretch-induced contribution to $\dot{\nu}_{\rm s}$ is taken as

$$d = A(\nu_{\rm ss} - \nu_{\rm s})\frac{\lambda_L - 1}{(\lambda_L - \Lambda^{\max})^2}\dot{\Lambda}^{\max} \tag{4.43}$$

with

$$\dot{\Lambda}^{\max} = \begin{cases} 0, & \Lambda < \Lambda^{\max}, \\ \\ \dot{\Lambda}, & \Lambda = \Lambda^{\max}. \end{cases} \tag{4.44}$$

The form given in (4.43) is such that $\nu_{\rm s}$ approaches the steady state value of $\nu_{\rm ss}$ whenever $\dot{\Lambda} \neq 0$. As mentioned by [71], $\nu_{\rm s}$ approaches its saturation value $\nu_{\rm ss}$ more rapidly than $\Lambda^{\max}$ approaches λ_L, therefore, $\dot{\nu}_{\rm s}$ will always become dormant prior to chain locking and the associated numerical issues.

Static Recovery According to the experiments shown in Section 4.2, many materials regained some, if not all of their strength after annealing, providing evidence that the Mullins effect is not a strictly irreversible process. For the purpose of modeling the recovery of the Mullins effect, the static recovery term is taken in a temperature dependent Arrhenius form

$$r = r_0 \exp\left\{-\frac{Q}{R\vartheta}\right\}|\nu_* - \nu_{\rm s}| \qquad \text{with} \qquad \nu_* = \hat{\nu}_*(\vartheta)\,. \tag{4.45}$$

In (4.45), r_0 is a pre-exponential factor, Q is an activation energy, R the gas constant, and ϑ the absolute temperature. The parameter ν_* in (4.45) sets the saturation value of the volume fraction of the soft domain due to thermal recovery. Taking guidance from the experimental results of [59] (shown in Figure 4.2) the saturation value ν_* is taken to be temperature dependent. However, since data is not readily available, we

[2]This type of evolution equation was presented in [58] in a continuum damage mechanics context.

are unable to calibrate ν_*, and therefore we assume $\nu_* = \nu_{s0}$ in the remainder of this paper.

4.6 Governing Equations

The governing equations include:

- The local force balance,

$$\left.\begin{aligned} \operatorname{div}\mathbf{T} + \mathbf{b} = \mathbf{0} \quad &\text{in} \quad \mathcal{B}_t, \\ \mathbf{u} = \breve{\mathbf{u}} \quad &\text{on} \quad \mathcal{S}_{\mathbf{u}}, \\ \mathbf{T}\mathbf{n} = \breve{\mathbf{t}} \quad &\text{on} \quad \mathcal{S}_{\mathbf{t}} \end{aligned}\right\} \tag{4.46}$$

  with $\mathbf{T}$ given by (4.41). Here $\mathcal{S}_{\mathbf{u}}$ and $\mathcal{S}_{\mathbf{t}}$ are complementary subsurfaces of the boundary $\partial\mathcal{B}_t$ of the body $\mathcal{B}_t$ in the sense that $\partial\mathcal{B}_t = \mathcal{S}_{\mathbf{u}} \cup \mathcal{S}_{\mathbf{t}}$ and $\mathcal{S}_{\mathbf{u}} \cap \mathcal{S}_{\mathbf{t}} = \varnothing$. The initial data is taken as

$$\mathbf{u}(\mathbf{x}_{\mathrm{R}}, 0) = \mathbf{u}_0(\mathbf{x}_{\mathrm{R}}) \quad \text{in} \quad \mathcal{B}_{\mathrm{R}}. \tag{4.47}$$

- The balance of energy (4.35), with our specific constitutive equations, gives the partial differential equation and boundary conditions for the temperature field,

$$\left.\begin{aligned} \rho C\dot{\vartheta} = \operatorname{div}(\kappa \operatorname{grad}\vartheta) + s \quad &\text{in} \quad \mathcal{B}_t, \\ \vartheta = \breve{\vartheta} \quad &\text{on} \quad \mathcal{S}_{\vartheta}, \\ -\mathbf{q}\cdot\mathbf{n} = \breve{q} \quad &\text{on} \quad \mathcal{S}_{q}. \end{aligned}\right\} \tag{4.48}$$

  where s is the heat source/sink term given by

$$s = q + J^{-1}F\dot{\nu}_{\mathrm{s}} + \frac{1}{2}J^{-1}\vartheta\frac{\partial \mathbf{S}}{\partial \vartheta} : \dot{\mathbf{C}} - J^{-1}\vartheta\frac{\partial F}{\partial \vartheta}\dot{\nu}_{\mathrm{s}}\,. \tag{4.49}$$

  Similarly, $\mathcal{S}_{\vartheta}$ and $\mathcal{S}_q$ are complementary subsurfaces of the boundary $\partial\mathcal{B}_t$ of the body $\mathcal{B}_t$ in the sense that $\partial\mathcal{B}_t = \mathcal{S}_{\vartheta} \cup \mathcal{S}_q$ and $\mathcal{S}_{\vartheta} \cap \mathcal{S}_q = \varnothing$. The initial data is

taken as

$$\vartheta(\mathbf{x}_{\mathrm{R}}, 0) = \vartheta_0(\mathbf{x}_{\mathrm{R}}) \quad \text{in} \quad \mathcal{B}_{\mathrm{R}}. \tag{4.50}$$

4.7 Calibration to Uniaxial Experiments

To calibrate the model, a one-dimensional uniaxial stress version of the constitutive model was implemented in MATLAB so that we may utilize the nonlinear least squares algorithms for the calibration. The experiments conducted by [33] and shown in Figures 4.1a-c on eight different variants of three materials are used here for the purpose of calibration.

In their experiments, all eight variants of the *virgin* filled rubber were subjected to a first stretching and then the second stretching. That deformation history was followed by stress-free annealing in vacuum at 100°C for 24 hours. After annealing, the third stretching was performed to assess recovery. All tensile tests were performed at room temperature with a constant stretch rate of $2\,\mathrm{min}^{-1}$.

The experimentally measured stress-stretch curves for all eight variants of the three materials used by [33] are shown in Figures 4.3, 4.4 and 4.5. A nonlinear least squares fit is performed on the error between the measured nominal stress and nominal model stress through the standard relation $\mathbf{P} = J\mathbf{T}\mathbf{F}^{-\top}$, in which in $\mathbf{T}$ is given by (4.41). For calibration, the absolute temperature is kept fixed at $\vartheta = 373\,\mathrm{K}$, and $R = 8.314\,\mathrm{J/(mol\ K)}$ as is standard. The calibrated material parameters are provided in Table 4.1, and the corresponding model behavior shown as solid lines in Figures 4.3, 4.4 and 4.5. From these Figures, it is clear that the model is able to capture the behavior for all the experiments from [33], and is well calibrated to them.

4.8 Behavior of the Model

The performance of the proposed model is presented by providing results using a representative material, here we choose Type C with 0.5% CC, which subjected

Table 4.1 Calibrated Parameters for the Eight Different Variants of Three Rubber Vulcanizates Reported by Harwood and Payne (1967)

Material Type	G_0 (kPa)	λ_L	A	ν_{s0}	ν_{ss}	r_0 (s^{-1})	Q (J/mol)
A with 4.17% S	250	4.08	0.107	0.73	0.88	-4.07×10^{-6}	14.32
A with 2.5% S	160	4.56	0.109	0.72	0.88	-2.87×10^{-6}	53.94
A with 1.25% S	90	4.98	0.103	0.71	0.89	-7.07×10^{-5}	48.31
B with 0.6% S	230	3.67	0.24	0.77	0.90	-1.85×10^{-5}	0.60
B with 0.4% S	110	4.99	0.04	0.69	0.87	-2.01×10^{-5}	97.7
B with 0.2% S	100	5.41	0.05	0.74	0.91	-1.86×10^{-5}	44.38
C with 3.5% CC	140	5.44	0.03	0.64	0.89	-2.30×10^{-5}	101.24
C with 0.5% CC	50	7.49	0.06	0.72	0.87	-5.35×10^{-5}	100.00

to different loading scenarios. This particular material was chosen since it shows significant recovery in the Mullins effect. First, the typical Mullins effect is shown by performing cyclic loading with different maximum stretches at room temperature. Second, the recovery of the Mullins effect is demonstrated by simulating annealing between deformation cycles. And lastly, three-dimensional simulations of a specimen with a hole undergoes a cyclic loading followed by an annealing process at different temperatures are demonstrated.

4.8.1 Cyclic Uniaxial Tensile Behavior without Annealing

To demonstrate how the model predicts the Mullins effect at room temperature 300 K without annealing, we consider a loading where the material is subjected to cyclic uniaxial tensile stretching. The applied stretch profile is shown in Figure 4.6a, the corresponding nominal stress – stretch curve is shown in Figure 4.6b, both ν_s - time and ν_s - stretch curves are plotted in Figure 4.6c and d, respectively. During the initial loading, the stress – stretch curve shows a typical hyperelastic response, and ν_s

evolves and increases from its initial value. One may observe that the stress response becomes more compliant after unloading at stretch of 6, and ν_s remains constant during unloading. Upon reloading, the stress – stretch curve follows the previous unloading curve and rejoins the primary loading curve at the previous maximum stretch of 6. Meanwhile, the ν_s remained constant up to the maximum prior stretch of 6. When the material is subjected to further deformation, beyond a stretch of 6, the stress – stretch curve extends the primary path with ν_s evolving even further. The stress – stretch response is even more compliant during the second unloading, and again ν_s remains constant during the second unloading.

4.8.2 Cyclic Uniaxial Tensile Behavior with Annealing

Next we demonstrate how our model predicts the recovery of Mullins effects for different recovery times at room temperature, as well as for annealing between deformation cycles at various elevated temperatures. The prescribed loading sequence is as follows: 1) loading, 2) unloading, 3) stress free annealing at a constant temperature for a variable time, 4) reloading, and lastly 5) unloading. The sequence is shown in in Figure 4.7a, where the sequence is denoted by numbers.

Room Temperature Annealing For the case of two days of annealing, Figure 4.7b shows the evolution of ν_s with stretch. It is clear that the evolution of ν_s starts with an initial value $\nu_{s0} = 0.72$ and then reaches 0.788 during the first loading and stays at the current value during the first unloading. However, during annealing, ν_s decreases with time to a value of 0.728 due to static recovery. Upon the second loading ν_s resumes evolving until reaching 0.788, and again remains constant during during unloading. Figures 4.7c and 4.7d show the effects of different recovery times on both ν_s - stretch curve and nominal stress - stretch curve. In these figures, the solid lines denote the behavior after various recovery times, while the dashed line represents the virgin response. One may observe that the material with a recovery

time of three days almost fully recovers back to the virgin response, while the one that is annealed for only one day regains about half of its virgin strength, and finally the one with an annealing time of two days, as expected, falls in between.

Elevated Temperature Annealing The effect of temperature on recovery is also investigated, the same loading profile and sequence as shown in Figure 4.7a is used, but now annealed stress free at three different fixed temperatures of 30°C, 60°C, and 100°C. The evolution of ν_s with time is shown in Figure 4.8a, solid lines with different colors represent the recovery response under the different elevated temperatures of 30°C, 60°C, and 100°C. As we expected, ν_s recovers more when the material subjected to a higher elevated temperature during annealing. Figure 4.8b shows the corresponding stress - stretch curves, the dashed line is the virgin response, while the solid lines with different colors denote the response after annealing at the various elevated temperatures. It is clear that with higher elevated temperature, the material tends to recover closer to its virgin state, and faster.

4.8.3 Representative 3D Finite Element Simulation

In this section, for the purpose of showing how the model behaves in a complex three-dimensional loading scenerio, the constitutive model is numerically implemented in Abaqus by writing a user-defined material subroutine (UMAT). Specifically, we consider a rectangular strip of material with a notch in center, that undergoes cyclic tension at room temperature 27°C followed by constant strain annealing at various elevated temperatures.

The three-dimensional geometry under consideration is a rectangular specimen with a height $2H = 200\,\text{mm}$, a width of $2W = 100\,\text{mm}$, and a thickness of $t = 4\,\text{mm}$, along with a through thickness notch of length $2a = 10\,\text{mm}$ centrally located. Using the symmetry, only one quarter of the geometry is modeled in the simulation and shown in Figure 4.9. Also, the zoom-in view in Figure 4.9 details the geometry of

the notch, with a tip radius of $R = 0.5\,\text{mm}$. The entire quarter-body is meshed with 2140 U3D8H elements, with the mesh close to the notch shown in Figure 4.9.

For simplicity, since the time scale for heat conduction is fast relative to that of recovery, we assume that the temperature is uniform, and prescribe the temperature for all times at all nodes of the mesh. For boundary conditions, referring to Figure 4.9, a displacement u is prescribed on face AB only in the 2 direction with a loading profile shown in Figure 4.10a. Further, faces AE and CD are assigned appropriate symmetry conditions, and all other faces are traction free. For temperature boundary conditions, we prescribe a uniform temperature of 27°C during the cyclic loading, followed by a 4 hours annealing process at three different temperatures of 27°C, 50°C and 100°C.

Figure 4.10b shows the time-history of stress component σ_{22} measured at the notch root, point D in Figure 4.9, the markers with Roman numerals from I) to VI) indicate the snapshots taken at different times of 3s, 7s, 10s, 50s, 7250s and 14450s, respectively. The corresponding contour plots of the soft volume fraction ν_{s} at the elevated temperature of 100°C are shown in Figure 4.11. As expected, the opening stress component σ_{22} at the notch root increases over time due to the recovery of the Mullins effect. And the increase in stress is proportional to the temperature. These simulated results imply the possibility of unexpected service loads and/or failure may exist, particularly at elevated temperatures over long times.

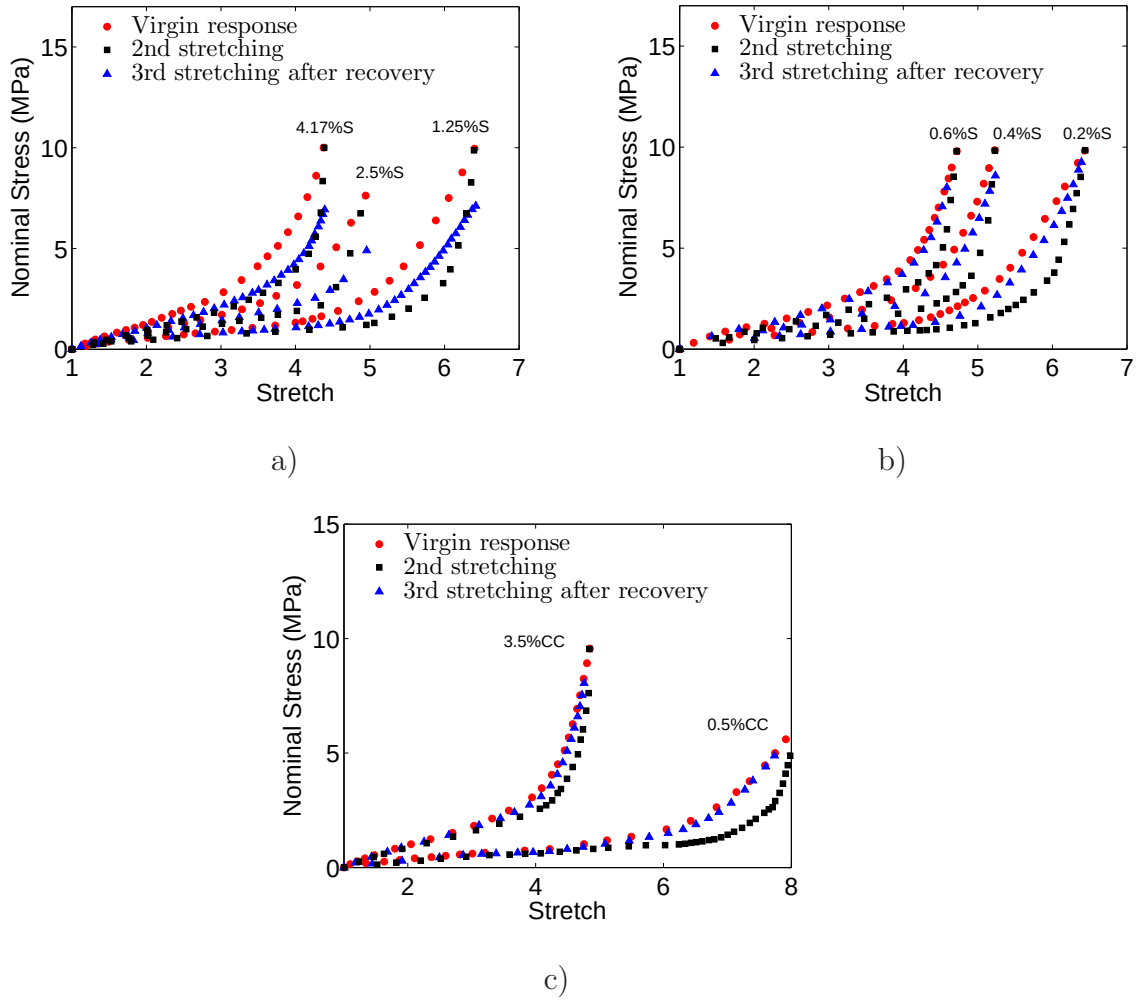

Figure 4.1 Eight variants of filled rubber subjected to a series of tensile tests, showing loading only, the experimental data are reproduced from [33]. a) Type A vulcanizate with three different amounts of polysulfide added as a crosslinker, b) type B vulcanizate with three different amounts of monosulfide added as a crosslinker and c) type C with three different amounts of carbon – carbon added as a crosslinker.

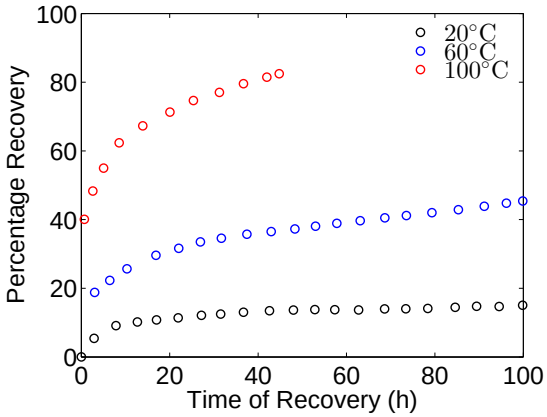

Figure 4.2 Recovery of natural rubber at three different elevated annealing temperatures, the data is reproduced from [59]. The natural rubber was initially prestretched to 420% and then annealed at different temperatures for various time periods. The stress was recorded when the material experienced a second stretch of 200%, the percentage recovery is calculated by taking the ratio of the stress in the initial stretch over the stress in the second stretch.

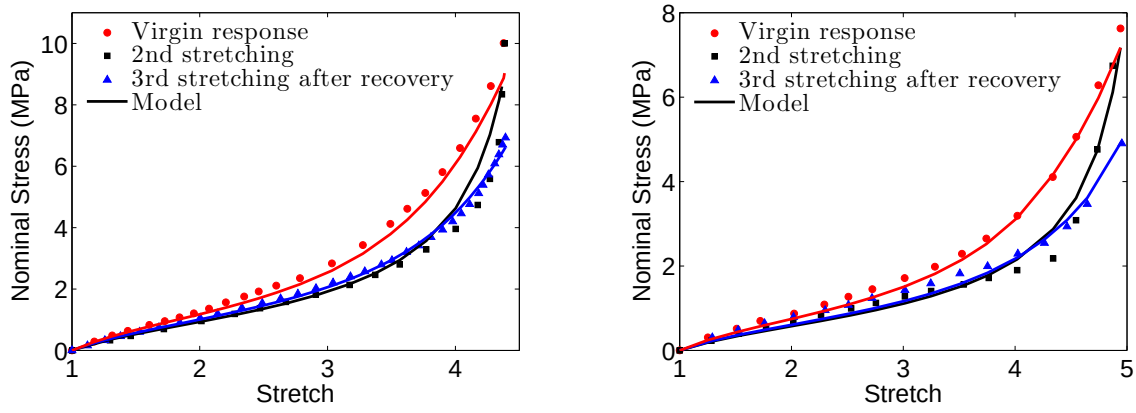

a)

b)

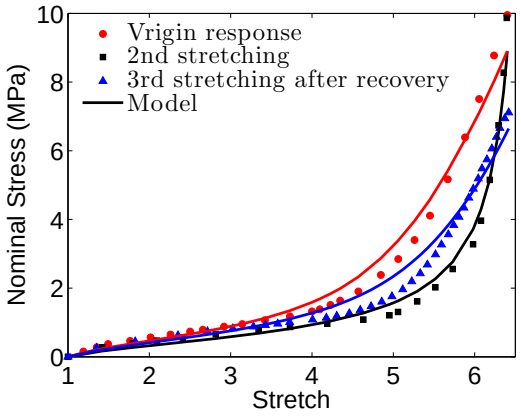

c)

Figure 4.3 Model calibration of type A vulcanizate with different amounts of crosslinker, experiments are shown as markers and the calibrated model as solid lines. a) Vulcanizate with 4.17% sulfur, b) 2.5% sulfur and c) 1.25% sulfur.

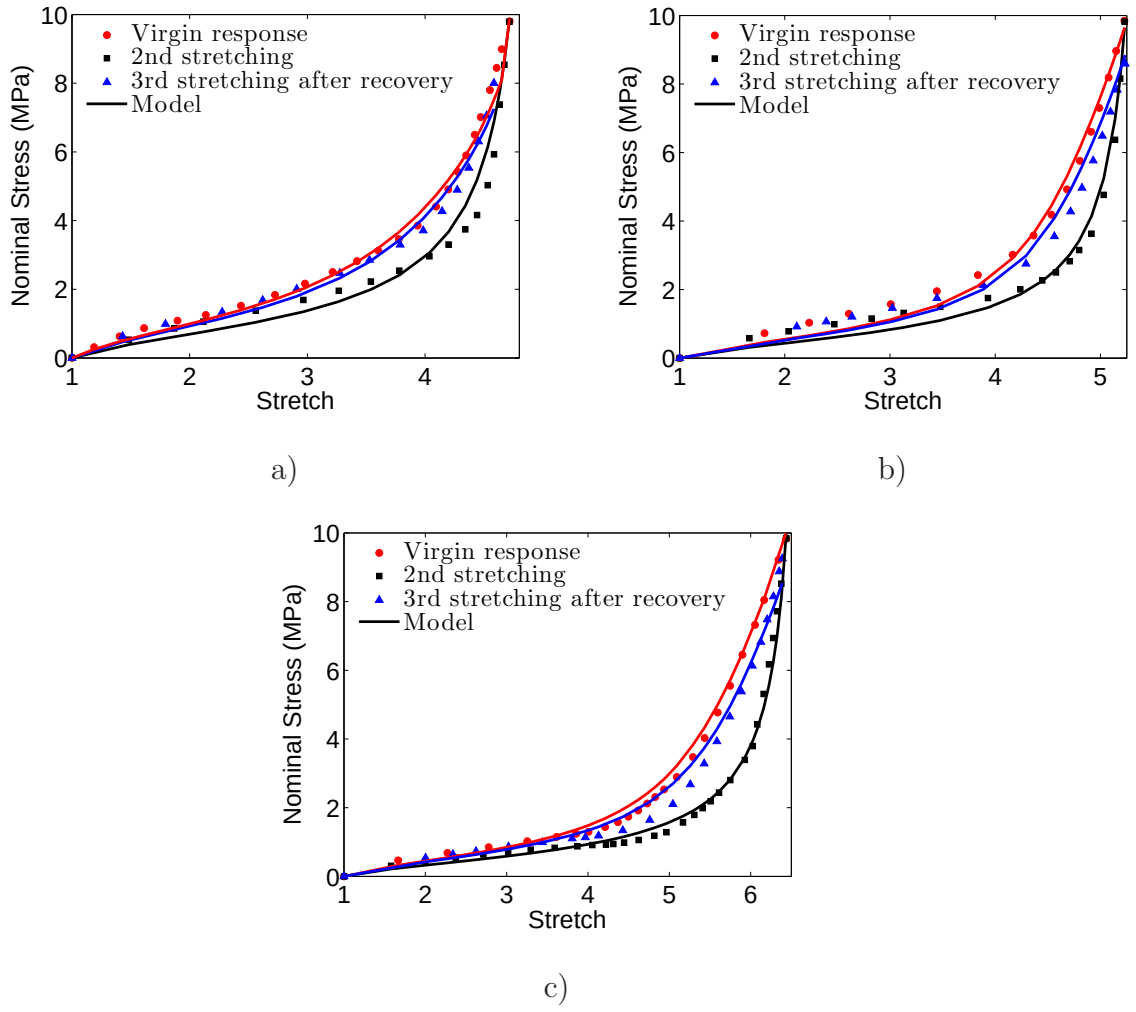

Figure 4.4 Model calibration of type B vulcanizate with different amounts of crosslinker, experiments are shown as markers and the calibrated model as solid lines. a) Vulcanizate with 0.6% sulfur, b) 0.4% sulfur and c) 0.2% sulfur.

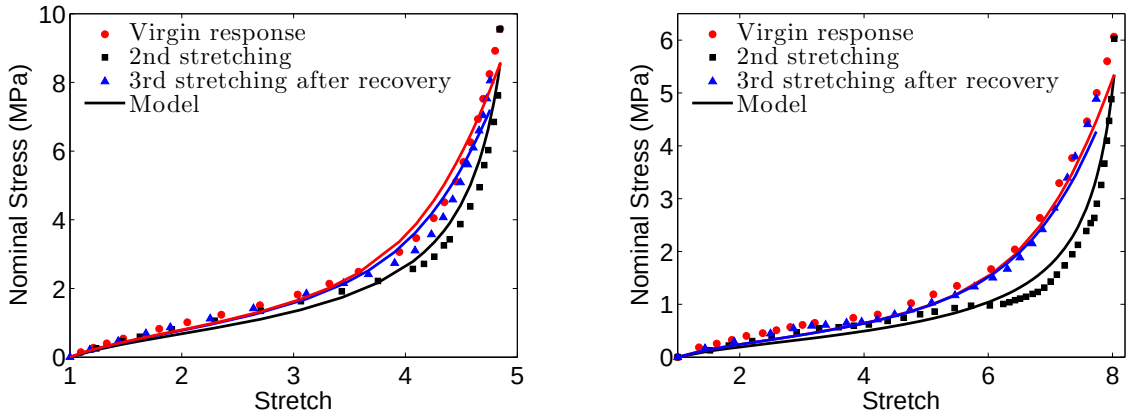

Figure 4.5 Model calibration of type C vulcanizate with different amounts of crosslinker, experiments are shown as markers and the calibrated model as solid lines. a) Vulcanizate with 3.5% CC, and b) 0.5% CC.

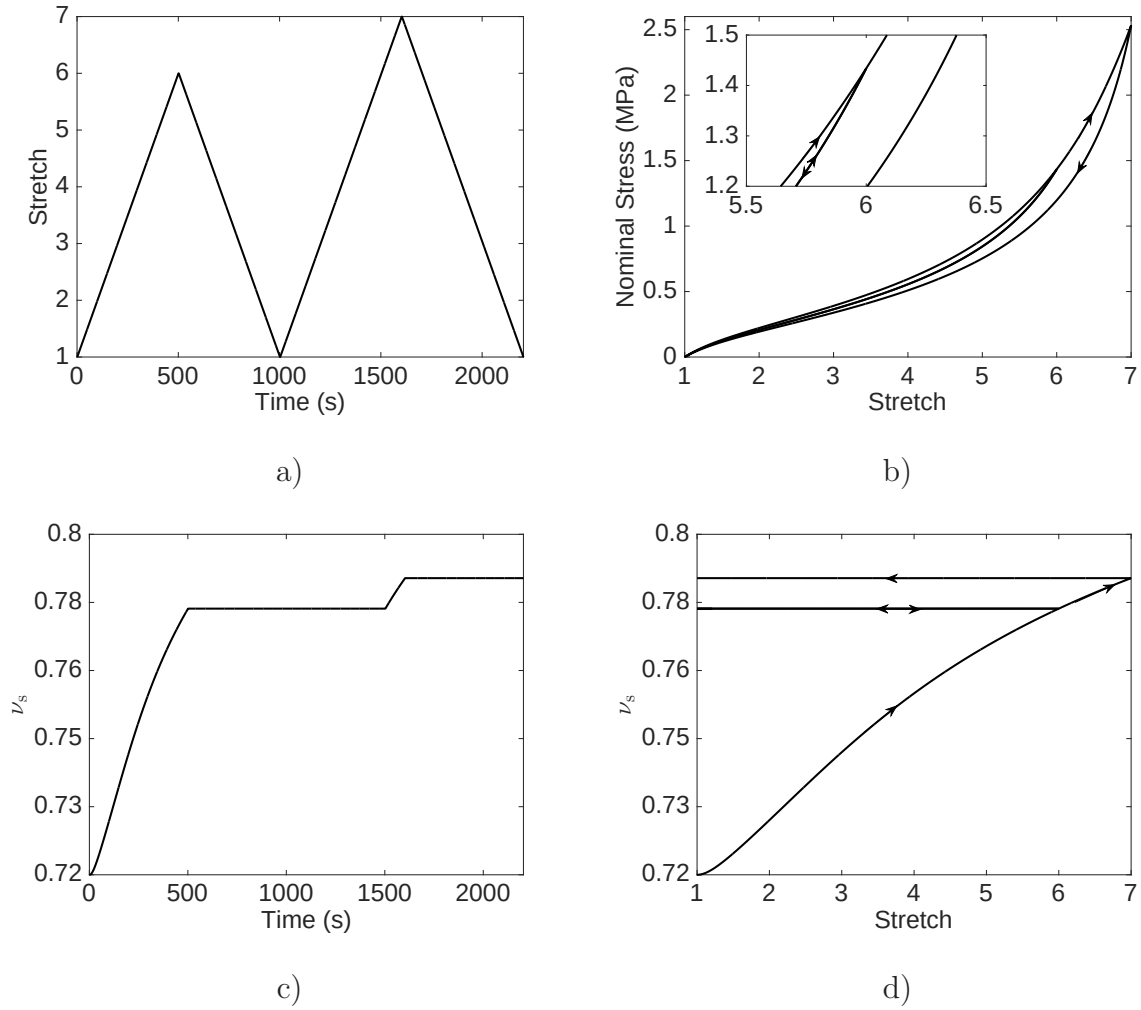

Figure 4.6 Model prediction of the Mullins effect under isothermal conditions without annealing. a) Stretch input as a function of time, b) nominal stress – stretch curve, and the evolution of volume fraction of soft domain plotted against c) time, and d) stretch.

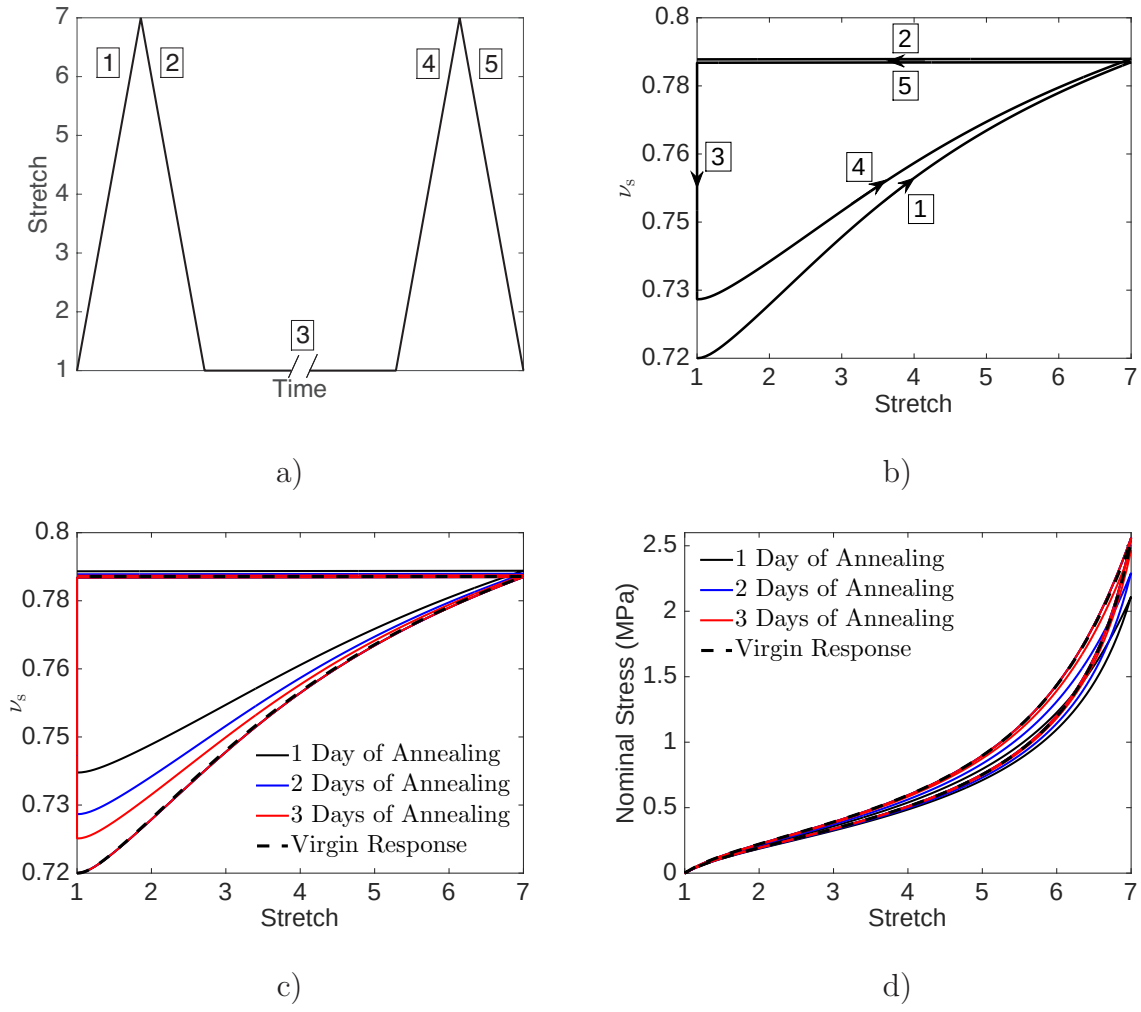

Figure 4.7 Model prediction of Mullins effect recovery due to annealing at room temperature. a) Loading profile with sequence numbered from 1 to 5, b) evolution of volume fraction of soft domain ν_s as a function of stretch for 2 days of annealing, c) evolution of ν_s and d) the nominal stress – stretch response for different annealing times.

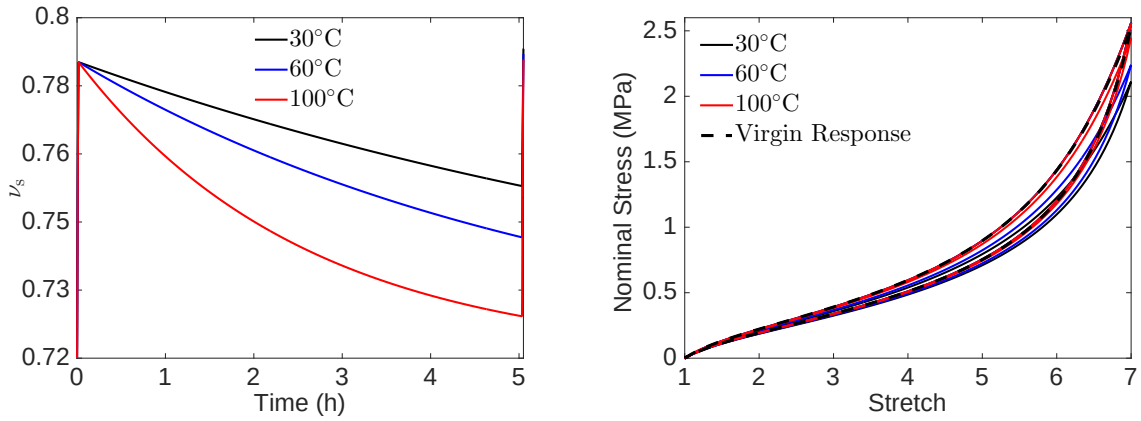

a) b)

Figure 4.8 Model prediction of Mullins effect recovery due to annealing at three different elevated temperatures of 30°C, 60°C and 100°C. a) The evolution of ν_s with time and b) the corresponding nominal stress - stretch response.

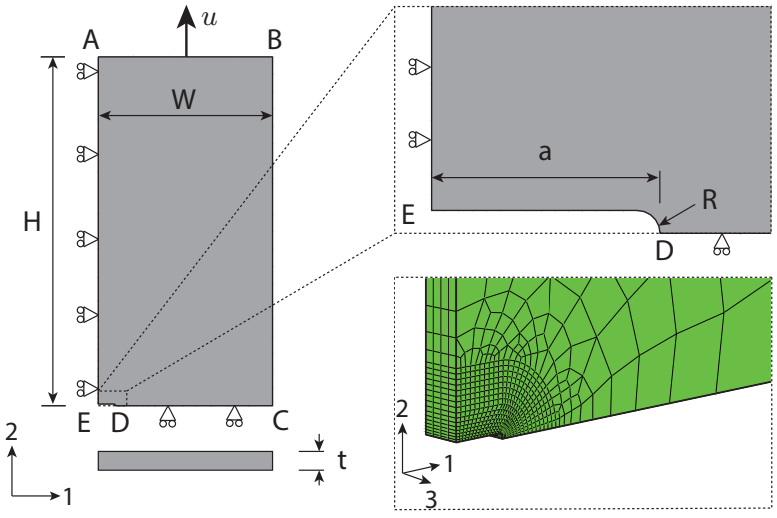

Figure 4.9 Geometry and boundary conditions of specimen with a notch in the center. The left shows a quarter of the geometry is used for the simulation due to the symmetry and the zoom-in view of the notch, and mesh, is shown on the right.

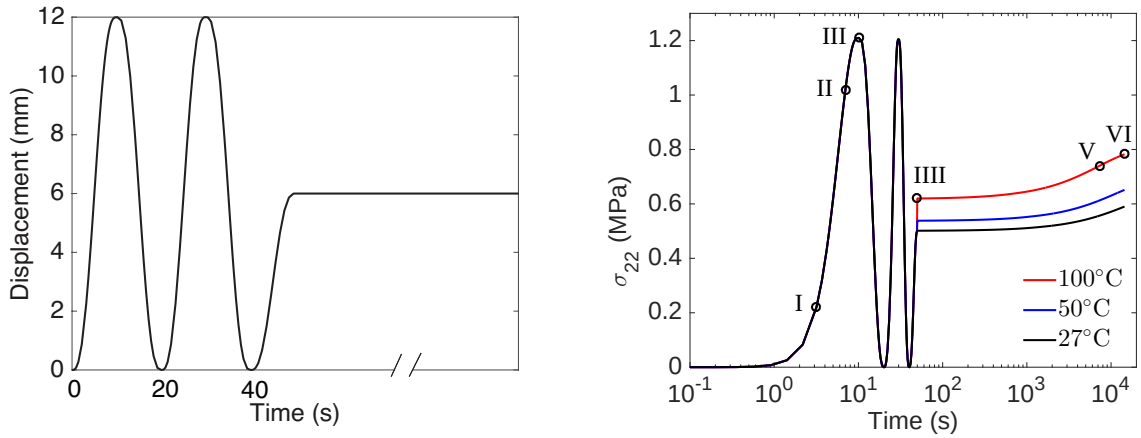

a) b)

Figure 4.10 Results of the specimen with a notch in center undergoes cyclic tension and annealing process. a) The displacement u prescribed on face AB with the function of time, b) the simulated stress component σ_{22} measured at the notch root D as the function of time at three different annealing temperatures of 27°C, 50°C and 100°C. The markers with Roman numeral from I) to VI) indicate the contour plots in Figure 4.11 captured at different times of 3s, 7s, 10s, 50s, 7250s and 14450s.

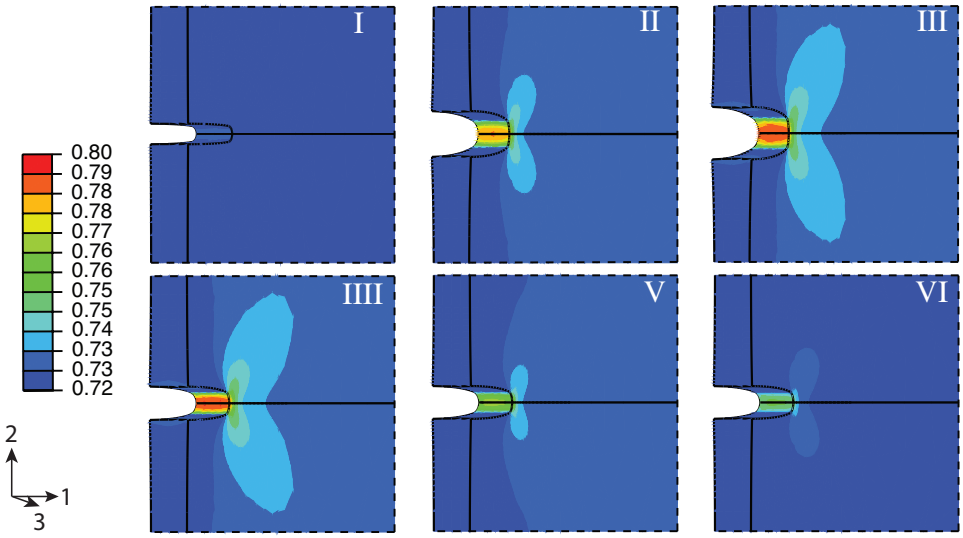

Figure 4.11 3-D Simulation of the specimen with a notch located at the center undergoes a cyclic tension followed by a recovery process under constant strain at the elevated temperatures of 100°C. For clarity, the contour plots of soft volume fraction ν_s are limited to the vicinity of the notch and only the half of the geometry is demonstrated. Three plots in the first row correspond to the snapshots taken at the different times of I) 3s, II) 7s and III) 10s during the first loading cycle. While the second row of snapshots is taken at IIII) 50s, V) 7250s and VI)14450s during the annealing process.

CHAPTER 5

CONCLUSION AND FUTURE DIRECTIONS

5.1 Conclusion

Throughout my four and half years of PhD study, I have gained the knowledge of continuum mechanics as well as numerical implementation of PDEs in terms of finite element method. At the same time, I have also learned the experimental mechanics techniques in mechanical testing. There are multi-field coupling phenomenon as well as inelastic material behavior that I have been studied, namely electro-mechanical coupling, rate-dependent behavior, Mullins effect, and thermal recovery of the Mullins effect. To conclude, I briefly summarize the main contributions of each part of this thesis:

- Part I
  - We have developed a constitutive theory and numerical simulation capability for dielectric viscoelastomers.
  - The theory has been applied to the DVE VHB 4910.
  - The theory has been numerically implemented into Abaqus by writing user defined element subroutine.
  - We have shown that viscoelasticity provides stabilization that delays the onset of instability under monotonic loading and may fully suppress instabilities under sufficiently fast cyclic loading.
- Part II
  - The combined viscoelastic and stress-softening inelastic behavior of the popular filled rubber-like material Viton was experimentally investigated.

  - We developed a thermodynamically consistent model to account rate-dependent, Mullins effect, and asymmetric inelastic behavior concurrently.
  - The model is numerically implemented and validated by comparing the simulation with an inhomogeneous deformation experiment.

- Part III
  - We developed a thermodynamically consistent constitutive model that quantitatively captures the thermal recovery of the Mullins effect.
  - The model is calibrated to a suite of uniaxial experiments (Harwood and Payne, 1967) using a non-linear least square method.
  - The model is numerically implemented into the Abaqus by writing user-defined material subroutine.

5.2 Future Directions

The future directions for soft dielectrics elastomers, filled rubber-like materials, and phase field models are listed below:

- **Soft dielectric elastomers:**

  The electrical behavior of dielectric elastomers can be more complex than considered in this thesis - for example, stretch-dependence of the permittivity or time-dependence of the polarization response - and hence our assumption of an "ideal dielectric" may be an oversimplification in some situations. The missing physics of polarization should be taken into consideration. Lastly, we have not included any consideration of material failure mechanisms in our modeling approach at this time, including material damage or electric breakdown. Accounting for these effects in the simulation capability will be the focus of future work.

- **Filled rubber-like materials:**

  - *Viscous effects & Mullins effects*

    Looking towards the future, there is much more to be done. For example, looking back at the space shuttle Challenger disaster, in many applications rubber-like materials are used at extreme temperatures and/or stretch rates. The combined thermo-mechanical behavior at high stretch rates is an open area with clear opportunity for broad impact. For some special filled rubber-like material systems, the coupling between viscous and Mullins effects could be important and will be our next goal.

  - *Recovery of Mullins effects*

    For recovery of Mullins effects, in light of the progress made this thesis, much improvement yet remains. A suite of comprehensive experiments to measure the transient response of Mullins recovery at various elevated temperatures would greatly improve constitutive models.

- **Phase-field models:**

  - *Polymeric gels*

    The constitutive theory and numerical implementation in this thesis are developed, however the experiments is needed to validate as well as to flesh-out the existing model.

  - *Fracture*

    Looking towards the future, the phase field formulation for fracture will be extended on ductile material which will undergoes finite deformation. Different dissipative mechanisms will be incorporated into the materials for resisting the crack propagation. For numerical perspective, a stagger scheme will be used for purpose of decreasing the simulation time.

Furthermore, a suite of comprehensive experiments are needed for the model validation.

APPENDIX A

THERMODYNAMIC CONSISTENCY OF THE VITON'S CONSTITUTIVE MODEL

For this isothermal system, the first and second laws of thermodynamics may be combined into a free energy imbalance. That imbalance states that the time rate of change of free energy in a part $\mathcal{P}_{\mathrm{R}}$ of the reference body $\mathcal{B}_{\mathrm{R}}$ is less than or equal to the power expended on $\mathcal{P}_{\mathrm{R}}$. Then the free energy imbalance for each part $\mathcal{P}_{\mathrm{R}}$ is given by

$$\overline{\int_{\mathcal{P}_{\mathrm{R}}} \psi_{\mathrm{R}} dv_{\mathrm{R}}}^{\cdot} \leq \mathcal{W}_{\mathrm{ext}}(\mathcal{P}_{\mathrm{R}}) = \int_{\partial\mathcal{P}_{\mathrm{R}}} \mathbf{T}_{\mathrm{R}}\mathbf{n}_{\mathrm{R}} \cdot \dot{\boldsymbol{\chi}} da_{\mathrm{R}} + \int_{\mathcal{P}_{\mathrm{R}}} \mathbf{b} \cdot \dot{\boldsymbol{\chi}} dv_{\mathrm{R}} \,. \tag{A.1}$$

Next, bringing the derivative inside the integral on the left hand side, and applying the divergence theorem to the right hand side, one arrives at the local free energy imbalance

$$\dot{\psi}_{\mathrm{R}} - \mathbf{T}_{\mathrm{R}} : \dot{\mathbf{F}} \leq 0 \,. \tag{A.2}$$

Then using standard arguments from continuum mechanics, the stress power $\mathbf{T}_{\mathrm{R}} : \dot{\mathbf{F}}$ may be written in the form $\frac{1}{2}\mathbf{S} : \dot{\mathbf{C}}$, where

$$\mathbf{S} = J\mathbf{F}^{-1}\mathbf{T}\mathbf{F}^{-\top} \tag{A.3}$$

is the 2nd Piola stress, and therefore the local free energy imbalance takes the frame invariant form

$$\dot{\psi}_{\mathrm{R}} - \frac{1}{2}\mathbf{S} : \dot{\mathbf{C}} \leq 0 \,. \tag{A.4}$$

In this model, total free energy has the functional form $\psi_{\mathrm{R}} = \hat{\psi}_{\mathrm{R}}(\mathbf{C}, \nu_{\mathrm{s}}, \mathbf{A}^{(1)}, ..., \mathbf{A}^{(N)})$, after taking the time derivative we have

$$\dot{\psi}_{\mathrm{R}} = \frac{\partial \psi_{\mathrm{R}}}{\partial \mathbf{C}} : \dot{\mathbf{C}} + \frac{\partial \psi_{\mathrm{R}}}{\partial \nu_{\mathrm{s}}} \dot{\nu}_{\mathrm{s}} + \sum_{\alpha=1}^{N} \frac{\partial \psi_{\mathrm{R}}}{\partial \mathbf{A}^{(\alpha)}} : \dot{\mathbf{A}}^{(\alpha)}. \tag{A.5}$$

Inserting (A.5) to (A.4) and rearranging terms, we obtain

$$\frac{1}{2}\left[\mathbf{S} - 2\frac{\partial \psi_{\mathrm{R}}}{\partial \mathbf{C}}\right] : \dot{\mathbf{C}} - \frac{\partial \psi_{\mathrm{R}}}{\partial \nu_{\mathrm{s}}} \dot{\nu}_{\mathrm{s}} - \sum_{\alpha=1}^{N} \frac{\partial \psi_{\mathrm{R}}}{\partial \mathbf{A}^{(\alpha)}} : \dot{\mathbf{A}}^{(\alpha)} \geq 0. \tag{A.6}$$

Now, since for any arbitrary deformation the 2nd Piola Kirchhoff stress and Cauchy stress are

$$\mathbf{S} = 2\frac{\partial \psi_{\mathrm{R}}}{\partial \mathbf{C}}, \quad \text{and} \quad \mathbf{T} = J^{-1}\mathbf{F}\mathbf{S}\mathbf{F}^{\top} = 2J^{-1}\mathbf{F}\frac{\partial \psi_{\mathrm{R}}}{\partial \mathbf{C}}\mathbf{F}^{\top}. \tag{A.7}$$

Following the second law of thermodynamics, the dissipation must be non-negative

$$\mathcal{D} = -\frac{\partial \psi_{\mathrm{R}}}{\partial \nu_{\mathrm{s}}} \dot{\nu}_{\mathrm{s}} - \sum_{\alpha=1}^{N} \frac{\partial \psi_{\mathrm{R}}}{\partial \mathbf{A}^{(\alpha)}} : \dot{\mathbf{A}}^{(\alpha)} \geq 0, \tag{A.8}$$

where the first term and second term are the contribution from Mullins effect and viscous effects, respectively. Clearly, (A.8) indicates that evolution of soft domain ν_{s} in Mullins effect and evolution of tensorial like internal variables $\mathbf{A}^{(\alpha)}$ in viscous effect are both dissipative processes. After differentiating the second term using (3.17) and (3.22), the dissipation then becomes

$$\mathcal{D} = -\frac{\partial \psi_{\mathrm{R}}}{\partial \nu_{\mathrm{s}}} \dot{\nu}_{\mathrm{s}} - \sum_{\alpha=1}^{N} \frac{G_{\mathrm{neq}}^{(\alpha)}}{2\tau^{(\alpha)}} \left[\mathbf{C}_{\mathrm{dis}} - (\mathbf{A}^{(\alpha)})^{-1}\right] : \left[\mathbf{C}_{\mathrm{dis}}^{-1} - \mathbf{A}^{(\alpha)}\right] \geq 0\,. \tag{A.9}$$

Where, [71] and [48] have shown that

$$\frac{\partial \psi_{\mathrm{R}}}{\partial \nu_{\mathrm{s}}} \dot{\nu}_{\mathrm{s}} \leq 0 \quad \text{and} \quad \left[\mathbf{C}_{\mathrm{dis}} - (\mathbf{A}^{(\alpha)})^{-1}\right] : \left[\mathbf{C}_{\mathrm{dis}}^{-1} - \mathbf{A}^{(\alpha)}\right] \leq 0\,, \tag{A.10}$$

and with $G_{\mathrm{neq}}^{(\alpha)} \geq 0$, and $\tau^{(\alpha)} \geq 0$, the constitutive equations satisfy thermodynamics.

BIBLIOGRAPHY

[1] Abaqus/Standard. *Abaqus Reference Manuals*. Dassault Systemes Simulia, Providence, RI, 2017.

[2] Lallit Anand. A constitutive model for compressible elastomeric solids. *Computational Mechanics*, 18(5):339–355, 1996.

[3] Ellen M Arruda and Mary C Boyce. A three-dimensional constitutive model for the large stretch behavior of rubber elastic materials. *Journal of the Mechanics and Physics of Solids*, 41(2):389–412, 1993.

[4] Jorgen S Bergström and Mary C Boyce. Constitutive modeling of the large strain time-dependent behavior of elastomers. *Journal of the Mechanics and Physics of Solids*, 46(5):931–954, 1998.

[5] Jorgen S Bergström and Mary C Boyce. Mechanical behavior of particle filled elastomers. *Rubber chemistry and technology*, 72(4):633–656, 1999.

[6] Jorgen S Bergström and Mary C Boyce. Large strain time-dependent behavior of filled elastomers. *Mechanics of materials*, 32(11):627–644, 2000.

[7] Katia Bertoldi and Massimiliano Gei. Instabilities in multilayered soft dielectrics. *Journal of the Mechanics and Physics of Solids*, 59(1):18–42, 2011.

[8] Paul Brochu and Qibing Pei. Advances in dielectric elastomers for actuators and artificial muscles. *Macromolecular rapid communications*, 31(1):10–36, 2010.

[9] Alex Büschel, Sven Klinkel, and Werner Wagner. Dielectric elastomers–numerical modeling of nonlinear visco-electroelasticity. *International Journal for Numerical Methods in Engineering*, 93(8):834–856, 2013.

[10] Federico Carpi, Danilo De Rossi, Roy Kornbluh, Ronald Edward Pelrine, and Peter Sommer-Larsen. *Dielectric elastomers as electromechanical transducers: fundamentals, materials, devices, models and applications of an emerging electroactive polymer technology*. Elsevier, 2011.

[11] Chellappa Chandrasekaran. *Rubber seals for fluid and hydraulic systems*. William Andrew, 2009.

[12] Shawn A Chester and Lallit Anand. A thermo-mechanically coupled theory for fluid permeation in elastomeric materials: application to thermally responsive gels. *Journal of the Mechanics and Physics of Solids*, 59(10):1978–2006, 2011.

[13] Shawn A Chester, Claudio V Di Leo, and Lallit Anand. A finite element implementation of a coupled diffusion-deformation theory for elastomeric gels. *International Journal of Solids and Structures*, 52:1–18, 2015.

[14] Samuel K Clark. *Mechanics of pneumatic tires*. US Government Printing Office, 1981.

[15] Eduardo de Souza Neto, Djordje Perić, M Dutko, and DRJ Owen. Design of simple low order finite elements for large strain analysis of nearly incompressible solids. *International Journal of Solids and Structures*, 33(20-22):3277–3296, 1996.

[16] Martina Decker. Time–space–matter emergent materials in architecture. *MRS Online Proceedings Library Archive*, 1800, 2015.

[17] Julie Diani, Bruno Fayolle, and Pierre Gilormini. A review on the mullins effect. *European Polymer Journal*, 45(3):601–612, 2009.

[18] Luis Dorfmann and Ray Ogden. A pseudo-elastic model for loading, partial unloading and reloading of particle-reinforced rubber. *International Journal of Solids and Structures*, 40(11):2699–2714, 2003.

[19] Luis Dorfmann and Ray Ogden. A constitutive model for the mullins effect with permanent set in particle-reinforced rubber. *International Journal of Solids and Structures*, 41(7):1855–1878, 2004.

[20] Luis Dorfmann and Ray Ogden. Nonlinear electroelasticity. *Acta Mechanica*, 174(3-4):167–183, 2005.

[21] Luis Dorfmann and Ray W Ogden. Instabilities of an electroelastic plate. *International Journal of Engineering Science*, 77:79–101, 2014.

[22] Aleksey D Drozdov and Al Dorfmann. Stress-softening and recovery of elastomers. *arXiv preprint cond-mat/0102052*, 2001.

[23] Choon Chiang Foo and Zhi-Qian Zhang. A finite element method for inhomogeneous deformation of viscoelastic dielectric elastomers. *International Journal of Applied Mechanics*, 7(05):1550069, 2015.

[24] Alan N Gent. A new constitutive relation for rubber. *Rubber chemistry and technology*, 69(1):59–61, 1996.

[25] Sanjay Govindjee and Juan Simo. A micro-mechanically based continuum damage model for carbon black-filled rubbers incorporating mullins' effect. *Journal of the Mechanics and Physics of Solids*, 39(1):87–112, 1991.

[26] Melville S. Green and Arthur V. Tobolsky. A new approach to the theory of relaxing polymeric media. *The Journal of Chemical Physics*, 14(2):80–92, 1946.

[27] Jingkai Guo, Rui Xiao, Harold S Park, and Thao D Nguyen. The temperature-dependent viscoelastic behavior of dielectric elastomers. *Journal of Applied Mechanics*, 82(9):091009, 2015.

[28] Morton E Gurtin, Eliot Fried, and Lallit Anand. *The mechanics and thermodynamics of continua*. Cambridge University Press, 2010.

[29] Eugene Guth. Theory of filler reinforcement. *Journal of applied physics*, 16(1):20–25, 1945.

[30] David E Hanson, Marilyn Hawley, Robert Houlton, Kiran Chitanvis, Philip Rae, E Bruce Orler, and Debra A Wrobleski. Stress softening experiments in silica-filled polydimethylsiloxane provide insight into a mechanism for the mullins effect. *Polymer*, 46(24):10989–10995, 2005.

[31] Jac Harwood, Leonard Mullins, and Arthur R Payne. Stress softening in natural rubber vulcanizates. part ii. stress softening effects in pure gum and filler loaded rubbers. *Journal of Applied Polymer Science*, 9(9):3011–3021, 1965.

[32] Jac Harwood and Arthur R Payne. Stress softening in natural rubber vulcanizates. part iii. carbon black-filled vulcanizates. *Journal of Applied Polymer Science*, 10(2):315–324, 1966.

[33] Jac Harwood and Arthur R Payne. Stress softening in natural rubber vulcanizates. iv. unfilled vulcanizates. *Rubber Chemistry and Technology*, 40(3):840–848, 1967.

[34] David L Henann and Katia Bertoldi. Modeling of elasto-capillary phenomena. *Soft Matter*, 10(5):709–717, 2014.

[35] David L Henann, Shawn A Chester, and Katia Bertoldi. Modeling of dielectric elastomers: Design of actuators and energy harvesting devices. *Journal of the Mechanics and Physics of Solids*, 61(10):2047–2066, 2013.

[36] Gerhard A Holzapfel and Juan C Simo. A new viscoelastic constitutive model for continuous media at finite thermomechanical changes. *International Journal of Solids and Structures*, 33(20-22):3019–3034, 1996.

[37] Wei Hong. Modeling viscoelastic dielectrics. *Journal of the Mechanics and Physics of Solids*, 59(3):637–650, 2011.

[38] Mokarram Hossain, Duc Khoi Vu, and Paul Steinmann. Experimental study and numerical modelling of vhb 4910 polymer. *Computational Materials Science*, 59:65–74, 2012.

[39] Mokarram Hossain, Duc Khoi Vu, and Paul Steinmann. A comprehensive characterization of the electro-mechanically coupled properties of vhb 4910 polymer. *Archive of Applied Mechanics*, 85(4):523–537, 2015.

[40] Michael Kaliske and H Rothert. Formulation and implementation of three-dimensional viscoelasticity at small and finite strains. *Computational Mechanics*, 19(3):228–239, 1997.

[41] Christoph Keplinger, Tiefeng Li, Richard Baumgartner, Zhigang Suo, and Siegfried Bauer. Harnessing snap-through instability in soft dielectrics to achieve giant voltage-triggered deformation. *Soft Matter*, 8(2):285–288, 2012.

[42] Christoph Keplinger, Jeong-Yun Sun, Choon Chiang Foo, Philipp Rothemund, George M Whitesides, and Zhigang Suo. Stretchable, transparent, ionic conductors. *Science*, 341(6149):984–987, 2013.

[43] Kamran A Khan, Husam Wafai, and Tamer El Sayed. A variational constitutive framework for the nonlinear viscoelastic response of a dielectric elastomer. *Computational Mechanics*, 52(2):345–360, 2013.

[44] Manfred Klüppel and Joachim Schramm. A generalized tube model of rubber elasticity and stress softening of filler reinforced elastomer systems. *Macromolecular theory and simulations*, 9(9):742–754, 2000.

[45] Guggi Kofod, Roy Kornbluh, Ron Pelrine, and Peter Sommer-Larsen. Actuation response of polyacrylate dielectric elastomers. In *Proc. SPIE*, volume 4329, 2001.

[46] Roy D Kornbluh, Ron Pelrine, Harsha Prahlad, Annjoe Wong-Foy, Brian McCoy, Susan Kim, Joseph Eckerle, and Tom Low. Dielectric elastomers: Stretching the capabilities of energy harvesting. *MRS bulletin*, 37(3):246–253, 2012.

[47] Fazilay Laraba-Abbes, Patrick Ienny, and Roland Piques. A new tailor-mademethodology for the mechanical behaviour analysis of rubber-like materials: Ii. application to the hyperelastic behaviour characterization of a carbon-black filled natural rubber vulcanizate. *Polymer*, 44(3):821–840, 2003.

[48] Christian Linder, Mykola Tkachuk, and Christian Miehe. A micromechanically motivated diffusion-based transient network model and its incorporation into finite rubber viscoelasticity. *Journal of the Mechanics and Physics of Solids*, 59(10):2134–2156, 2011.

[49] Alexander Lion. A constitutive model for carbon black filled rubber: experimental investigations and mathematical representation. *Continuum Mechanics and Thermodynamics*, 8(3):153–169, 1996.

[50] Alexander Lion. A physically based method to represent the thermo-mechanical behaviour of elastomers. *Acta Mechanica*, 123(1):1–25, 1997.

[51] Tongqing Lu, Jikun Wang, Ruisen Yang, and TJ Wang. A constitutive model for soft materials incorporating viscoelasticity and mullins effect. *Journal of Applied Mechanics*, 84(2):021010, 2017.

[52] Jacob Lubliner. A model of rubber viscoelasticity. *Mechanics Research Communications*, 12(2):93–99, 1985.

[53] Yunwei Mao, Shaoting Lin, Xuanhe Zhao, and Lallit Anand. A large deformation viscoelastic model for double-network hydrogels. *Journal of the Mechanics and Physics of Solids*, 100:103–130, 2017.

[54] Gilles Marckmann, Erwan Verron, Laurent Gornet, Gregory Chagnon, Pierre Charrier, and P Fort. A theory of network alteration for the mullins effect. *Journal of the Mechanics and Physics of Solids*, 50(9):2011–2028, 2002.

[55] Robert M McMeeking and Chad M Landis. Electrostatic forces and stored energy for deformable dielectric materials. *Journal of Applied Mechanics*, 72(4):581–590, 2005.

[56] Christian Miehe. Discontinuous and continuous damage evolution in ogden-type large-strain elastic materials. *European journal of mechanics. A. Solids*, 14(5):697–720, 1995.

[57] Christian Miehe and Serdar Göktepe. A micro–macro approach to rubber-like materials. part ii: the micro-sphere model of finite rubber viscoelasticity. *Journal of the Mechanics and Physics of Solids*, 53(10):2231–2258, 2005.

[58] Christian Miehe and Joachim Keck. Superimposed finite elastic–viscoelastic–plastoelastic stress response with damage in filled rubbery polymers. experiments, modelling and algorithmic implementation. *Journal of the Mechanics and Physics of Solids*, 48(2):323–365, 2000.

[59] Leonard Mullins. Effect of stretching on the properties of rubber. *Rubber Chemistry and Technology*, 21(2):281–300, 1948.

[60] Leonard Mullins. Permanent set in vulcanized rubber. *Rubber Chemistry and Technology*, 22(4):1036–1044, 1949.

[61] Leonard Mullins and Nr Tobin. Theoretical model for the elastic behavior of filler-reinforced vulcanized rubbers. *Rubber Chemistry and Technology*, 30(2):555–571, 1957.

[62] Leonard Mullins and Nr Tobin. Stress softening in rubber vulcanizates. part i. use of a strain amplification factor to describe the elastic behavior of filler-reinforced vulcanized rubber. *Journal of Applied Polymer Science*, 9(9):2993–3009, 1965.

[63] Ray Ogden and Douglas Roxburgh. A pseudo–elastic model for the mullins effect in filled rubber. *Proceedings of the Royal Society of London A: Mathematical, Physical and Engineering Sciences*, 455(1988):2861–2877, 1999.

[64] Ailish OHalloran, Fergal Omalley, and Peter McHugh. A review on dielectric elastomer actuators, technology, applications, and challenges. *Journal of Applied Physics*, 104(7):9, 2008.

[65] Harold S Park and Thao D Nguyen. Viscoelastic effects on electromechanical instabilities in dielectric elastomers. *Soft Matter*, 9(4):1031–1042, 2013.

[66] Harold S Park, Qiming Wang, Xuanhe Zhao, and Patrick A Klein. Electromechanical instability on dielectric polymer surface: Modeling and experiment. *Computer Methods in Applied Mechanics and Engineering*, 260:40–49, 2013.

[67] Ron Pelrine, Roy Kornbluh, Qibing Pei, and Jose Joseph. High-speed electrically actuated elastomers with strain greater than 100%. *Science*, 287(5454):836–839, 2000.

[68] Ronald E Pelrine, Roy D Kornbluh, and Jose P Joseph. Electrostriction of polymer dielectrics with compliant electrodes as a means of actuation. *Sensors and Actuators A: Physical*, 64(1):77–85, 1998.

[69] Philippe Pibarot and Jean G Dumesnil. Prosthetic heart valves. *Circulation*, 119(7):1034–1048, 2009.

[70] Jean-Sébastien Plante and Steven Dubowsky. Large-scale failure modes of dielectric elastomer actuators. *International journal of solids and structures*, 43(25):7727–7751, 2006.

[71] Jerry H Qi and Mary Boyce. Constitutive model for stretch-induced softening of the stress–stretch behavior of elastomeric materials. *Journal of the Mechanics and Physics of Solids*, 52(10):2187–2205, 2004.

[72] Jerry H Qi and Mary Boyce. Stress–strain behavior of thermoplastic polyurethanes. *Mechanics of Materials*, 37(8):817–839, 2005.

[73] Stefanie Reese and Sanjay Govindjee. A theory of finite viscoelasticity and numerical aspects. *International journal of solids and structures*, 35(26-27):3455–3482, 1998.

[74] Stefanie Reese and Sanjay Govindjee. A theory of finite viscoelasticity and numerical aspects. *International journal of solids and structures*, 35(26-27):3455–3482, 1998.

[75] Pedro M Reis. A perspective on the revival of structural (in) stability with novel opportunities for function: From buckliphobia to buckliphilia. *Journal of Applied Mechanics*, 82(11):111001, 2015.

[76] Zvi Rigbi. Reinforcement of rubber by carbon black. *Properties of Polymers*, pages 21–68, 1980.

[77] Rogers Commission. Presidential commission on the space shuttle challenger accident, report to the president, 1986. https://history.nasa.gov/rogersrep/genindex.htm.

[78] Prashant Saxena, Duc Khoi Vu, and Paul Steinmann. On rate-dependent dissipation effects in electro-elasticity. *International Journal of Non-Linear Mechanics*, 62:1–11, 2014.

[79] Saman Seifi and Harold S Park. Computational modeling of electro-elasto-capillary phenomena in dielectric elastomers. *International Journal of Solids and Structures*, 87:236–244, 2016.

[80] Robert F Shepherd, Filip Ilievski, Wonjae Choi, Stephen A Morin, Adam A Stokes, Aaron D Mazzeo, Xin Chen, Michael Wang, and George M Whitesides. Multigait soft robot. *Proceedings of the National Academy of Sciences*, 108(51):20400–20403, 2011.

[81] Samuel Shian, Roger M Diebold, and David R Clarke. Tunable lenses using transparent dielectric elastomer actuators. *Optics express*, 21(7):8669–8676, 2013.

[82] Phanindhar Shivapooja, Qiming Wang, Beatriz Orihuela, Daniel Rittschof, Gabriel P López, and Xuanhe Zhao. Bioinspired surfaces with dynamic topography for active control of biofouling. *Advanced Materials*, 25(10):1430–1434, 2013.

[83] Juan Carlos Simo. On a fully three-dimensional finite-strain viscoelastic damage model: formulation and computational aspects. *Computer methods in applied mechanics and engineering*, 60(2):153–173, 1987.

[84] John C Snowdon. *Vibration and shock in damped mechanical systems*. J. Wiley, 1968.

[85] Zhigang Suo, Xuanhe Zhao, and William H Greene. A nonlinear field theory of deformable dielectrics. *Journal of the Mechanics and Physics of Solids*, 56(2):467–486, 2008.

[86] Vito L Tagarielli, Richard Hildick-Smith, and John Huber. Electro-mechanical properties and electrostriction response of a rubbery polymer for eap applications. *International Journal of Solids and Structures*, 49(23):3409–3415, 2012.

[87] Behrouz Tavakol and Douglas P Holmes. Voltage-induced buckling of dielectric films using fluid electrodes. *Applied Physics Letters*, 108(11):112901, 2016.

[88] Michael T Tolley, Robert F Shepherd, Bobak Mosadegh, Kevin C Galloway, Michael Wehner, Michael Karpelson, Robert J Wood, and George M Whitesides. A resilient, untethered soft robot. *Soft Robotics*, 1(3):213–223, 2014.

[89] Franziska Vogel, Serdar Göktepe, Paul Steinmann, and Ellen Kuhl. Modeling and simulation of viscous electro-active polymers. *European Journal of Mechanics-A/Solids*, 48:112–128, 2014.

[90] Konstantin Volokh. On electromechanical coupling in elastomers. *Journal of Applied Mechanics*, 79(4):044507, 2012.

[91] Jin Wang, Thao D Nguyen, and Harold S Park. Electrostatically driven creep in viscoelastic dielectric elastomers. *Journal of Applied Mechanics*, 81(5):051006, 2014.

[92] Qiming Wang, Zhigang Suo, and Xuanhe Zhao. Bursting drops in solid dielectrics caused by high voltages. *Nature communications*, 3:1157, 2012.

[93] Qiming Wang, Mukarram Tahir, Jianfeng Zang, and Xuanhe Zhao. Dynamic electrostatic lithography: Multiscale on-demand patterning on large-area curved surfaces. *Advanced Materials*, 24(15):1947–1951, 2012.

[94] Qiming Wang, Mukarram Tahir, Lin Zhang, and Xuanhe Zhao. Electro-creasing instability in deformed polymers: experiment and theory. *Soft Matter*, 7(14):6583–6589, 2011.

[95] Qiming Wang, Lin Zhang, and Xuanhe Zhao. Creasing to cratering instability in polymers under ultrahigh electric fields. *Physical review letters*, 106(11):118301, 2011.

[96] Shuolun Wang and Shawn A Chester. Experimental characterization and continuum modeling of inelasticity in filled rubber-like materials. *International Journal of Solids and Structures*, 2017.

[97] Shuolun Wang, Martina Decker, David L Henann, and Shawn A Chester. Modeling of dielectric viscoelastomers with application to electromechanical instabilities. *Journal of the Mechanics and Physics of Solids*, 95:213–229, 2016.

[98] Michael Wissler and Edoardo Mazza. Electromechanical coupling in dielectric elastomer actuators. *Sensors and Actuators A: Physical*, 138(2):384–393, 2007.

[99] Lei Yan, David A Dillard, Robert L West, Loren D Lower, and Glenn V Gordon. Mullins effect recovery of a nanoparticle-filled polymer. *Journal of Polymer Science Part B: Polymer Physics*, 48(21):2207–2214, 2010.

[100] Qiming Zhang, Vivek Bharti, and Xiao Zhao. Giant electrostriction and relaxor ferroelectric behavior in electron-irradiated poly (vinylidene fluoride-trifluoroethylene) copolymer. *Science*, 280(5372):2101–2104, 1998.

[101] Xuanhe Zhao, Wei Hong, and Zhigang Suo. Electromechanical hysteresis and coexistent states in dielectric elastomers. *Physical review B*, 76(13):134113, 2007.

[102] Xuanhe Zhao, Soo Jin Adrian Koh, and Zhigang Suo. Nonequilibrium thermodynamics of dielectric elastomers. *International journal of applied mechanics*, 3(02):203–217, 2011.

[103] Xuanhe Zhao and Zhigang Suo. Method to analyze electromechanical stability of dielectric elastomers. *Applied Physics Letters*, 91(6):061921, 2007.

[104] Xuanhe Zhao and Qiming Wang. Harnessing large deformation and instabilities of soft dielectrics: Theory, experiment, and application. *Applied Physics Reviews*, 1(2):021304, 2014.